METABOLIC CONTROL OF NAIVE PLURIPOTENCY

by

Benjamin Tonnu Jackson, MPhil

A Dissertation

Presented to the Faculty of the

Louis V. Gerstner, Jr. Graduate School of Biomedical Sciences,

Memorial Sloan Kettering Cancer Center

In Partial Fulfillment of the Requirements for the Degree of

Doctor of Philosophy

New York, NY

August 23, 2023

_____ _____

Lydia Finley, PhD Date

Dissertation Mentor

DEDICATION

This thesis is dedicated to my parents, who gave up so many of their dreams so that one day I could follow mine; to Ann, who always believed in me and made my dreams her own; and to Miku & Sabi, who tried their best to delete this document.

ABSTRACT

Early embryonic development requires rapid cell division while preserving pluripotent cell fate. This requirement necessitates specialized metabolic programs to balance fate regulation with proliferation that are inherently linked to cell identity. Uncovering these metabolic programs therefore is an important step towards understanding mammalian development and to promote the growth of specific cell populations. Embryonic stem cells (ESCs) represent a robust system to uncover the metabolic networks that underlie these key early cell fate transitions. These cells can be captured in culture in a 'naive' ground state of pluripotency that mimics the pre-implantation epiblast, and likewise can assume a more developmentally limited cell state representative of the post-implantation epiblast. By comparing these cell states we can examine the specific metabolic preferences of naive versus more committed ESCs and assess the direct relevance of metabolism to the acquisition and loss of naive pluripotency. Here, we profile both the intracellular metabolic networks and nutrient acquisition programs of ESCs across multiple cell states and demonstrate that two metabolic pathways—tricarboxylic acid cycle (TCA) metabolism and pyruvate uptake—are intrinsically linked to ESC fate and are required for proper maintenance of cellular identity.

The tricarboxylic acid (TCA) cycle is a central biosynthetic hub that generates metabolites and reducing equivalents critical for cellular survival and proliferation. However, diverse substrates can fuel TCA cycle activity across different cell types, including ESCs, suggesting that heterogenous TCA cycle engagement can underlie cell state. To probe this heterogeneity, we performed genetic co-essentiality mapping of TCA-cycle-associated genes and found a gene cluster that might represent a biochemical alternative to the traditional TCA cycle, whereby a portion of mitochondrially-derived citrate flows through the cytosol and is catabolized prior to reimport as malate to complete the cycle. Subsequent genetic and metabolic tracing approaches confirmed the activity of this citrate-malate shuttle (CMS) and demonstrated that its engagement accompanied changes in cell state. Naive ESCs utilize canonical TCA-cycle metabolism and switch to CMS-metabolism with the exit from naive pluripotency. Blocking the

CMS prevented cells from exiting pluripotency, demonstrating the importance of proper TCA-cycle engagement for cell fate transitions.

Many metabolic pathways—including the mitochondrial TCA cycle—rely on the reduction of the cofactor NAD^+ to NADH to sustain cellular oxidation reactions. Cells have therefore evolved multiple routes of NAD^+ regeneration, but the relevance of these pathways in different cell types remains unclear. A hallmark of naive ESCs is the preferential capture and oxidation of glucose-derived pyruvate in the mitochondria which creates a cytosolic NAD^+ deficit. Therefore, we interrogated the mechanism by which naive ESCs regenerate NAD^+ to maintain redox homeostasis and found that enhanced pyruvate uptake sustains NAD^+ regeneration and TCA cycle metabolism in the naive state. Pyruvate uptake is dependent on the monocarboxylate transporter MCT1, but levels of MCT1 are not limiting for pyruvate uptake. Instead, enhanced mitochondrial pyruvate oxidation drives pyruvate uptake from the extracellular environment. Withdrawal of pyruvate or loss of MCT1 selectively impairs naive ESC fitness and can be rescued with alternative electron acceptors or TCA cycle substrates, illustrating how pyruvate demand licenses its uptake to meet the metabolic requirements of naive ESCs.

Altogether, these findings establish selective pyruvate uptake and TCA-cycle rewiring as key features of ESC state and provide insight into the unique metabolic strategies of early development.

BIOGRAPHICAL SKETCH

Benjamin Tonnu Jackson was born on October 11th, 1994, to Raymond F. Jackson and Thuthu Tonnu in Hayward, California. It was there that Ben spent his entire childhood until 2012, when he enrolled at the University of California, Berkeley. During his time as an undergraduate, Ben was exposed to biomedical research through summer programs at the University of California, San Francisco, Genentech, and Harvard Medical School. At the beginning of his sophomore year, he began to work in the laboratory of Dr. David Raulet at UC Berkeley studying the regulation of natural killer cell receptor expression in cancer, culminating in his undergraduate honors thesis. In 2016, he graduated with high distinction from UC Berkeley with honors in Molecular and Cell Biology and with highest honors in English. Ben then pursued a funded fellowship at the University of Cambridge as a member of Trinity College. There, he conducted research in the laboratory of Dr. Gregory Hannon at the Cancer Research United Kingdom Cambridge Institute on the role of non-coding RNAs in normal hematopoiesis. In 2017, he graduated with a Masters in Philosophy in Medical Science. Ben then enrolled in the Tri-Institutional MD-PhD Program at Weill Cornell Medicine/Memorial Sloan Kettering Cancer Center/Rockefeller University. After two years of medical training, Ben joined Dr. Lydia Finley's laboratory in 2019 to begin his thesis research.

ACKNOWLEDGEMENTS

This thesis would not have been possible alone. First, I would like to thank my mentor Dr. Lydia Finley, who provided me with invaluable mentorship and always taught me how to ask the right questions. I hope I can emulate your infectious enthusiasm for science. Thank you also to my committee members, Drs. Effie Apostolou, Kristian Helin, Danwei Huangfu, and Alban Ordureau for their timely advice and words of encouragement that made me look forward to our meetings each year. I would also like Dr. Santosha Vardhana for agreeing to chair my defense committee and Dr. Kivanc Birsoy for serving as my external examiner. Thank you also to the entirety of the Gerstner-Sloan-Kettering Graduate School staff and Tri-Institutional MD-PhD Program office for helping steer me through this journey.

It is hard to imagine a more supportive environment than the Finley laboratory in which to conduct my graduate training. Thank you to all past and present members of the lab for their critical feedback and perceptive questions that shaped this thesis. Specific acknowledgements are detailed in the following chapters. But more than these scientific contributions, thank you all for your sense of humor and continual willingness to listen–it makes the long tissue-culture marathons bearable.

Beyond the lab, I want to acknowledge my friends and family who have kept me sane during the years it took to complete this thesis. Particular thanks are owed to my partner Ann, who tolerated my general tardiness, late nights at the lab, and multiple practice talks on TCA cycle metabolism. Thank you also to my cats Miku and Sabi for their incalculable emotional support. I would also like to thank my classmates, particularly the Tri-I entering class of 2017. It is a long path we have chosen, but I am grateful to walk it in such good company.

TABLE OF CONTENTS

LIST OF FIGURES

LIST OF TABLES

LIST OF ABBREVIATIONS

αKG	alpha-ketoglutarate
αKB	alpha-ketobutyrate
2i	Inhibitors against MEK and GSK3β
ACO2	aconitase 2
ANOVA	analysis of variance
AP	alkaline phosphatase
ATP	adenine triphosphate
cDNA	complimentary deoxyribonucleic acid
CMS	citrate-malate shuttle
d5-2HG	d-2-hydroxyglutaric-2,3,3,4,4-d_5 acid
DAPI	4,6-diamidino-2-phenylindole
DepMap	Cancer Dependency Map
dFBS	dialyzed fetal bovine serum
DM-αKG	dimethyl alpha ketoglutarate
DMEM	Dulbecco's Modified Eagle Medium
DMSO	dimethyl sulfoxide
DNA	deoxyribonucleic acid
DRP1	Dynamin-related protein 1
ECAR	extracellular acidification rate
EpiLC	epiblast-like cell
EpiSC	epiblast-derived stem cell
ESC	embryonic stem cell
ETC	electron transport chain
FACS	fluorescence-activated cell sorting
FBS	fetal bovine serum
FCCP	carbonyl cyanide p-(tri-fluromethoxy)phenyl-hydrazone
GC-MS	gas-chromatography mass spectrometry
GFP	green fluorescent protein
GO	gene ontology
GSK3β	glycogen synthase kinase 3 beta
H3K4	histone 3 lysine 4
KEGG	Kyoto Encyclopedia of Genes and Genomics
***Lb*NOX**	*Lactobacillus brevis* NADH oxidase
LC-MS	liquid-chromatography mass spectrometry
LDH	lactate dehydrogenase
LIF	leukemia inhibitor factor
MCT1	monocarboxylate transporter 1
MCT1-OE	monocarboxylate transporter 1 over-expressing
MCT4	monocarboxylate transporter 4
MDH1	malate dehydrogenase 1
MEF	mouse embryonic fibroblast
MEK	mitogen-activated protein kinase 1

MPC	mitochondrial pyruvate carrier
mTOR	mammalian target of rapamycin
NAD^+	nicotinamide adenine dinucleotide
NADH	nicotinamide adenine dinucleotide + hydrogen
NSCLC	non-small cell lung cancer
OCR	oxygen consumption rate
PBS	phosphate-buffered saline
PDHC	pyruvate dehydrogenase complex
PSC	pluripotent stem cell
qRT-PCR	quantitative real-time polymerase chain reaction
RNA	ribonucleic acid
RNA-seq	ribonucleic acid sequencing
ROS	reactive oxygen species
S/L	serum/leukemia inhibitory factor
SAM	S-adenosyl methionine
sgRNA	single-guide ribonucleic acid
shRNA	short-hairpin ribonucleic acid
SLC25A1	solute carrier family 25 member 1
TCA	tricarboxylic acid
TET	ten-eleven translocation methylcytosine dioxygenases

CHAPTER 1: INTRODUCTION

1.1 Hallmarks of pluripotent stem cell metabolism

Cellular metabolism comprises the metabolic pathways required for the breakdown of nutrients and synthesis of macromolecules required for cellular homeostasis and can be flexibly engaged by different cell types in both normal development and disease. This metabolic plasticity enables the tuning of cellular metabolism to meet cell-type specific functions. Correspondingly, disruption of metabolic function often results in cell-type specific pathologies. Understanding how metabolism is assembled across different cells is critical to uncovering the full breadth of cellular metabolism.

Pluripotent stem cells (PSCs) are a unique cell type with the capacity to form all cells of the developing embryo and represent a powerful model system to study the intersection of metabolism and cell fate[1]. These cells can be captured in vitro in media conditions that promote varying cell fates and allow specific interrogation of cellular metabolism[2]. When cultured with serum and leukemia inhibitor factor (LIF, referred to as S/L), mouse PSCs form a heterogenous metastable population, where only a portion of cells are transcriptionally reminiscent of the pre-implantation epiblast[3]. The addition of inhibitors against MEK and GSK3β (referred to as 2i) is sufficient to drive PSCs into the naive ground state of pluripotency[4],and removal of both 2i and LIF leads to exit from the naive state and the acquisition of differentiation competence[5]. Similarly, PSCs can be induced to form epiblast-like cells (EpiLCs) which are similar to pre-gastrulating epiblasts[6]. Finally, epiblast stem cells (EpiSCs) have been derived from post-implantation mouse epiblasts and represent a primed pluripotent state that is unable to contribute to chimeras upon blastocyst injection[7,8]. Notably, human PSCs isolated in vitro are primed, and ongoing efforts are focused on generating naive human PSCs with increased similarity to the epiblast of the human inner cell mass[9].

These in vitro models of PSC state are highly amenable to studying cellular metabolism. First, the use of pharmacological inhibitors allows cells in different stages of pluripotency to be assayed in identical media conditions. The use of defined media formulations allows the elimination of other culture variables and—by dropout or addition—the interrogation of specific individual metabolites on PSC fate and function. Additionally, the signaling and transcriptional networks of PSCs have been extensively characterized. This knowledge allows the parallel use of genetic perturbations to alter cell fate and examine concomitant metabolic changes. Finally, these models allow the expansion of large numbers of PSCs, making them more amenable to a wide range of multiomic technologies—including metabolomics—than in vivo models of development.

Over the past decades of research, several common hallmarks of stem cell metabolism have emerged[10]. While these themes have broad applications to both pluripotent and adult stem cells, this chapter will focus on the metabolism of pluripotent stem cells. The following topics will be discussed: 1) metabolic pathways supporting PSC proliferation, 2) PSC resistance to metabolic stress, 3) metabolic control of PSC fate, and 4) metabolic requirements of the embryonic niche (**Figure 1.1**).

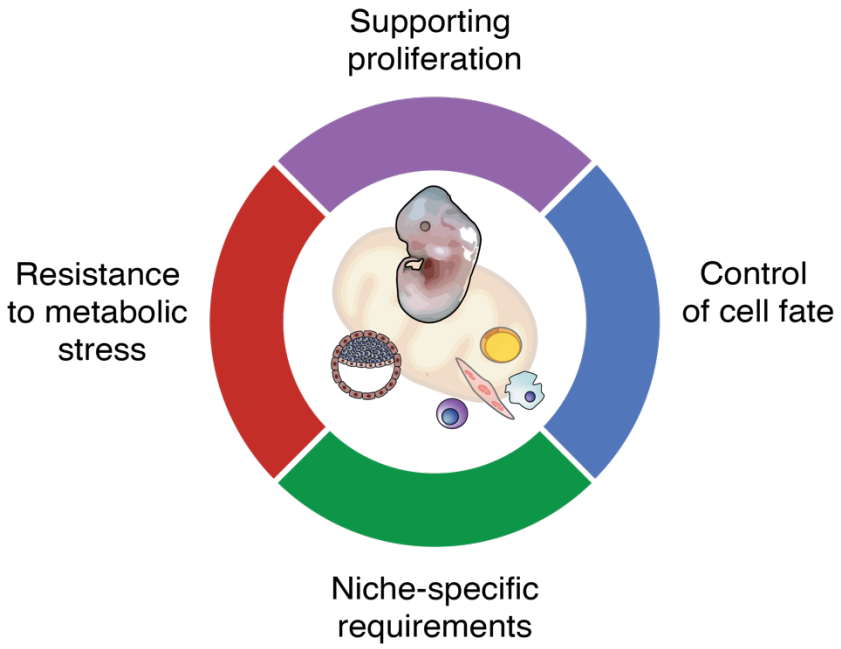

Figure 1.1 Metabolic hallmarks of pluripotent stem cells. PSCs must balance survival and proliferation with maintenance of cell identity. Metabolism supports these goals by enabling rapid proliferation and control of cell fate while guarding against metabolic stressors and meeting the needs of the embryonic niche. Figure was designed with assistance from Julia S. Brunner.

1.2 Metabolic pathways supporting PSC proliferation

Given the sufficient signaling cues to retain the pluripotent state, PSCs can have the capacity to proliferate indefinitely. Multiple studies therefore have asked what metabolic pathways support PSC proliferation. One of the first and broadest approaches taken to profile PSCs has been extracellular flux assays, which measure either the oxygen consumption rate (OCR) or extracellular acidification rate (ECAR) of cells. These values correlate with oxidative phosphorylation and glycolytic activity; however, it is important to note that these values are not absolute quantifications of either pathway activity.

Bioenergetic profiling of naive versus primed mouse PSCs found that naive PSCs have a higher OCR and lower ECAR, corresponding to increased levels of mitochondrial respiration and lower levels of lactate export[11]. In contrast, naive human PSCs have been reported to engage in higher levels of glycolysis as assessed by increased ECAR and glucose incorporation into glycolytic intermediates and switch to oxidative phosphorylation upon differentiation[12,13]. Whether this discrepancy between mouse and human PSCs is due to species-specific biology or in vitro culture differences that fail to fully capture the naive state of human PSCs remains unclear. However, the binning of PSC states into those that burn glucose in the mitochondria or discard it as lactate—the latter commonly referred to as the Warburg effect—is overly simplistic. While the carbons that fuel glycolysis and oxidative phosphorylation derive from the same pool, neither pathway occurs in mutual exclusivity from the other. Oxidative phosphorylation is dependent on the upper steps of glycolysis that generate pyruvate from glucose to fuel the TCA cycle. Even human cancers exhibiting classic features of Warburg effect do respire[14], and PSCs have the flexibility to engage in both metabolic programs upon demand[11,15].

What dictates the choice between oxidative and glycolytic metabolism and what benefits this has for specific developmental pathways remains a key open question for the field. While some studies have implicated specific transcription factors—including Oct4 and Myc—in regulation of glycolytic genes[13,16], the intersection of the pluripotency transcriptional network with metabolism warrants further investigation. Numerous studies have also described changes in mitochondrial morphology with differentiation. While mitochondria in naive PSCs are rounded with sparse irregular cristae, upon differentiation they elongate and contain denser cristae structure[11,15]. Mitochondrial structure in naive PSCs is dependent on DRP1-mediated mitochondrial fission[17]. Despite these studies, a mechanistic of understanding the link between mitochondrial morphology and PSC metabolism has yet to be determined.

Additional studies have focused upon the usage of glucose and glutamine—two major sources of nutrients for mammalian cell—in PSCs. While exogenous glutamine supplementation is required for the culture of most mammalian cells, naive PSCs can proliferate in its complete absence[18-20]. This glutamine independence is accompanied by lower glutamine utilization: cells cultured in the ground state of naive pluripotency incorporate lower levels of glutamine into TCA cycle intermediates[18]. Correspondingly, naive PSCs have increased incorporation of glucose into TCA cycle metabolites relative to metastable counterparts[18,19]. These changes in substrate preference are a generalizable feature of pluripotent stem cells. Alternative forms of inducing self-renewal likewise increase reliance on glucose-derived carbons and decrease dependence on exogenous glutamine[19]. Similarly, within a heterogenous population of PSCs, glutamine withdrawal selects for cells with the highest propensity for self-renewal[19].

While the requirements for glucose and glutamine have been extensively characterized during early differentiation, less is known about the functional consequences of substrate switching for development. In human PSCs, glutamine withdrawal biased cells towards ectoderm and away from mesoderm differentiation, in part through a signaling role[21]. Furthermore, the

molecular cues that govern glucose or glutamine usage in PSCs remain to elucidated. Finally, the contribution of other substrates to TCA cycle anaplerosis has not yet been explored.

1.3 PSC resistance to metabolic stress

Rapid proliferation in PSCs is balanced with tight control of cell death pathways. In the developing mouse embryo, the epiblast cell number increases 100-fold from E5.5 to E7.5[22]. Concomitantly, large numbers of cells are eliminated through apoptosis at E6.5[23]. This induction of cell death with differentiation has been further studied in connection with sensitivity to ionizing radiation. Low dose (0.5 Gy) irradiation induces apoptosis of E6.5 embryos, but not their pre-implantation counterparts that have not yet begun gastrulation[24]. This differential resistance to cell death has also been observed in PSCs in culture and extended to other cellular stresses. For example, loss of micro RNAs, oxidative stress, and endoplasmic reticulum stress all lead to apoptosis induction in EpiSCs but not their naive counterparts[17,25].

These results have led to the hypothesis that embryonic differentiation is accompanied by increased priming for cell death. However, the molecular mechanisms that contribute to this priming remain unclear. As apoptosis is tightly linked to mitochondrial permeabilization and caspase activation[26], several studies have examined the role of mitochondrial dynamics in PSCs. Naive PSCs have higher expression mitochondrial fusion regulator DRP1, and loss of DRP1 is sufficient to lower the apoptotic threshold in these cells. Conversely, overexpression of DRP1 can inhibit apoptosis at baseline and in response to endoplasmic reticulum and oxidative stress in differentiating PSCs[27]. Mitochondrial dynamics therefore might not only support bioenergetics but play an important role in promoting PSC resistance to stress.

Another possibility is that naive PSCs have decreased production of endogenous toxic metabolites or utilize specialized disposal mechanisms to protect the pluripotent state. The most studied of these metabolites are reactive oxygen species (ROS) which are oxygen-containing free radicals that in excess can be cytotoxic[28]. PSCs have low levels of endogenous ROS that increase

with differentiation[29], which has been proposed to protect against genotoxicity. However, ROS can also play important signaling roles, and low levels of ROS are required to maintain PSC self-renewal[30]. While the mechanisms that regulate ROS production in PSCs remain unclear, a new study in oocytes identified elimination of complex I as a mechanism by which oocytes evade mitochondrial ROS production[31]. Whether similar regulation of complex I exists in other cell types remains to be seen. Similarly, future studies will likely explore the relevance of antioxidant pathways such as forkhead box protein O and nuclear factor (erythroid-derive 2)-like 2 to PSC function[29].

An additional method of coping with metabolic stress is the delay of embryonic development. While human development is temporally unyielding, many mammalian species can halt blastocyst development pre-implantation and enter a state referred to as embryonic diapause[32]. Critically, diapause is reversible and paused blastocysts can re-enter normal development upon the induction of specific cues. Diapause has therefore emerged as a strategy by which environmental factors can be coupled to embryonic development to yield the highest chance for successful reproduction.

Numerous studies have characterized the metabolic profile of diapaused embryos, which are thought to exhibit lower usage of metabolic pathways consistent with their more quiescent state[32]. However, specific metabolic changes in diapause are poorly characterized, with opposing roles being reported for glycolysis[33,34] and fatty acid oxidation[33,35]. Diapaused embryos are more reliant on lipid droplets[36] and autophagy[37] for survival, indicating a potential change in substrate preferences during this cell state. Importantly, many of the cues that regulate diapause in embryos are metabolic. Reductions in polyamine levels can delay blastocyst implantation[38] and glucose withdrawal delays the reentry from diapause[39], but how these nutrients fluctuations are communicated to the embryo to dictate cell fate remain unclear.

Given the technical limitations of studying embryonic metabolism in vivo, considerable effort has gone into developing in vitro models of diapause-like states. Two distinct approaches,

inhibition of the transcription factor Myc and inhibition of mechanistic target or rapamycin (mTOR), are sufficient to induce the reversible pausing of cultured PSCs[40,41]. Transcriptionally, these paused PSCs resemble diapaused epiblasts and share common features of diapause including decreased transcription, splicing, and protein synthesis. While modulation of these pathways is sufficient to induce diapause-like states[42], whether their endogenous regulation promotes diapause remains unclear. Altogether, these orthogonal ex vivo pausing strategies have yielded considerable insight into the biology of diapause, and the development of other systems will likely increase our understanding of this unique metabolic state.

1.4 Metabolic control of PSC fate

In addition to meeting the demands of proliferation and resisting cellular stressors, PSCs must retain the capacity for pluripotent differentiation. To this end, metabolites act not only as substrates for cellular anabolism but can directly influence gene expression programs to alter cell fate. Metabolites act as co-substrates for many of the enzymatic reactions that modify histones and nucleic acids. This has led to the hypothesis that fluctuations in levels of metabolites can alter the distribution of chromatin and DNA modifications, which might have particular importance to either maintenance or dismantling of the pluripotent state[43].

Recent studies have suggested that modulating levels of S-adenosylmethionine (SAM)—the methyl donor for histone and DNA methylation—can alter chromatin states in PSCs. Mouse PSCs are uniquely dependent on threonine, which is catabolized into SAM via glycine and acetyl-coenzyme A, and threonine depletion in mouse PSCs reduces H3K4 levels[44]. In contrast to mouse PSCs, human PSCs are dependent on methionine rather than threonine for the catabolic generation of SAM, and depletion of methionine impairs histone methylation[45,46].

Mouse PSCs cultured under conditions that promote the naive ground state of pluripotency exhibit increased intracellular levels of the TCA cycle metabolite alpha-ketoglutarate (αKG) [47,48]. αKG is a co-substrate for the large family of αKG-dependent

dioxygenases, including the Jumonji-domain containing histone demethylases and the ten-eleven-translocation (TET) enzymes that facilitate the oxidation and demethylation of methylated cytosine in DNA. In both PSCs and a variety of other stem and cancer cell types, αKG has been proposed to act via these αKG-dependent demethylases to remove repressive DNA or histone methylation[49]. Additional evidence for this hypothesis in PSCs comes from the role of ascorbate, a cofactor for αKG-dependent dioxygenases such as the TET enzymes. Vitamin C addition in ESCs promotes TET activity and leads to an increase in DNA demethylation[50]. Therefore, by either increasing levels of the co-substrate (αKG) or enzyme activity (ascorbate), PSCs might regulate chromatin methylation states in response to a rewiring of intracellular metabolism. However, the precise αKG-dependent enzymes that mediate this process have not yet been identified, and the relevance of these metabolites to in vivo PSC development remains unclear. In human PSCs, αKG supplementation leads to differentiation accompanied by DNA and histone demethylation[51]. Whether the same enzymes are relevant in both cell types—and why demethylation promotes two disparate phenotypes—requires further investigation.

Histone acetylation has similarly been shown to play a role in PSCs. Histone acetyltransferases utilize the metabolite acetyl-CoA to acetylate lysine residues and create marks generally associated with actively transcribed loci[52]. Acetyl-CoA is generated by numerous pathways in the cell, including mitochondrial oxidation of glucose, amino acids, and fatty acids. In the cytosol, ATP-citrate lyase (ACL) processes glucose-derived citrate into acetyl-CoA and oxaloacetate, thereby linking the production of acetyl-CoA for acetylation and lipid synthesis with mitochondrial metabolism[53]. Additional histone acylations have also been linked to availability of specific acyl-donors[54]. Pluripotent human PSCs utilize glycolysis to produce acetyl-CoA, and decreased glycolysis upon differentiation correlates with reduced histone acetylation[55].

Considerable numbers of studies continue to reinforce the link between metabolic pathways and transcriptional regulation of cell fate through chromatin and DNA modification. However, important questions remain unanswered[56]. Do physiologic shifts in metabolite concentrations occur that are sufficient to limit or promote enzyme function that alters the chromatin landscape? How are these shifts coordinated across organelles when metabolite levels can differ dramatically between cellular compartments? What dictates the specificity of metabolite-chromatin regulation, both at the level of the enzymes that carry out these reactions and at the loci that are perturbed? Finally, can metabolism affect posttranslational modifications on other macromolecules such as RNA or proteins that similarly regulate cell fate? Studies both in PSCs and other cell types aimed at addressing these questions will be paramount to further understanding this aspect of PSC metabolism.

1.5 Metabolic requirements of the embryonic niche

While some attention has been given to the role of niche metabolism in maintaining adult stem cells[57], less is known about the extracellular environment in which zygotes develop to form blastocysts and begin the process of multilineage differentiation. Part of this challenge is technical, as limited tools exist to probe embryonic metabolism in vivo. While recent advances in metabolic tracing in vivo[58,59] and in vitro models of embryogenesis hold great promise, most studies are limited by reliance on aspects of the embryonic niche that can be recapitulated in 2D culture.

An example of one such niche requirement is nutrient uptake, which poses a metabolic challenge for both pluripotent and adult stem cells that reside in specific physiologic locations. While soluble amino acids are an important nutrient source for mammalian cell proliferation, the maternal reproductive tract is relatively nutrient-poor[60]. Several studies have investigated methods of nutrient acquisition by PSCs. Amino acids are largely acquired by a diverse set of plasma membrane transporters that facilitate entry of these nutrients to fuel protein translation

and other cellular functions[61]. However, naive PSCs have been shown to proliferate and gain biomass in the absence of essential amino acids [62]. A notable exception is threonine, which mouse PSCs are uniquely reliant on due to cell-type specific expression of threonine dehydratase[44,63].As for glutamine, the withdrawal of essential amino acids such as leucine likewise selects for the most naive cells within a metastable population. Mechanistically, amino acid independence is enabled by high levels of macropinocytosis, whereby extracellular protein is taken up and digested in the lysosome to release amino acids required for growth[62].

The ability of naive PSCs to grow without essential amino acids mimics early studies demonstrating that embryos can develop to the blastocyst stage in the complete absence of soluble amino acids[64,65]. Indeed, all cells of the pre-implantation blastocyst engage in macropinocytosis[62], suggesting a conservation of nutrient acquisition programs between ESC culture models and embryonic development. That these metabolic strategies are hard-wired into the cells of the pre-implantation epiblast irrespective of other cell types or 3D architecture verifies their utility to uncover metabolic programs with direct relevance to embryogenesis.

The maternal reproductive tract notably differs in the concentration of key carbohydrate substrates. While glucose is present at approximately 5 mM in plasma, it can be much as tenfold lower in oviductal fluid[60]. Conversely, levels of lactate are considerably higher while pyruvate levels are maintained. Experiments dating back to the 1960s demonstrated that zygotes can develop to the blastocyst stage with pyruvate as their sole energy source[66], suggesting that this unique carbohydrate composition may reflect the nutrient needs of the developing embryo. However, how these substrate preferences are established, how they support PSC proliferation, and whether they are preserved in vitro remain unexplored.

1.6 Dissertation research aims

These studies and others have examined the way that metabolism changes in the trajectory from naive pluripotency to early differentiation, However, less is known about how this

metabolic rewiring functionally contributes to changes in cell state. The goal of this dissertation is to interrogate the molecular mechanisms by which metabolism sustains naive pluripotency or facilitates the acquisition of differentiation competence. We find that both intracellular metabolic networks and nutrient acquisition programs vary in concert with cell state. In the first chapter of this thesis, we demonstrate that configuration of the tricarboxylic acid (TCA) cycle changes as ESCs exit naive pluripotency, and that this TCA cycle rewiring is required for changes in cell state. Shifts in intracellular metabolic networks are likewise accompanied by variation in nutrient acquisition and substrate preferences. In the second chapter of this thesis, we examine the differential metabolite uptake of naive and more differentiated ESCs and demonstrate that pyruvate is selectively taken up by and supports cells in the ground state of naive pluripotency. Together, this work highlights the dynamic and critical role metabolism plays in the early stages of development.

CHAPTER 2: A NON-CANONICAL TRICARBOXYYLIC CYCLE UNDERLIES CELLULAR IDENTITY

2.1 Abstract

The tricarboxylic acid (TCA) cycle is a central hub of cellular metabolism, oxidizing nutrients to generate reducing equivalents for energy production and critical metabolites for biosynthetic reactions. Despite the importance of the products of the TCA cycle for cell viability and proliferation, mammalian cells display diversity in TCA-cycle activity[67,68]. How this diversity is achieved, and whether it is critical for establishing cell fate, remains poorly understood. Here we identify a non-canonical TCA cycle that is required for changes in cell state. Genetic co-essentiality mapping revealed a cluster of genes that is sufficient to compose a biochemical alternative to the canonical TCA cycle, wherein mitochondrially derived citrate exported to the cytoplasm is metabolized by ATP citrate lyase, ultimately regenerating mitochondrial oxaloacetate to complete this non-canonical TCA cycle. Manipulating the expression of ATP citrate lyase or the canonical TCA-cycle enzyme aconitase 2 in mouse myoblasts and embryonic stem cells revealed that changes in the configuration of the TCA cycle accompany cell fate transitions. During exit from pluripotency, embryonic stem cells switch from canonical to non-canonical TCA-cycle metabolism. Accordingly, blocking the non-canonical TCA cycle prevents cells from exiting pluripotency. These results establish a context-dependent alternative to the traditional TCA cycle and reveal that appropriate TCA-cycle engagement is required for changes in cell state.

Chapter 2 is adapted from Arnold, P.K.*, Jackson, B.T.*, et al. A non-canonical tricarboxylic acid cycle underlies cellular identity. *Nature* **603**, 477-481 (2022).

2.2 Results

2.2.1 Two modes of TCA cycle metabolism

Mammalian cells use diverse strategies to meet their metabolic demands. In particular, heterogeneous TCA-cycle substrate preferences and enzyme activities suggest that cells selectively engage components of the TCA cycle[68,69]. We therefore investigated whether enzymes that are involved in the TCA cycle form discrete functional modules by analyzing gene essentiality scores generated from genome-wide CRISPR screens by the DepMap project[70], as genes participating in the same pathway exhibit similar patterns of essentiality[71]. Genes involved in core metabolic pathways were clustered on the basis of the pairwise correlation of gene essentiality scores. Of the clusters that emerged, one contained genes that are involved in glycolysis and one contained genes that are required for one-carbon metabolism, consistent with the notion that these genes comprise distinct functional modules (**Figure 2.1**)

By contrast, TCA-cycle-associated genes separated into two distinct clusters, even after unbiased analysis of the top co-dependencies of all TCA-cycle genes (**Figure 2.1 and Figure 2.2a**). Two-dimensional mapping of correlation distance demonstrated that these clusters were linked by shared co-dependency for *Dld*, a subunit that is required for both the pyruvate and oxoglutarate dehydrogenase complexes (**Figure 2.3a**). Mapping genes in each cluster onto the canonical TCA-cycle pathway underscored a clear division of the TCA cycle into two segments upstream and downstream of citrate (**Figure 2.3b**), raising the question of how cells sustain citrate production if oxidative production of oxaloacetate through the TCA cycle is not tightly linked to citrate synthesis. Suggestively, enzymes involved in cytosolic citrate metabolism, including the mitochondrial citrate/malate antiporter (encoded by *Slc25a1*) and ATP citrate lyase (ACL, encoded by *Acly*), were correlated with enzymes involved in citrate production (**Figure 2.3a, b**). The catabolism of mitochondrially derived citrate by ACL provides the cytoplasmic acetyl-CoA required for protein acetylation and lipid biosynthesis[72,73]. The co-dependency of

ACL with TCA-cycle enzymes suggests that ACL may also support cellular metabolic demands by forming a non-canonical TCA cycle that is capable of continuous oxaloacetate regeneration for citrate production.

TCA-cycle metabolism can be monitored by tracing [U-13C]glucose, which generates citrate containing two heavy-labelled carbons (M+2-labelled citrate) following oxidative decarboxylation of glucose-derived pyruvate (**Figure 2.3c**). Further metabolism by mitochondrial aconitase (ACO2) generates M+2-labelled TCA-cycle intermediates, whereas metabolism by ACL liberates M+2-labelled acetyl-CoA, thereby generating unlabeled oxaloacetate and downstream derivatives. Thus, a decrease in M+2 labeling of TCA-cycle intermediates downstream of citrate can partly reflect the degree to which cells engage a non-canonical TCA cycle. Many cultured cells show a disconnect between M+2 labeling of citrate and downstream metabolites, as shown in 82 non-small cell lung cancer (NSCLC) lines[74] (**Figure 2.3d**). To determine whether the loss of glucose label downstream of citrate is due in part to flux through ACL, we treated selected NSCLC lines with an ACL inhibitor. ACL inhibition increased the proportion of malate containing two labelled carbons while having only a small effect on the fraction of citrate M+2 (**Figure 2.2b**). Although glutamine anaplerosis will also contribute to a disconnect between fractional labeling of citrate and malate[75], ACL inhibition did not uniformly affect glutamine anaplerosis, indicating that the effect of ACL on label loss downstream of citrate is not merely due to glutamine-derived label dilution (**Figure 2.2c**). Within an individual cell line, the degree to which malate is derived from the canonical TCA cycle can be represented as the ratio of malate M+2 relative to citrate M+2 (mal+2/cit+2). ACL inhibition increased the mal+2/cit+2 ratio in all of the cell lines, indicating that citrate metabolism by ACL contributes to the loss of glucose labeling downstream of citrate (**Figure 2.3e**).

As an orthogonal labeling strategy, human osteosarcoma cells expressing guinea pig asparaginase[76] were incubated with [U-13C]asparagine to produce M+4-labelled citrate, which will lose labelled carbons when metabolized by the traditional TCA cycle (**Figure 2.2d**). Here,

ACL inhibition significantly increased the ratio of cit+2/cit+4, reflecting citrate regeneration through the oxidative TCA cycle (**Figure 2.2e, f**). These results are consistent with the model that citrate metabolism by ACL represents an important alternative to the canonical TCA cycle.

2.2.2 ESCs engage a non-canonical TCA cycle

To determine whether an ACL-mediated TCA cycle exists in non-transformed cells, we traced the fate of [U-13C]glucose in mouse embryonic stem (ES) cells, which self-renew indefinitely when cultured with serum and leukemia inhibitory factor (LIF). Similar to cancer cells, ES cells exhibit reduced enrichment of malate M+2 relative to citrate M+2 that is mitigated by ACL inhibition (**Figure 2.4a, b**). To compare the effects of ACL inhibition with disruption of the canonical TCA cycle, we generated clonal ES cell lines with genetic disruption of *Acly* or *Aco2* (**Figure 2.4c, d**). *Acly* disruption had no consistent effect on M+2 enrichment in citrate but consistently increased M+2 enrichment in downstream TCA-cycle metabolites, thereby elevating the mal+2/cit+2 ratio (**Figure 2.5a, b**). By contrast, *Aco2* disruption reduced the M+2 enrichment of downstream TCA-cycle metabolites and decreased the mal+2/cit+2 ratio (**Figure 2.4e**). Surprisingly, despite the role of ACO2 as a canonical TCA-cycle enzyme, *Aco2* disruption minimally affected steady-state levels of TCA-cycle metabolites (**Figure 2.4f**). By contrast, *Acly* mutation substantially altered levels of TCA-cycle metabolites that are associated with cytosolic citrate processing (citrate, malate, aspartate and fumarate), but not canonical TCA-cycle metabolism (succinate, α-ketoglutarate) (**Figure 2.5c**).

To test the hypothesis that a portion of the TCA cycle flows through ACL, we directly tested whether ACL mediates citrate recycling. Cytosolic processing of citrate to malate requires hydride donation from NADH, which can be traced by culturing cells with [4-2H]glucose to label up to half of cytosolic NADH pools[77] (**Figure 2.5d**). *Acly* mutation did not affect NADH labeling from [4-2H]glucose: both control and edited cells exhibit similar fractional enrichment of NADH and lactate, which becomes labelled when lactate dehydrogenase reduces cytosolic pyruvate

(**Figure 2.4g, h**). However, *Acly*-edited cells did display significantly lower M+1 enrichment of malate, indicating that wild-type cells generate a portion of malate by reducing ACL-derived cytosolic oxaloacetate (**Figure 2.5e**). Importantly, *Acly* mutation more than halved the fraction of labelled citrate, suggesting that cytosolic malate is indeed recycled back into the mitochondria for citrate regeneration, and that this process is impaired in the absence of ACL (**Figure 2.5f and Figure 2.4i–k**). Consistent with impaired transfer of cytosolic reducing equivalents to the mitochondria, *Acly* mutation increased the cytosolic NADH/NAD^+ ratio, measured as the ratio of lactate to pyruvate[78], and decreased mitochondrial oxygen consumption (**Figure 2.4l, m**).

To further test whether SLC25A1, ACL and MDH1 form a non-canonical TCA cycle, we generated clonal ES cell lines deficient for SLC25A1 and MDH1 (**Figure 2.6a, b**). Deuterated glucose tracing revealed that, like ACL, both SLC25A1 and MDH1 were required for citrate regeneration from cytosolic oxaloacetate (**Figure 2.6c, d**). Accordingly, *Slc25a1*- and *Mdh1*-edited cells exhibited [U-13C]glucose labeling patterns that were consistent with reduced non-canonical TCA-cycle activity, including increased enrichment of M+2 isotopologues in TCA-cycle metabolites downstream of citrate and an elevated mal+2/ cit+2 ratio (**Figure 2.5g, h and Figure 2.6e, f**). Furthermore, *Slc25a1* and *Mdh1* mutation, like *Acly* mutation, reduced malate and fumarate pools (**Figure 2.6g**). SLC25A1 loss also reduced aspartate pools, but MDH1 loss did not, consistent with its role in the malate–aspartate shuttle that consumes cytosolic aspartate[79]. These data demonstrate that SLC25A1, ACL and MDH1 coordinate a cross-compartment cycle of citrate metabolism.

2.2.3 TCA-cycle choice is cell-state dependent

As Krebs originally elucidated the canonical TCA cycle in pigeon breast[80] muscle, we assessed TCA-cycle choice in C2C12 myoblasts and differentiated myotubes. Compared with myoblasts, myotubes exhibited increased incorporation of glucose-derived carbons into TCA-cycle intermediates and a mal+2/cit+2 ratio of greater than fivefold higher than proliferating

myoblasts (**Figure 2.7a and Figure 2.8a, b**). Consistent with switching from the non-canonical to canonical TCA cycle, [4-2H]glucose tracing revealed a diminished production of malate, fumarate and citrate from cytosolic oxaloacetate in myotubes compared with in myoblasts (**Figure 2.8c**). To further assess TCA-cycle engagement, we engineered cells to express doxycycline-inducible short hairpin RNAs (shRNAs) targeting *Acly* or *Aco2* (**Figure 2.8d**). ACL inhibition significantly increased the mal+2/cit+2 ratio in myoblasts, but not myotubes (**Figure 2.8e–h**). By contrast, although ACO2 inhibition decreased the mal+2/cit+2 ratio in myoblasts, this effect was greater in myotubes, consistent with canonical TCA-cycle engagement after differentiation (**Figure 2.8e–h**). As in ES cells, ACL inhibition significantly increased citrate pools and decreased the levels of fumarate, malate and aspartate, and this effect was stronger in myoblasts compared with in myotubes (**Figure 2.7b**). By contrast, ACO2 inhibition had little effect on the levels of TCA-cycle metabolites in myoblasts and, surprisingly, tended to increase metabolite levels in myotubes, indicating that ACO2 loss causes greater metabolic disruption in myotubes compared with in myoblasts (**Figure 2.7b**). Collectively, these results indicate that the degree to which cells use the canonical TCA cycle is at least partially determined by cell state.

To identify potential drivers of TCA-cycle choice, we compared gene expression with TCA-cycle activity in NSCLC lines. TCA-cycle genes were highly enriched among genes that were positively correlated with the mal+2/cit+2 ratio (**Figure 2.9a**). Similarly, myogenic differentiation significantly induced most TCA-cycle genes, many of which are targets of the myogenic transcription factor MYOD[81] (**Fig. 2.7c**). As all of the subunits of the pyruvate dehydrogenase complex (PDHC), which initiates carbon entry into the TCA cycle, were upregulated after myogenic differentiation, we tested whether modulating pyruvate entry into the TCA cycle affected the TCA-cycle choice. Both myoblasts and ES cells that were treated with dichloroacetate to potentiate PDHC activity[82] increased the incorporation of glucose-derived carbons not only into citrate but also into downstream metabolites, thereby increasing the mal+2/cit+2 ratio consistent with enhanced canonical TCA-cycle activity (**Figure 2.7d, e and**

Figure 2.9b, c). Reciprocally, pharmacological inhibition of the mitochondrial pyruvate carrier reduced incorporation of glucose-derived carbons into TCA-cycle metabolites and repressed the mal+2/cit+2 ratio (**Figure 2.7d , e and Figure 2.9b, c**). Thus, TCA-cycle choice is determined in part by the amount of pyruvate captured for oxidation by PDHC.

2.2.4 TCA-cycle switch after pluripotency exit

We next examined whether changes in TCA-cycle configuration are required for changes in cell state. ES cells cultured with LIF and inhibitors against GSK3β and MEK (2i) represent the naive ground state of pluripotency reminiscent of the pre-implantation epiblast; withdrawal of these factors (−2i/LIF) enables cells to exit the naive pluripotent state and gain differentiation competence[5] (**Figure 2.10a–c**). Loss of naive pluripotency triggers major changes in TCA-cycle dynamics: cells induced to exit naive pluripotency decrease incorporation of glucose-derived carbon while increasing incorporation of glutamine-derived carbon (**Figure 2.10d, e**), consistent with our previous report demonstrating enhanced glutamine dependence in more committed ES cells[83]. The high mal+2/cit+2 ratio of naive ES cells is progressively reduced during exit from naive pluripotency alongside a concomitant increase in citrate production from cytosolic intermediates (**Figure 2.11a, b and Figure 2.10f**). This metabolic shift was not due to changes in the culture medium: ES cells cultured serum-free in 2i/LIF also repressed glucose utilization and had a decreased mal+2/cit+2 ratio after 2i/LIF withdrawal, despite continuous culture in the same medium formulation (**Figure 2.10g–i**). Furthermore, cells deficient for *Tcf3*/*Tcf7l1*, a repressor of the naive pluripotency gene network[84], exhibited dampened metabolic reprogramming corresponding to a delayed exit from naive pluripotency **(Figure 2.10j–m**).

Together, these results indicate that ES cells switch from canonical to non-canonical TCA-cycle activity as they dismantle naive pluripotency. Accordingly, metabolic rewiring during exit from pluripotency required ACL—*Acly* edited clones maintained higher incorporation of glucose-derived carbons and lower incorporation of glutamine-derived carbons compared with

their control counterparts grown in −2i/LIF conditions (**Figure 2.12a, b**). ACL loss did not affect the mal+2/cit+2 ratio or steady-state levels of TCA-cycle metabolites in naive ES cells, but doubled the mal+2/cit+2 ratio and triggered up to sevenfold changes in TCA-cycle metabolite levels in cells grown under −2i/LIF conditions (**Figure 2.12c–f**). As a consequence, ACL was required for inducing large changes in TCA-cycle metabolites and maintaining viability specifically after exit from naive pluripotency (**Figure 2.11c and Figure 2.12g**). Impaired viability was not due simply to deficient cytosolic acetyl-CoA after ACL loss: exogenous acetate restored histone acetylation and supported de novo lipid synthesis—processes that require cytosolic acetyl-CoA[73]—but minimally rescued viability (**Figure 2.12h–k**). Thus, after exit from naive pluripotency, cells rely on the non-canonical TCA cycle to maintain TCA-cycle intermediates and cell viability.

2.2.5 Exit from pluripotency requires ACL

We therefore tested whether exit from naive pluripotency requires ACL. Using ES cells containing a reporter of naive pluripotency (*Rex1::GFPd2*) [85], we found that the expected reporter downregulation after 2i/LIF withdrawal[5] was almost completely prevented by ACL inhibition (**Figure 2.11d and Figure 2.12l**). Similarly, following 2i/LIF withdrawal, *Acly*-edited clones demonstrated increased expression of the naive pluripotency genes *Nanog*, *Esrrb* and *Rex1*, impaired induction of the differentiation marker *Sox1* and an enhanced ability to form alkaline-phosphatase-positive colonies when reseeded into medium containing 2i/LIF (**Figure 2.11e and Figure 2.12m, n**). None of these phenotypes were reversed by exogenous acetate, which tended to increase colony formation (**Figure 2.12o–q**), consistent with reports that acetate promotes ES cell self-renewal[55]. These results demonstrate that ACL loss selectively impairs the metabolism and viability of cells during 2i/LIF withdrawal, independent of cytosolic acetyl-CoA.

Like ACL, neither SLC25A1 nor MDH1 was required for the viability of naive pluripotent ES cells (**Figure 2.13a**). Moreover, like ACL, the loss of SLC25A1 specifically

impaired the viability of cells under −2i/ LIF conditions, but the loss of MDH1 did not (**Figure 2.13b**). Notably, although ACL, SLC25A1 and MDH1 were all required to sustain the TCA-cycle metabolites fumarate and malate during exit from naive pluripotency, only SLC25A1 and ACL were required to maintain aspartate pools (**Figure 2.13c**). Aspartate, which contributes to protein and nucleotide biosynthesis, is a critical output of the TCA cycle in proliferating cells[79,86]. Consistent with this, when induced to exit naive pluripotency, both *Acly*- and *Slc25a1*-edited cells, but not *Mdh1*-edited cells, had impaired protein synthesis and reduced proliferation (**Figure 2.13d–g**). Accordingly, while *Acly*- and *Slc25a1*-edited cells preserved naive pluripotency gene signatures, this effect was blunted in *Mdh1*-edited cells (**Figure 2.13h, i**). Together, these results demonstrate that SLC25A1, ACL and MDH1 establish metabolic identity as cells exit the naive pluripotent state, and cells that are unable to activate ACL-dependent non-canonical TCA-cycle metabolism exhibit compromised viability.

To further test the model that appropriate TCA-cycle engagement enables establishment of cell identity, we tested whether efficient induction of the naive, ground state of pluripotency requires canonical TCA-cycle metabolism. *Aco2* disruption did not affect proliferation in serum/LIF-cultured ES cells, which exhibit non-canonical TCA-cycle activity (**Figure 2.14a**). Supplementing the cells with 2i to initiate conversion to naive pluripotency slowed the proliferation of *Aco2*-edited clones and delayed the induction of naive pluripotency markers (**Figure 2.14b, c**). Collectively, these results underscore the role of TCA-cycle configuration in facilitating cell state transitions.

2.3 Discussion

Here we identified a non-canonical TCA cycle that is active in both normal and transformed cells. The possibility of a similar citrate–malate shuttle has been proposed but has never been demonstrated[72,87,88]. By combining isotope tracing with genetic manipulation of ACL, SLC25A1 and MDH1, we provide direct evidence that the proposed citrate–malate shuttle indeed

represents a bona fide cycle with differential activity across mammalian cell states. Potential advantages of non-canonical TCA-cycle engagement include retaining, rather than combusting, reduced carbon and regenerating cytosolic NAD^+ required to sustain glycolysis. By circumventing several steps of the mitochondrial TCA cycle, the non-canonical TCA cycle maintains oxaloacetate regeneration while minimizing mitochondrial NADH production, which may restrain cell proliferation[89]. Notably, in contrast to their in vitro counterparts, cancer cells growing in vivo exhibit little loss of glucose label between citrate and malate[90,91], suggesting that differential TCA-cycle engagement contributes to the discrepancy between in vitro and in vivo metabolic phenotypes. Consistent with this, pancreatic cancer cells are more reliant on *Acly* in vitro and more dependent upon *Aco2* in vivo[92]. Collectively, these studies underscore the diversity of metabolic strategies that support cellular bioenergetics and reveal that TCA-cycle behavior is dynamic and entwined with cell state.

2.4 Experimental Methods

Metabolic co-essentiality analysis and network modelling

To obtain metabolic gene essentiality scores, we analyzed CERES gene dependency values from the DepMap Portal Project Achilles[93,94] 20Q2 release in which 18,119 genes were perturbed by genome-wide loss of function CRISPR screens in 769 human cancer cell lines. We used two gene lists to perform our analysis. To focus on an unbiased set of metabolic genes corresponding to well-defined metabolic pathways, we created a gene set of 122 genes derived from four GO terms[95,96]: tricarboxylic acid cycle (GO:0006099), canonical glycolysis (GO:0061621), 1-carbon metabolic process (GO:0006730) and fatty-acyl-CoA metabolic process (GO:0035337). To focus more specifically on the TCA cycle, we used a list of 27 core TCA-cycle genes and then identified the top 10 correlates of these genes using Pearson correlation coefficients from DepMap gene essentiality scores above a minimum threshold ($r > 0.25$). Next,

we identified the top 5 correlates of this expanded list again above a minimum threshold ($r > 0.25$), resulting in a list of 115 TCA-cycle associated genes.

To examine genetic co-dependency in these gene lists, Pearson correlation coefficients were calculated between metabolic gene essentiality scores across the 769 human cancer cell lines surveyed to generate a correlation matrix heat map of codependent gene modules. To create the heat map, the correlations were hierarchically clustered with the UPGMA algorithm using the scipy.cluster.hierarchy.linkage function from the SciPy Python package[97], with the method argument set to 'average'. The heat map was graphed using the Seaborn Python package (https://seaborn.pydata.org/citing.html). To visualize codependent gene modules as a network diagram, we used the Python package NetworkX (http://networkx.org). Genes with no correlation partners or with low correlation scores ($r < 0.25$) were filtered out, and spring model layouts were generated using the method 'neato' from the Python package PyGraphviz (http://pygraphviz.github.io). Graph edges were weighted according to the strength of pairwise gene correlations and the final network diagram was created using the NetworkX draw function. Gene clusters with less than three members were removed.

Gene expression correlation

NSCLC cell line isotope tracing data were obtained from previously published data[74]. Gene expression data were obtained from the DepMap Cancer Cell Line Encyclopedia[98]. For the 68 cell lines present in both datasets, expression of each gene was correlated with the fractional enrichment of malate M+2 relative to citrate M+2 (mal+2/cit+2) derived from [U-13C]glucose. Genes were ranked on the basis of correlation with mal+2/cit+2, and gene set enrichment analysis[99] of the gene set KEGG citric acid (TCA) cycle-associated genes (KEGG_CITRATE_CYCLE_TCA_ CYCLE; M3985) was performed using GSEAPreranked version 4 with the default parameters. Data were exported and graphed in GraphPad Prism v.9.

Cell culture

Mouse ES cells were previously generated from C57BL/6 × 129S4/SvJae F1 male embryos[47]. *Rex1::GFPd2* ES cells[85] were a gift from A. Smith. All other cell lines were obtained from ATCC. ES cells were maintained on gelatin-coated plates in the following media: serum/LIF, serum/LIF+2i or 2i/LIF. Serum/LIF medium contained knockout DMEM (10829018; Thermo Fisher Scientific) supplemented with 10% fetal bovine serum (FBS; Gemini), 0.1 mM 2-mercaptoethanol, 2 mM l-glutamine and 1,000 U ml−1 LIF (Gemini). To generate serum/LIF+2i maintenance medium, serum/LIF medium was supplemented with 3 μM CHIR99021 (Stemgent) and 1 μM PD0325901 (Stemgent) (2i). 2i/LIF medium contained a 1:1 mix of DMEM/F-12 (11320033; Gibco) and Neurobasal medium (21103049; Gibco) including N-2 supplement (17502048; Gibco), B-27 supplement (17504044; Gibco), 2-mercaptoethanol, 2 mM l-glutamine, LIF and 2i. To generate ES cells in the naive ground state of pluripotency, serum/LIF-cultured ES cells were adapted for three passages to serum/LIF+2i medium or 2i/LIF medium. Adapted cells were used for a maximum of nine passages.

For exit from naive pluripotency, serum/LIF+2i-cultured ES cells were seeded at least 24 h before washing with PBS and changing into medium containing a 1:1 mix of glutamine-free DMEM (11960051; Gibco) and Neurobasal medium including N-2 supplement, B-27 supplement, 2-mercaptoethanol and 2 mM l-glutamine at the indicated time before collection (24 or 40 h). 2i/LIF-cultured ES cells were seeded at least 24 h before being washed with PBS and changed into serum-free maintenance medium without 2i or LIF at the indicated time before collection (12, 24 or 40 h). Unless otherwise noted, cells were adapted to serum/LIF+2i culture before exit from naive pluripotency.

C2C12 cells were maintained at subconfluence as myoblasts unless otherwise noted. All myoblast experiments were performed in high-glucose DMEM supplemented with 10% FBS and 4 mM l-glutamine. For differentiation into myotubes, C2C12 cells were grown to 100% confluence for 3 days and then washed with PBS and changed into differentiation medium composed of high-glucose DMEM supplemented with 2% horse serum (26050070; Gibco), 4 mM

l-glutamine and 100X insulin–transferrin–selenium–ethanolamine (ITS-X; 51500056; Gibco) for the indicated length of time (3, 5 or 7 days). Differentiation medium was refreshed every day. For NSCLC cell line studies, the H2170, A549 and Calu-1 cell lines were thawed and passaged in RPMI-1640 supplemented with 10% FBS before being transitioned to high-glucose DMEM supplemented with 10% FBS and 4 mM L-glutamine for several passages before the experiments. 143B cells were maintained in high-glucose DMEM supplemented with sodium pyruvate, 10% FBS and penicillin–streptomycin. Cell lines treated with inhibitors were cultured as described above but the medium was supplemented with DMSO, 50 μM BMS-303141 (SML0784; Sigma-Aldrich), 5 mM dichloroacetate (3447795; Sigma-Aldrich) or 10 μM UK-5099 (4186; Tocris) for 24 h before collection or for the duration of the exit from pluripotency. Cell lines were not externally authenticated. All cells routinely tested negative for mycoplasma.

Generation of clonal ES cell lines

Single guide RNA (sgRNA) sequences targeting *Acly*, *Aco2*, *Slc25a1*, *Mdh1* or a control, non-genic region on mouse chromosome 8[100] were cloned into the pSpCas9(BB)-2A-GFP plasmid (PX458, Addgene plasmid number 48138), as previously described38. A list of sgRNA sequences is provided in **Table 1**. ES cells (4×10^5 per condition) were electroporated using the 4D-Nucleofector (Amaxa, Lonza) system with 5 μg PX458 plasmid encoding Cas9, EGFP and sgRNA sequences. After electroporation, cells were plated onto a layer of mitotically inactivated feeder mouse embryonic fibroblasts (MEFs). After 48 h, cells were dis- sociated with Accutase (Invitrogen) and sorted using the BD FACSAria III sorter (BD Biosciences) to enrich for GFP-positive cells. Approximately 10,000 fluorescence-activated cell sorting (FACS)-sorted GFP-positive cells per experimental condition were immediately reseeded onto 10 cm plates (on feeder MEFs) to enable clonal growth. After 7 days, individual clones were picked and expanded (initially on feeder MEFs, then on gelatin-coated tissue culture plates) and loss of target gene expression was validated by immunoblotting (see below).

Generation of Tcf7l1-edited ES cell lines

Cas9 cDNA from a lentiCas9-Blast plasmid (Addgene plasmid number 52962) was cloned into Piggybac (pCAGGS-IRES-Neo, a gift from H. Niwa). ES cells were transfected with Piggybac plus transposase (pBase) at a ratio of 3:1 using Fugene HD (E2691; Promega). After selection with G418 (300 μg/mL, 10131-035; Gibco), cells were plated on feeder MEFs at a single-cell density to generate clonal Cas9+ ES cell lines.

sgRNA sequences targeting *Tcf7l1*[101] or a non-genic region on mouse chromosome 8 were cloned into the pUSEPB plasmid[102] (gift from S. Lowe) as previously described[103]. A list of sgRNA sequences is provided in **Table 1**. Lentivirus was generated by the co-transfection of sgRNA vectors with the packaging plasmids psPAX2 and pMD2.G (Addgene) into HEK293T cells. Virus-containing supernatant was cleared of cellular debris by 0.45 μm filtration and was concentrated using Lenti-X (631231; Takara). Cas9-ES cells were exposed to concentrated viral supernatant with 6 μg/ml polybrene for 24 h before being washed, grown for 24 h in fresh medium and selected for using antibiotics. Cells were expanded and loss of target gene expression was validated by immunoblotting (see below).

Table 1: Chapter 2 sgRNA primer sequences

Chr.8 Control	CACCGACATTTCTTTCCCCACTGG
	AAACCCAGTGGGGAAAGAAA TGTC
Acly sg1	CACCGGGGCGTACTTGAACCGGTTC
	AAACGAACCGGTTCAAGTACGCCCC
Acly sg2	CACCGGAACCGGTTCAAGTACGCCC
	AAACGGGCGTACTTGAACCGGTTCC
Aco2 sg	CACCGGCCAACCAGGAGATCGAGCG
	AAACCGCTCGA TCTCCTGGTTGGCC
Slc25a1 sg1	CACCGCTTCACGTATTCGGTCGGGA
	AAACTCCCGACCGAATACGTGAAGC

Slc25a1 sg2	CACCGGAGAGGACTATTGTGCGGTC
	AAACGACCGCACAATAGTCCTCTCC
Mdh1 sg1	CACCGTTGGACATCACCCCCATGAT
	AAACA TCA TGGGGGTGA TGTCCAAC
Mdh1 sg2	CACCGTCAGCCAGCTGTCGTCTTTC
	AAACGAAAGACGACAGCTGGCTGAC
Tcf7l1 sg	CACCGCCGGGCAAGCTCATAGTATT
	AAACAATACTATGAGCTTGCCCGGC

Lentiviral production and infection

Renilla luciferase-, *Acly*- and *Aco2*-targeting shRNAs were introduced into C2C12 cells to enable doxycycline-inducible expression using lentiviral LT3GEPIR[104] (the shRNA sequences are provided in **Table 2**). The lentivirus was generated by the co-transfection of shRNA-expressing viral vectors with the packaging plasmids psPAX2 and pMD2.G (Addgene) into HEK293T cells. Virus-containing supernatants were cleared of cellular debris by 0.45 μm filtration and mixed with 8 μg/ml polybrene. C2C12 cells were exposed to viral supernatants for two 24 h periods before being passaged and grown for 24 h in fresh medium and then subjected to antibiotic selection with 1 μg/ml puromycin. Cells were maintained under antibiotic selection until all cells on an uninfected control well were eliminated.

Table 2: Chapter 2 shRNA sequences

Xho1/ECORI for mir30-based shRNA cloning, 5'-3'

shRenilla	TGCTGTTGACAGTGAGCGCAGGAATTATAATGCTTATCTATAGT GAAGCCACAGATGTATAGATAAGCATTATAATTCCTATGCCTA CTGCCTCGGA
shAcly-1	TGCTGTTGACAGTGAGCGCCTGTATTAATCTGATTTTTAATAGT GAAGCCACAGATGTATTAAAAATCAGATTAATACAGTTGCCTA CTGCCTCGGA

shAcly-2	TGCTGTTGACAGTGAGCGCTGTAACATACAAGTGTTTAAATAG TGAAGCCACAGATGTATTTAAACACTTGTATGTTACAATGCCTA CTGCCTCGGA
shAco2-1	TGCTGTTGACAGTGAGCGCTCACCAGATCATTCTAGAAAATAG TGAAGCCACAGATGTATTTTCTAGAATGATCTGGTGAATGCCT ACTGCCTCGGA
shAco2-2	TGCTGTTGACAGTGAGCGACAGTATGACCAAGTGATTGAATAG TGAAGCCACAGATGTATTCAATCACTTGGTCATACTGGTGCCTA CTGCCTCGGA

Viability assays

Serum/LIF+2i-adapted ES cells were seeded at a density of 24,000 cells per well of a 24-well plate in triplicate or quadruplicate. Then, 24 h later, the cells were washed with PBS and changed into either fresh serum/LIF+2i medium or medium containing a 1:1 mix of glutamine-free DMEM and Neurobasal medium including N-2 supplement, B-27 supplement, 2-mercaptoethanol and 2 mM L-glutamine for 40 h. The cells were evaluated for propidium iodide on the LSRFortessa flow cytometer using FACSDiva software v.8.0 (BD Biosciences). Analysis of propidium iodide exclusion was performed using FCS Express v.7.05 or FlowJo v.10.8.0.

Growth curves

ES cells were seeded at a density of 40,000 cells per well of a 12-well plate. The next day, three wells of each line were counted to determine the starting cell number. The remaining cells were washed with PBS and either changed to medium containing serum/LIF+2i or induced to exit from naive pluripotency as indicated above. Cells were counted 40 h later using a Beckman Coulter Multisizer 4e with a cell volume gate of 400–10,000 fl. Cell counts were normalized to starting cell number. All curves were performed at least two independent times.

Naive pluripotency conversion growth curve

ES cells were seeded in standard culture medium (serum/LIF) in six-well plates; then, 48 h later, cells were counted to establish a baseline measurement of proliferation for each line under serum/LIF culturing conditions. After this count, ES cells were seeded into serum/LIF+2i

maintenance medium and passaged and counted every 48 h for 6 days (three passages). Cumulative population doublings were assessed by summing population doublings measured at each passage. Cells were counted using a Beckman Coulter Multisizer 4e with a cell volume gate of 400–10,000 fl.

OP-puro assay

All cells were washed with PBS and changed into fresh medium 60 min before collection. For cycloheximide control samples, 10 μg/mL cycloheximide was added to wells at this time. At 30 min before collection, 20 μM O-propargyl-puromycin (OP-puro, HY-15680; Med- ChemExpress) was added to cells. Cells were collected and stained with fixable viability dye (65-0863-14; Thermo Fisher Scientific), followed by fixation with 4% PFA in PBS and permeabilization with 0.25% Triton-X-100. Fixed and permeabilized cells were stained using the Click-iT Plus Alexa Fluor 647 Picolyl Azide Toolkit (C10643; Thermo Fisher Scientific) and AZDye 647 Picoyl Azide (1300-1; Click Chemistry Tools) according to the manufacturer's instructions, and analysed on the LSRFortessa flow cytometer using FACSDiva v.8.0 (BD Biosciences). Analysis of OP-puro incorporation was performed with FCS Express v.7.05 or FlowJo v.10.8.0.

Rex1::GFPd2 analysis

On the day of analysis, cells were trypsinized and resuspended in FACS buffer (PBS, 2% FBS and 1 mM EDTA) containing 4,6-diamidino-2-phenylindole (DAPI, 1 μg/mL). Cells were evaluated for DAPI and GFP on the LSRFortessa flow cytometer using FACSDiva v.8.0 (BD Biosciences). Viable cells were those that excluded DAPI. *Rex1::GFPd2* expression was measured by GFP mean fluorescence intensity (MFI) and quantified using FCS Express v.7.0.5 or FlowJo v.10.8.0.

Metabolic analyses

For isotope tracing experiments, ES cells were seeded in standard culture medium in six-well plates. Then, 24 h or 40 h later, cells were washed with PBS and changed into experimental

medium containing a 1:1 mix of glutamine-free DMEM and glutamine-free Neurobasal medium including 10% dialyzed FBS, 2-mercaptoethanol, LIF and 2 mM L-glutamine with or without 2i. The next day, cells were washed with PBS and changed into medium containing a 1:1 combination of glucose- and glutamine-free DMEM and glucose- and glutamine-free Neurobasal-A medium including 10% dialyzed FBS, 2-mercaptoethanol, LIF and 2i as specified and supplemented with [12C]glucose (Sigma-Aldrich) and [12C]glutamine (Gibco) or the labelled versions of each metabolite: [U-13C]glucose, [4-2H]glucose or [U-13C]glutamine (Cambridge Iso- tope Laboratories) to a final concentration of 20 mM (glucose) and 2 mM (glutamine) for 4 h before collection. To analyze metabolites in serum/LIF+2i-cultured ES cells undergoing exit from pluripotency, ES cells were seeded in maintenance medium in six-well plates overnight. Either 24 or 40 h before collection, cells were washed with PBS and changed into medium containing a 1:1 mix of glutamine-free DMEM and Neurobasal medium including N-2 supplement, B-27 supplement, 2-mercaptoethanol and 2 mM L-glutamine. To analyze metabolites in 2i/LIF-cultured ES cells undergoing exit from pluripotency, ES cells were seeded in serum-free maintenance medium in six-well plates overnight. Either 24 or 40 h before collection, cells were washed with PBS and changed into serum-free maintenance medium without 2i or LIF. In all cases, 4 h before collecting, cells were washed with PBS and changed into medium containing a 1:1 combination of glucose- and glutamine-free DMEM and glucose- and glutamine-free Neurobasal-A medium including N-2 and B-27 supplements and 2-mercaptoethanol, and supplemented with [12C]glucose and [12C]glutamine or the labelled versions of each metabolite to a final concentration of 20 mM (glucose) and 2 mM (glutamine).

For mass spectrometry (MS) analyses of C2C12 myoblasts and NSCLC cell lines, cells were seeded in six-well plates and the medium was changed 24 h or 48 h later. The next day, the cells were washed with PBS and changed into medium containing glucose- and glutamine-free DMEM including 10% dialyzed FBS and supplemented with [12C]glucose and [12C]glutamine or the labelled versions of each metabolite: [U-13C]glucose, [4-2H]glucose or [U-13C]glutamine

(Cambridge Isotope Laboratories) to a final concentration of 20 mM (glucose) and 4 mM (glutamine) for 4 h before collection. Forty-eight hours before collection, myoblasts were supplemented with 1 μg/mL doxycycline to induce shRNA expression. For analysis of myotubes, cells seeded in six-well plates were grown to 100% confluence for 3 days, washed with PBS and changed to differentiation medium that was refreshed every day for 5 or 7 days. On the final day of differentiation, the cells were washed with PBS and changed to experimental medium described above. For analysis of C2C12 myotube genetic hairpin lines, the cells were processed as described above, but the medium was supplemented with 1 μg/mL doxycycline for the final four days of differentiation to induce shRNA expression. Cell lines treated with inhibitors were processed as described above but medium was supplemented with DMSO, 50 μM BMS-303141, 5 mM dichloroacetate or 10 μM UK-5099 for 24 h before collection. At collection, metabolites were extracted with 1 ml ice-cold 80% methanol containing 2 μM deuterated 2-hydroxyglutarate (d-2-hydroxyglutaric- 2,3,3,4,4-d5 acid (d5-2HG)). After overnight incubation at −80 °C, lysates were collected and centrifuged at 21,000g for 20 min to remove protein. All extracts were further processed using liquid chromatography coupled with MS (LC–MS) (for analysis of the lactate/pyruvate ratio and deuterium labeling of NADH, lactate and succinate) or gas chromatography coupled with MS (GC–MS) (for all other analyses) as described below.

143B cells were plated in six-well plates; 24 h later, the medium was changed to DMEM supplemented with 10% dialyzed FBS, 1 mM asparagine and DMSO or 50 μM BMS-303141. After 20 h, the medium was changed to DMEM supplemented with 10% dialyzed FBS, 1 mM [U-13C] asparagine and DMSO or 50 μM BMS-303141. The cells were extracted with 300 μl 80% methanol containing valine-D8 as an internal control. 143B extracts were further processed using LC–MS as described below.

Fatty acid analyses

To analyze fatty acids in serum/LIF+2i-cultured ES cells undergoing exit from pluripotency, ES cells were seeded in maintenance medium in six-well plates overnight. The next

day, the cells were washed with PBS and changed into medium containing a 1:1 mix of glutamine-free DMEM and Neurobasal medium including N-2 supplement, B-27 supplement, 2-mercaptoethanol and 2 mM L-glutamine. Then, 24 h before collection, the cells were washed with PBS and changed into medium containing a 1:1 combination of glucose- and glutamine-free DMEM and glucose- and glutamine-free Neurobasal-A medium including N-2 supplement, B-27 supplement, 2-mercaptoethanol, 2mM l-glutamine and 20 mM glucose supplemented with 5 mM [1,2-13C]sodium acetate (Cambridge Isotope Laboratories). At collection, lysates were collected in PBS and centrifuged at 6,800g for 5 min to pellet the cells. To isolate fatty acids, the cell pellets were resuspended in 400 µl high-performance liquid chromatography (HPLC)-grade methanol followed by 800 µl HPLC-grade chloroform, and the samples were vortexed for 10 min at 4 °C. HPLC grade water (300 µl) was then added to induce phase separation. Next, 800 µl of the bottom chloroform layer was moved to a new tube and lyophilized. Dried samples were saponified by resuspending in 1 ml of 80% methanol with 0.3 M KOH and heating at 80 °C for 1 h in a glass vial. HPLC grade hexanes (1 ml) were then added to the vial and briefly vortexed. Next, 800 µl of the top hexane layer was moved to a new tube and lyophilized. The extracts were then further processed by LC–MS as described below.

GC–MS analysis

The extracts were dried in an evaporator (Genevac EZ-2 Elite) and resuspended by incubating with shaking at 30 °C for 2 h in 50 µl of 40 mg/mL methoxyamine hydrochloride in pyridine. The metabolites were further derivatized by adding 80 µl of N-methyl-N-(trimethylsilyl) trifluoroacetamide with or without 1% TCMS (Thermo Fisher Scientific) and 70 µl ethyl acetate (Sigma-Aldrich) and then incubated at 37 °C for 30 min. The samples were analyzed using the Agilent 7890A gas chromatograph coupled to an Agilent 5977C mass selective detector. The gas chromatograph was operated in splitless injection mode with constant helium gas flow at 1 ml/min; 1 µl of derivatized metabolites was injected onto an HP-5ms column and the gas chromatograph oven temperature increased from 60 °C to 290 °C over 25 min. Peaks representing

compounds of interest were extracted and integrated using MassHunter v.B.08 (Agilent Technologies) and then normalized to both the internal standard (d5-2HG) peak area and protein content of triplicate samples as determined using the bicinchoninic acid assay (Thermo Fisher Scientific). Steady-state metabolite pool levels were derived by quantifying the following ions: d5-2HG, 354 *m/z*; αKG, 304 *m/z*; aspartate, 334 *m/z*; citrate, 465 *m/z*; fumarate, 245 *m/z*; malate, 335 *m/z*; and succinate, 247 *m/z*. All of the peaks were manually inspected and verified relative to known spectra for each metabolite. Enrichment of [13C] or [2H] was assessed by quantifying the abundance of the following ions: aspartate, 334–346 *m/z*; citrate, 465–482 *m/z*; fumarate, 245–254 *m/z*; and malate, 335–347 *m/z*. Correction for natural isotope abundance was performed using IsoCor (v.1.0 or v.2.0) [105].

LC–MS analysis

Lyophilized samples were resuspended in 80% methanol in water and transferred to LC–MS vials for measurement by LC–MS. Metabolite quantitation was performed using the Q Exactive HF-X Hybrid Quadrupole-Orbitrap Mass Spectrometer equipped with an Ion Max API source and H-ESI II probe, coupled to a Vanquish Flex Binary UHPLC system (Thermo Fisher Scientific). Mass calibrations were completed at a minimum of every 5 days in both the positive and negative polarity modes using LTQ Velos ESI Calibration Solution (Pierce).

Polar samples. Polar samples were chromatographically separated by injecting a sample volume of either 1 µl in the MS1 mode or 5 µl in the SIM mode into a SeQuant ZIC-pHILIC Polymeric column (2.1 × 150 mm, 5 mM, EMD Millipore). The flow rate was set to 150 ml/min, autosampler temperature set to 10 °C and column temperature set to 30 °C. Mobile phase A consisted of 20 mM ammonium carbonate and 0.1 % (v/v) ammonium hydroxide, and mobile phase B consisted of 100 % acetonitrile. The sample was gradient eluted (percentage of B) from the column as follows: 0–20 min: linear gradient from 85% to 20% B; 20–24 min: hold at 20% B; 24–24.5 min: linear gradient from 20% to 85% B; 24.5 min to the end: hold at 85% B until equilibrated with ten column volumes. Mobile phase was directed into the ion source with the

following parameters: sheath gas = 45, auxiliary gas = 15, sweep gas = 2, spray voltage = 2.9 kV in the negative mode or 3.5 kV in the positive mode, capillary temperature = 300 °C, RF level = 40%, auxiliary gas heater temperature = 325 °C. Mass detection was conducted with a resolution of 240,000 in full scan mode or 120,000 in SIM mode, with an AGC target of 3,000,000 and maximum injection time of 250 ms for the full scan mode, or 100,000 ms and 100 ms for the SIM mode. Metabolites were detected over mass range of 70–1,050 m/z in full scan positive mode, or SIM in positive mode using a quadrupole isolation window of 0.7 m/z.

Non-polar samples. Non-polar samples were chromatographically separated by injecting 2 µl into an Accucore Vanquish C18+ column (2.1 × 100 mm, 1.5 µm particle size, 27101-102130, Thermo Fisher Scien- tific). The autosampler temperature was set at 10 °C and the flow rate was 500 µl/min with the column temperature set at 50 °C. The largely isocratic gradient consisted of a mixture of water and 5 mM ammonium acetate as A and acetonitrile as B. At 0–6.5 min, the solvent composition was held at 60% B, followed by a change to 98% B between 6.5–6.6 min. The composition was held at 98% B between 6.6–9.0 min, and then returned back to starting conditions at 60% B between 9.0–9.1 min. It was then held for an additional 4.4 min to re-equilibrate the column for the next run. Non-polar analytes were detected in the negative polarity mode at a resolution of 240,000 in the full scan setting, using a mass range of 240-650 m/z. The AGC target value was 3,000,000 with a maximum injection time of 200 ms. The chromatography peak width setting was 10 s (FWHM), and data were collected in profile mode. The parameters for the H-ESI source were as follows: sheath gas flow rate of 53 units, aux gas flow rate of 14 units, sweep gas flow rate of 3 units, with the spray voltage set at 3.00 kV. The funnel RF level was set at 40%, and the capillary and auxiliary gas heater temperatures were held at 300 °C and 400 °C, respectively. Quantification of all metabolites was performed using Tracefinder v.4.1 (Thermo Fisher Scientific) referencing an in-house metabolite standards library using ≤5 ppm mass error. Data from stable isotope labeling experiments include correction for natural isotope abundance using IsoCor v.2.2.

Oxygen consumption

The oxygen consumption rate (OCR) was measured using a Seahorse XFe96 Extracellular Flux Analyzer (Agilent Technologies). ES cells were plated on gelatin-coated tissue-culture-treated XF96 96-well plates (Agilent Technologies) at 2×10^4 cells per well in standard maintenance medium. The next day, the cells were washed twice with assay medium (Seahorse XF DMEM medium supplemented with 10 mM glucose) and changed to assay medium containing 2 mM L-glutamine for 2 h before the assay. Baseline measurements of OCR were obtained three times. After the assay, the protein content was determined and averaged for each condition and the OCR measurements were normalized to these values. The third baseline OCR reading was averaged across all 12 replicates; averaged values from three independent experiments are shown.

Western blotting

Protein lysates were extracted in 1× RIPA buffer (Cell Signaling Technology), separated by SDS–polyacrylamide gel electrophoresis and transferred to nitrocellulose membranes (Bio-Rad). For histone blots, cell pellets were flash-frozen in ethanol and resuspended in Laemmli buffer for sonication. The samples were mixed with 5% BME and 0.01% bromo- phenol blue before identical separation was performed as described for protein lysates. The membranes were blocked in 3% milk in Tris-buffered saline with 0.1% Tween-20 (TBST) or 5% BSA in TBST and incubated at 4 °C with primary antibodies overnight. After TBST washes the next day, the membranes were incubated with horseradish-peroxidase-conjugated secondary antibodies (mouse, NA931; rabbit, NA934; Cytiva) for at least 2 h, incubated with enhanced chemiluminescence (Thermo Fisher Scientific) and imaged using the SRX-101A X-ray Film Processor (Konica Minolta). The antibodies used (at 1:1,000 unless otherwise indicated) were: anti-ACL (4332; Cell Signaling Technologies), anti-ACO2 (MA1- 029; Thermo Fisher Scientific), anti-SLC25A1 (15235-1-AP; ProteinTech), anti-MDH1 (sc-166879; Santa Cruz Biotechnology), anti-AceCS1/ACSS2 (3658; Cell Signaling Technologies), anti-TCF7L1 (sc-

166411; Santa Cruz Biotechnology), anti-myogenin/MYOG (14-5643-82; Thermo Fisher Scientific), anti-MYH3 (22287-1-AP; ProteinTech), anti-vinculin (1:10,000; V9131; Sigma), anti-tubulin (T9026; Sigma-Aldrich), anti-H3K9ac (9469; Cell Signaling Technology), anti-H3K14ac (07-353; Millipore Sigma), anti-H3K27ac (39133; Active Motif), anti-H4K16ac, (1:500; 39167; Active Motif), anti-H3 (Ab1791; Abcam) and anti-H4 (1:500; 07-108; Millipore Sigma). C2C12 myoblast genetic hairpin lines were maintained in medium supplemented with 1 μg/mL doxycycline for 48 h before protein lysate extraction to induce shRNA expression.

Colony-formation assay

ES cells adapted to 2i/LIF or serum/LIF+2i were subjected to exit from pluripotency in triplicate for 12, 24 or 40 h. On the day of collection, the cells were counted and reseeded at a density of 2,000 cells per well in technical triplicate in maintenance medium containing 2i and LIF. The medium was refreshed every 3 days. Then, 6 days after initial seeding, the cells were fixed with citrate/acetone/3% formaldehyde for 30 s and stained with the Leukocyte Alkaline Phosphatase Kit (Sigma-Aldrich) according to the manufacturer's instructions. The colonies were quantified using ImageJ's particle analysis function and technical triplicates were averaged for each condition.

Quantification of gene expression

RNA was isolated from six- or twelve-well plates using TRIzol (Invitrogen) according to the manufacturer's instructions and 200 ng RNA was used for complementary DNA (cDNA) synthesis using the iScript cDNA Synthesis Kit (Bio-Rad). Quantitative PCR with reverse transcription (RT–qPCR) analysis was performed in technical triplicate using QuantStudio 5 or 6 Flex (Applied Biosystems) with the Power SYBR Green Master Mix (Thermo Fisher Scientific). All data were generated using cDNA from three independent wells for each condition. Actin was used as an endogenous control for all of the experiments. A list of the RT–qPCR primer sequences is provided in **Table 3**.

Table 3: Chapter 2 qRT-PCR primer sequences

Actin, forward	GCTCTTTTCCAGCCTTCCTT
Actin, reverse	CTTCTGCATCCTGTCAGCAA
Nanog, forward	AAGATGCGGACTGTGTTCTC
Nanog, reverse	CGCTTGCACTTCATCCTTTG
Esrrb, forward	AACAGCCCCTACCTGAACCT
Esrrb, reverse	TGCCAA TTCACAGAGAGTGG
Klf2, forward	TAAAGGCGCATCTGCGTACA
Klf2, reverse	CGCACAAGTGGCACTGAAAG
Rex1, forward	TCCATGGCATAGTTCCAACAG
Rex1, reverse	TAACTGATTTTCTGCCGTATGC
Klf4, forward	CGGGAAGGGAGAAGACACT
Klf4, reverse	GAGTTCCTCACGCCAACG
Sox1, forward	CCTCGGATCTCTGGTCAAGT
Sox1, reverse	GCAGGTACATGCTGATCATCTC
Otx2, forward	GACCCGGTACCCAGACATC
Otx2, reverse	GCTCTTCGATTCTTAAACCATACC
Fgf5, forward	AAACTCCA TGCAAGTGCCAAA T
Fgf5, reverse	TCTCGGCCTGTCTTTTCAGTTC
Oct4, forward	TGGATCCTCGAACCTGGCTA
Oct4, reverse	CCCTCCGCAGAACTCGTATG

RNA-seq analysis of myoblasts and myotubes

RNA was isolated as described above and quantified using a Qubit 3.0 fluorometer. RNA-seq libraries were generated using the TruSeq Stranded mRNA Library Prep Kit (20020594, Illumina) according to the manufacturer's instructions. The samples were pooled and sequenced at the Memorial Sloan Kettering Cancer Center Integrated Genomics Operation. RNA-seq libraries were filtered and trimmed using fastp[106] and mapped with STAR aligner[107] against the mm10 mouse genome assembly using default parameters. featureCounts[108] was used to

calculate gene counts for input into DESeq2(ref[109]) for quality control analysis, size normalization and variance dispersion corrections.

Statistics and reproducibility

Prism 9 (GraphPad) software was used for statistical analyses, except for DepMap data. Error bars, P values and statistical tests are reported in the figures and figure legends. Statistical analyses on DepMap data were performed using Python v3.8. No statistical methods were used to predetermine sample sizes. All data were collected and analyzed objectively using instruments without bias. Therefore, blinding is not relevant to this study. Experimental samples were randomly distributed into groups. Experiments were performed in biological triplicate or as indicated in the figure legends and were repeated at least two (often many more) times.

2.5 Acknowledgements

Rex1::GFPd2 cells were a gift from A. Smith. Work in this chapter was performed with assistance from multiple members of the Finley and Sullivan laboratories as indicated in figure legends.

2.6 Figures

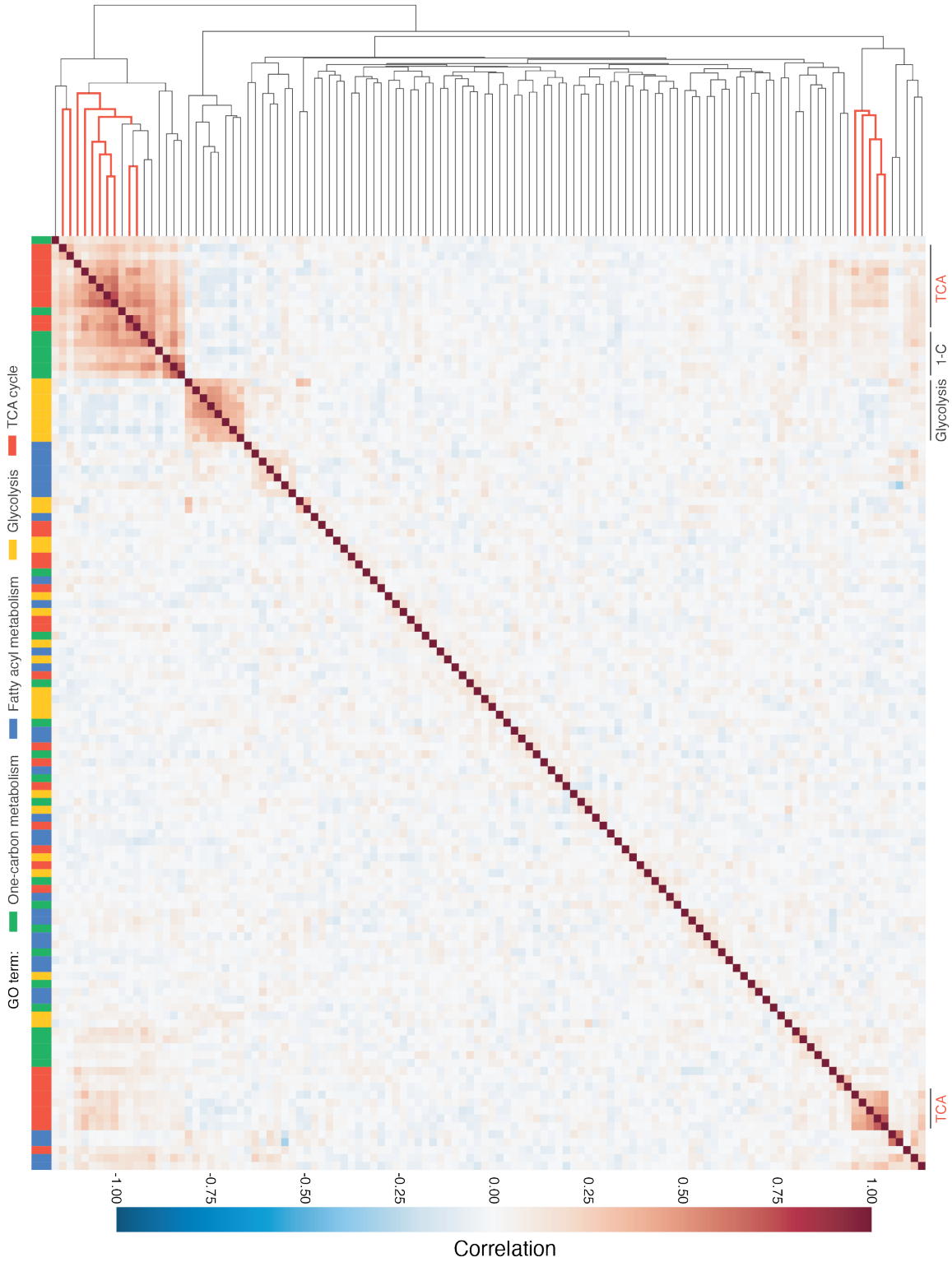

Figure 2.1 Metabolic gene essentiality correlations across cancer cell lines. Heatmap depicting hierarchical clustering of pairwise gene essentiality score correlations of core metabolic pathway genes derived from four GO terms: tricarboxylic acid (TCA) cycle, canonical glycolysis, one-carbon metabolic process and fatty-acyl-CoA metabolic process. Genes are color coded to the left of the heatmap according to the GO term. TCA cycle genes are highlighted (red) in the

dendrogram. This analysis was performed by the author of this thesis (from Arnold*, Jackson* et al., *Nature* 2022).

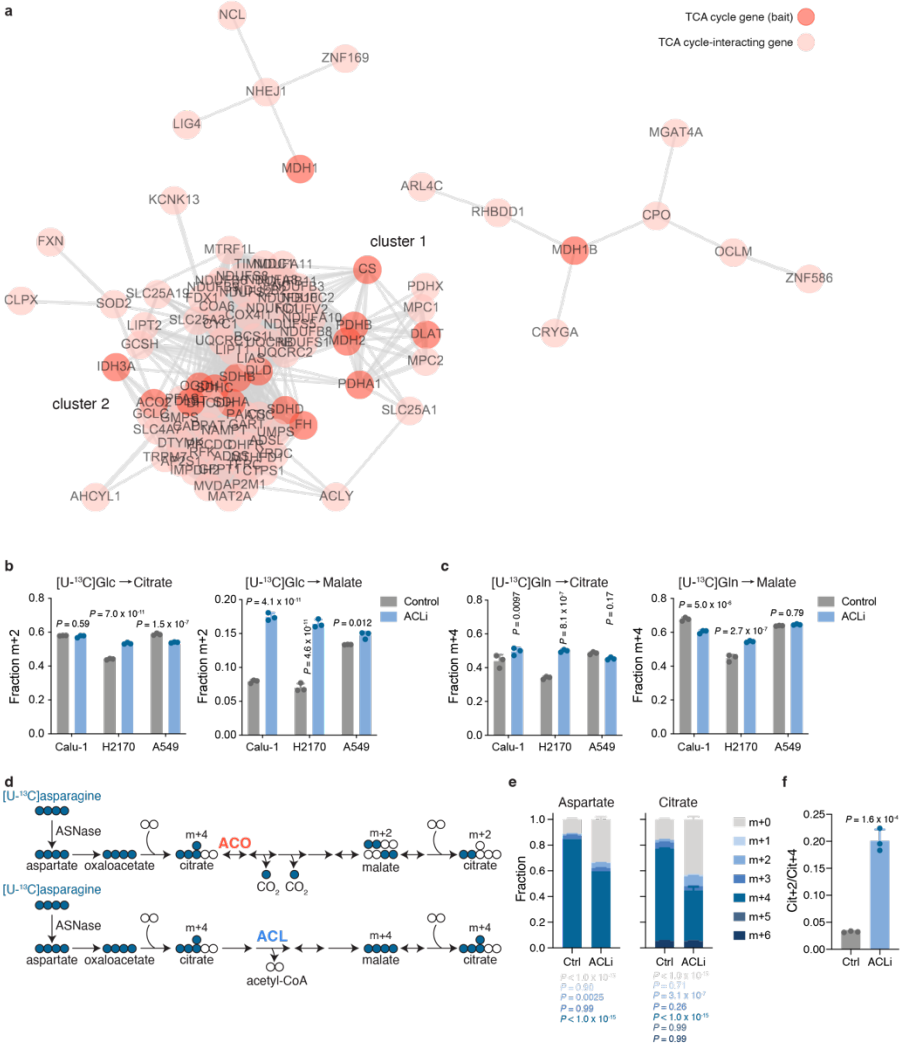

Figure 2.2 Effect of ACL inhibition on ^{13}C labeling of TCA cycle metabolites. a, Two-dimensional network diagram representing gene essentiality score correlations between TCA cycle genes and their top co-dependencies. The strength of the correlation between genes is represented by both the length and thickness of the connecting edge. **b**, **c**, Fractional enrichment of citrate (left) and malate (right) in three NSCLC cell lines cultured in medium containing [U-^{13}C]glucose (**b**) or [U-^{13}C]glutamine (**c**) and treated with vehicle or 50 μM BMS-303141(ACLi) for 24 h. **d**, Schematic depicting [U-^{13}C] asparagine labeling of aspartate and citrate in cells expressing guinea pig asparaginase (ASNase). Asparagine-derived aspartate will generate M+4-labelled citrate. Top, M+4-labelled citrate metabolized via the canonical TCA cycle will lose two labelled carbons as CO_2, ultimately regenerating citrate that retains two labelled carbons (M+2). Bottom, M+4-labelled citrate metabolized by ACL will yield M+4 labelled oxaloacetate that will ultimately regenerate M+4-labelled citrate. **e**, **f**, Fractional labeling of aspartate (left) and citrate (right) (**e**) or citrate M+2 relative to citrate M+4 (cit+2/cit+4) (**f**) in ASNase-expressing 143B human osteosarcoma cells cultured in medium containing [U-^{13}C]asparagine and treated with vehicle or 50 μM ACLi for 24 h. Data are mean ± SD, n = 3 independent replicates. Significance was assessed in comparison to vehicle treatment by two-way ANOVA with Sidak's multiple

comparisons post-test (**b-c**, **e**) or using unpaired two-tailed Student's *t*-test (**f**). Co-essentiality analysis (panel **a**) was performed by the author of this thesis. Panels **b-c** were generated by Paige K. Arnold and panels **d-f** were generated by Sydney P. Alibeckoff and Madeleine L. Hart (from Arnold*, Jackson* et al., *Nature* 2022).

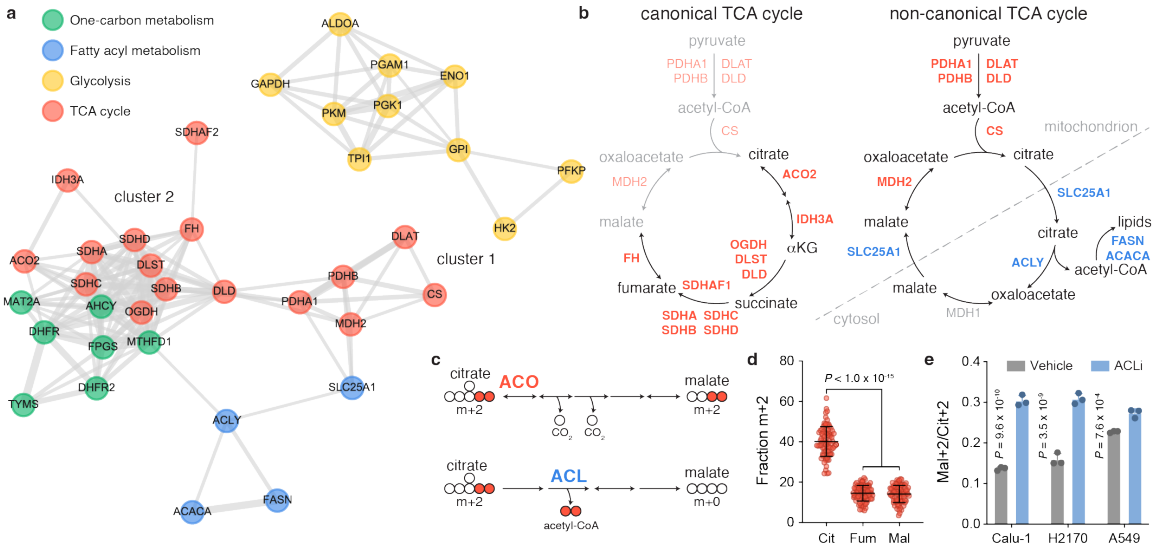

Figure 2.3 Genetic co-essentiality mapping of metabolic enzymes reveals two TCA-cycle modules. a, Two-dimensional network diagram representing gene essentiality score correlations between genes from the indicated pathways (Gene Ontology (GO) terms: TCA cycle, canonical glycolysis, one-carbon metabolic process and fatty-acyl-CoA metabolic process). Correlation strength is shown by the length and thickness of the connecting edge. **b**, Schematic of two TCA-cycle modules that emerge from gene clustering in **a**. Left, cluster-2 genes, associated with the pathway from citrate to malate, are annotated on the traditional TCA cycle. Right, cluster-1 genes are annotated on a non-canonical TCA cycle in which citrate is exported to the cytoplasm and cleaved by ACL to liberate acetyl-CoA and regenerate oxaloacetate, which can yield malate for mitochondrial import and oxaloacetate regeneration. Genes are coloured according to their GO term or grey (no significant correlation). **c**, Schematic of the possible fates for citrate containing 2 carbons derived from [U-^{13}C]glucose. Top, M+2-labelled citrate metabolized by aconitase in the traditional TCA cycle generates M+2-labelled malate. Bottom, M+2-labelled citrate cleaved in the cytoplasm by ACL loses two heavy-isotope-labelled carbons, producing unlabelled four-carbon derivatives. **d**, Fractional M+2 enrichment of TCA-cycle intermediates in 82 NSCLC cell lines cultured with [U-^{13}C]glucose for 6 h. Data were obtained from previously published data[74]. **e**, Fractional enrichment of glucose-derived malate M+2 relative to citrate M+2 (mal+2/cit+2) in NSCLC cell lines after incubation with vehicle or 50 μM BMS- 303141 (ACL inhibitor (ACLi)) for 24 h. Data are mean ± s.d. $n = 3$ independent replicates. Significance was assessed in comparison to citrate using one-way analysis of variance (ANOVA) (**d**) or in comparison to vehicle-treated cells using two-way ANOVA (**e**) with Sidak's multiple-comparisons post-test. Co-essentiality analysis (panel **a**) was performed by the author of this thesis. Panels **b-e** were generated by Paige K. (from Arnold*, Jackson* et al., *Nature* 2022).

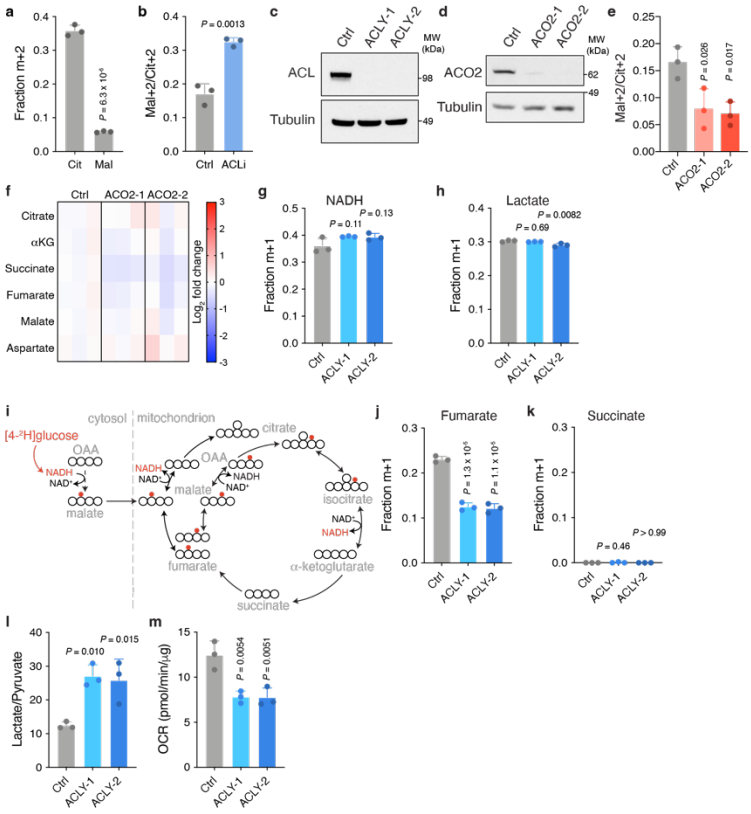

Figure 2.4 ACO2 and ACL disruption in embryonic stem cells. a, Fractional M+2 enrichment of citrate and malate in mouse ES cells cultured in medium containing [U-^{13}C]glucose. **b**, Fractional enrichment of malate M+2 relative to citrate M+2 (mal+2/cit+2) derived from [U-^{13}C]glucose in ES cells following treatment with vehicle or 50 μM BMS-303141 (ACLi) for 24 h. **c**, **d**, Immunoblot of clonal mouse ES cells in which CRISPR/Cas9-mediated editing was used to target either a non-genic region of chromosome 8 (Ctrl) and *Acly* (ACLY-1 and ACLY-2) (**c**) or *Aco2* (ACO2-1 and ACO2-2) (**d**). **e**, **f**, Assessment of the [U-^{13}C]glucose-derived mal+2/cit+2 ratio (**e**) or steady-state levels of TCA cycle metabolites represented as the fold change (expressed in log2) relative to Ctrl (**f**) in control and *Aco2*-edited ES cells. **g**, **h**, **j**, **k**, Fractional M+1 enrichment of NADH (**g**), lactate (**h**), fumarate (**j**) and succinate (**k**) in control and *Acly*-edited ES cells cultured in medium containing [4-^{2}H]glucose. **i**, Schematic depicting deuterium transfer from [4-^{2}H]glucose first onto malate in the cytoplasm then onto TCA cycle metabolites in the mitochondria. **l**, Quantification of the lactate over pyruvate ratio in control and *Acly*-edited ES cells. **m**, The baseline oxygen consumption rate (OCR) in control and *Acly*-edited ES cells normalized to protein content. Twelve technical replicates were averaged for each of three independent experiments. Data are mean ± SD, $n = 3$ independent replicates unless otherwise noted. Significance was assessed using unpaired two-tailed Student's *t*-test (**a**, **b**) or in comparison to control cells by one-way ANOVA with Sidak's multiple comparisons post-test for all other panels. Panels **a-m** were generated by Paige K. Arnold with assistance from Madeleine L. Hart for panels **g-h** (from Arnold*, Jackson* et al., *Nature* 2022).

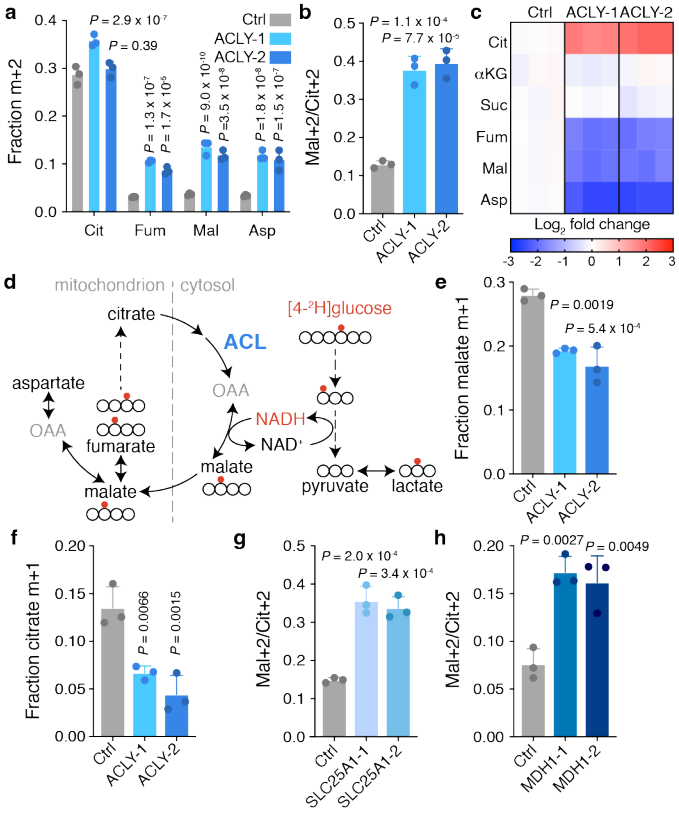

Figure 2.5 ACL loss disrupts TCA-cycle metabolism in ES cells. a, **b**, Fractional M+2 enrichment of citrate (Cit), fumarate (Fum), malate (Mal) and aspartate (Asp) (**a**) or malate M+2 relative to citrate M+2 (mal+2/cit+2) (**b**) in control and *Acly*-edited (ACLY-1 and ACLY-2) mouse ES cells cultured in medium containing [U-^{13}C]glucose. **c**, Steady-state levels of TCA-cycle metabolites in *Acly*-edited mouse ES cells. Levels are represented as the log2-transformed fold change relative to the control cells. αKG, α-ketoglutarate; Suc, succinate. **d**, Schematic of deuterium label transfer from [4-^{2}H]glucose first onto NADH during glycolysis and subsequently onto either malate or lactate in the cytoplasm through MDH1 or LDH activity, respectively. After mitochondrial import, deuterium-labelled malate can be converted to fumarate. The symmetry of fumarate allows the deuterium label to be scrambled, enabling the generation of deuterium-labelled citrate. OAA, oxaloacetate. **e**, **f**, Fractional M+1 enrichment of malate (**e**) or citrate (**f**) in control and *Acly*-edited ES cells cultured in medium containing [4-^{2}H]glucose. **g**, **h**, The mal+2/cit+2 ratio derived from [U-^{13}C]glucose in control and *Slc25a1*-edited (**g**) or *Mdh1*-edited (**h**) ES cells. Data are mean ± s.d. $n = 3$ independent replicates. Significance was assessed using two-way ANOVA (**a**) or one-way ANOVA (**b** and **e**–**h**) with Sidak's multiple-comparisons post-test relative to the controls. Panels **a-h** were generated by Paige K. Arnold (from Arnold*, Jackson* et al., *Nature* 2022).

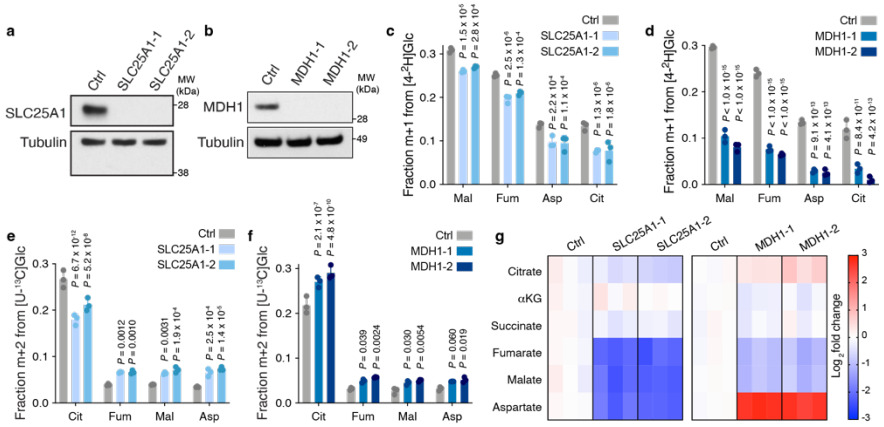

Figure 2.6 SLC25A1 and MDH1 contribute to TCA cycle metabolism in ESCs. a, **b**, Immunoblot of clonal mouse ES cells in which CRISPR/Cas9-mediated editing was used to target either a non-genic region of chromosome 8 (Ctrl) and *Slc25a1* (SLC25A1-1 and SLC25A1-2) (**a**) or *Mdh1* (MDH1-1 and MDH1-2) (**b**). **c**, **d**, Fractional M+1 enrichment of malate (Mal), fumarate (Fum), aspartate (Asp) and citrate (Cit) in control (Ctrl) and *Slc25a1*-edited ES cells (**c**) or *Mdh1*-edited ES cells (**d**) cultured in medium containing [4-^{2}H]glucose. **e**, **f**, Fractional M+2 enrichment of citrate, fumarate, malate and aspartate derived from [U-^{13}C]glucose in control and *Slc25a1*-edited (**e**) or *Mdh1*-edited (**f**) ES cells. **g**, Steady-state levels of TCA cycle metabolites in *Slc25a1*-edited or *Mdh1*-edited ES cells. Levels are represented as the fold change (expressed in log2) relative to chromosome 8-targeted control cells. Data are mean ± SD, $n = 3$ independent replicates. Significance was assessed in comparison to control cells by two-way ANOVA (**c-f**) with Sidak's multiple comparisons post-test. Panels **a-g** were generated by Paige K. Arnold (from Arnold*, Jackson* et al., *Nature* 2022).

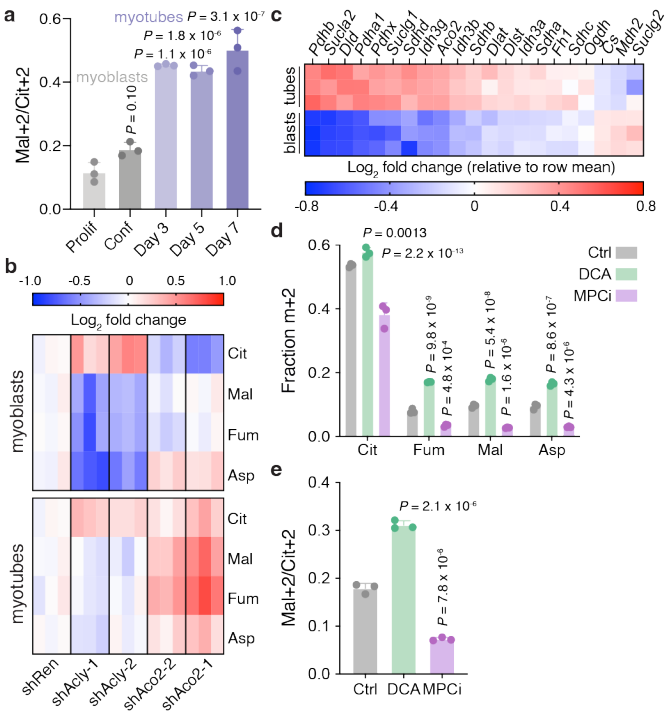

Figure 2.7 Engagement of the non-canonical TCA cycle is cell-state dependent. a, Fractional enrichment of malate M+2 relative to citrate M+2 (mal+2/cit+2) derived from [U-^{13}C]glucose in proliferating (prolif.) and confluent (conf.) myoblasts and myotubes differentiated for 3, 5 or 7 days. **b**, Steady-state levels of citrate, fumarate, malate and aspartate, expressed as the log2-transformed fold change relative to shRenilla, in myoblasts (top) and myotubes (bottom). Myoblasts and myotubes expressing doxycycline-inducible shRNAs targeting *Acly* (shAcly-1 and shAcly-2), *Aco2* (shAco2-1 and shAco2-2) or *Renilla* luciferase (shRen, used as a control) were cultured on doxycycline for two or four days, respectively, to induce shRNA expression. **c**, RNA-seq analysis of TCA-cycle-associated genes in myoblasts (blasts) and myotubes (tubes) that were differentiated for 5 days. Levels are represented as the log2-transformed fold change relative to the row mean. $n = 3$ independently derived samples. **d**, **e**, Fractional M+2 enrichment (**d**) or the mal+2/cit+2 ratio (**e**) derived from [U-^{13}C]glucose in myoblasts after treatment with vehicle (control), 5 mM dichloroacetate (DCA) or 10 μM UK-5099 (MPCi) for 24 h. Data are mean ± s.d. $n = 3$ independent replicates. Significance was assessed in comparison to proliferating myoblasts (**a**) or vehicle treatment (**d** and **e**) using one-way ANOVA (**a** and **e**) or two-way ANOVA (**d**) with Sidak's multiple-comparisons post-test. Panels **a-e** were generated by Paige K. Arnold with assistance from Katrina I. Paras for panel **c** (from Arnold*, Jackson* et al., *Nature* 2022).

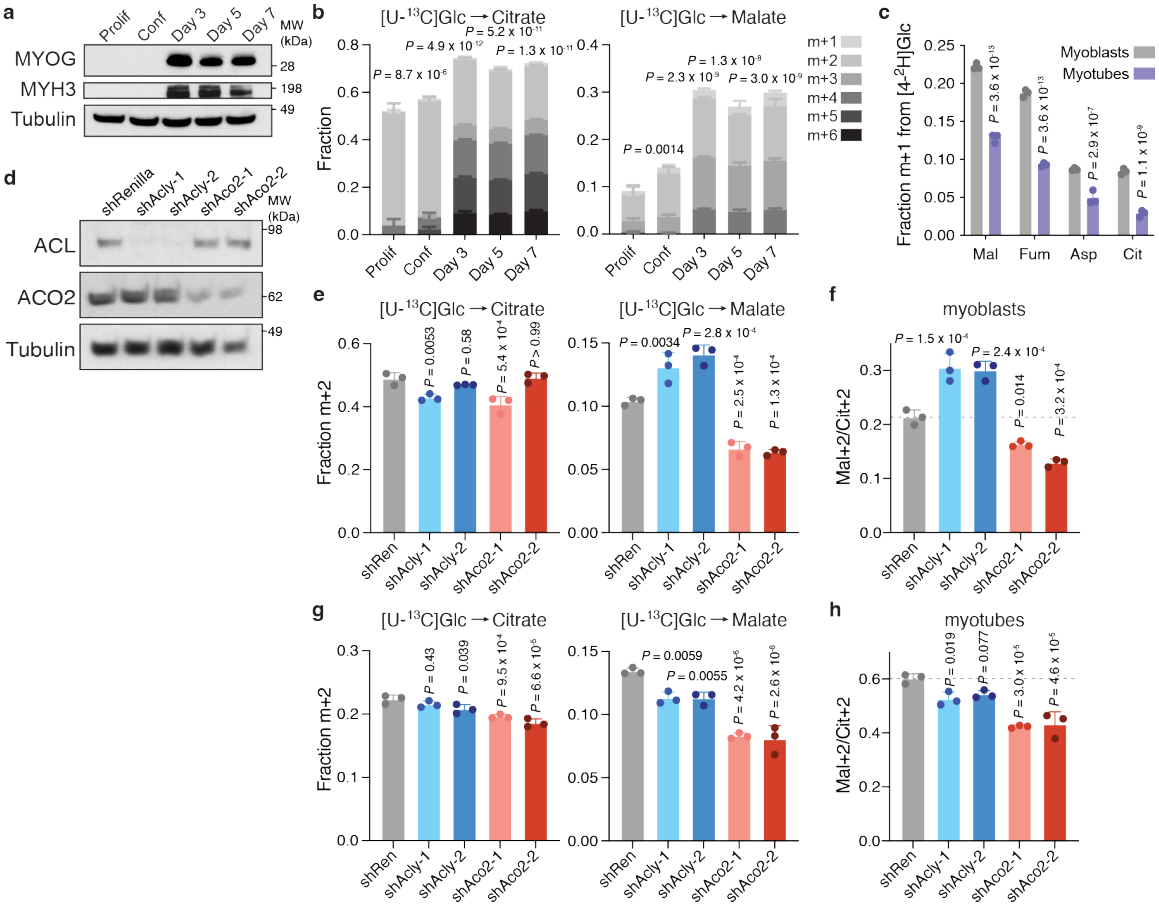

Figure 2.8 Effect of myogenic differentiation on ^{13}C-glucose labeling of TCA cycle intermediates. a, Immunoblot comparing expression of myogenesis markers MYOG and MYH3 between proliferating (Prolif) and 100% confluent (Conf) myoblasts and myotubes differentiated for 3, 5 or 7 days. **b**, Fractional labeling of citrate (left) and malate (right) in proliferating and confluent myoblasts and myotubes differentiated for 3, 5 or 7 days cultured in medium containing [U-^{13}C]glucose. **c**, Fractional M+1 enrichment from [4-^{2}H] glucose of malate (Mal), fumarate (Fum), aspartate (Asp) and citrate (Cit) in myoblasts and myotubes differentiated for 5 days. **d**, Immunoblot comparing expression of ACL and ACO2 in C2C12 cells expressing doxycycline-inducible shRNAs targeting *Acly* (shAcly-1 and shAcly-2), *Aco2* (shAco2-1 and shAco2-2) or Renilla luciferase (shRen, used as a control). Cells were cultured on doxycycline for two days to induce shRNA expression. **e-h**, Fractional M+2 enrichment of citrate (left) and malate (right) or malate M+2 relative to citrate M+2 (mal+2/ cit+2) in myoblasts (**e**, **f**) or myotubes (**g**, **h**) expressing doxycycline-inducible shRNAs targeting *Acly*, *Aco2* or Renilla luciferase cultured in medium containing [U-^{13}C]glucose. Myoblasts and myotubes were cultured on doxycycline for 2 or 4 days, respectively, to induce shRNA expression. Data are mean ± SD, $n = 3$ independent replicates. In **b**, significance was assessed using one-way ANOVA with Sidak's multiple comparisons post-test to compare total metabolite fraction labelled relative to proliferating myoblasts. In remaining panels, significance was assessed by two-way ANOVA in comparison to myoblasts (**c**) or by one-way ANOVA in comparison to shRen-expressing myoblasts (**e-f**) or myotubes (**g-h**) with Sidak's multiple comparisons post-test. Panels **a-h** were generated by Paige K. Arnold (from Arnold*, Jackson* et al., *Nature* 2022).

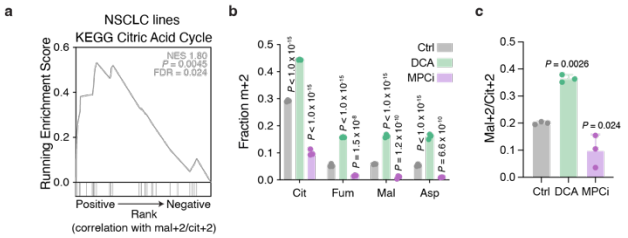

Figure 2.9 Transcriptional profiles associated with TCA cycle choice. a, Gene set enrichment analysis showing that genes positively correlated with fractional enrichment of malate M+2 relative to citrate M+2 (mal+2/cit+2) derived from [U-^{13}C]glucose in 68 NSCLC cell lines are enriched for KEGG citric acid (TCA) cycle-associated genes. **b**, **c**, Fractional M+2 enrichment of citrate (Cit), fumarate (Fum), malate (Mal) and aspartate (Asp) (**b**) or mal+2/cit+2 (**c**) derived from [U-^{13}C]glucose in mouse ES cells following treatment with vehicle, 5 mM DCA or 10 μM MPCi for 24 h. Data are mean ± SD, n = 3 independent samples. In **b-c**, significance was assessed in comparison to vehicle treatment by two-way ANOVA (**b**) or one-way ANOVA **(c)** with Sidak's multiple comparisons post-test. Panels **a-c** were generated by Paige K. Arnold with assistance from Katrina I. Paras for panel **a** (from Arnold*, Jackson* et al., *Nature* 2022).

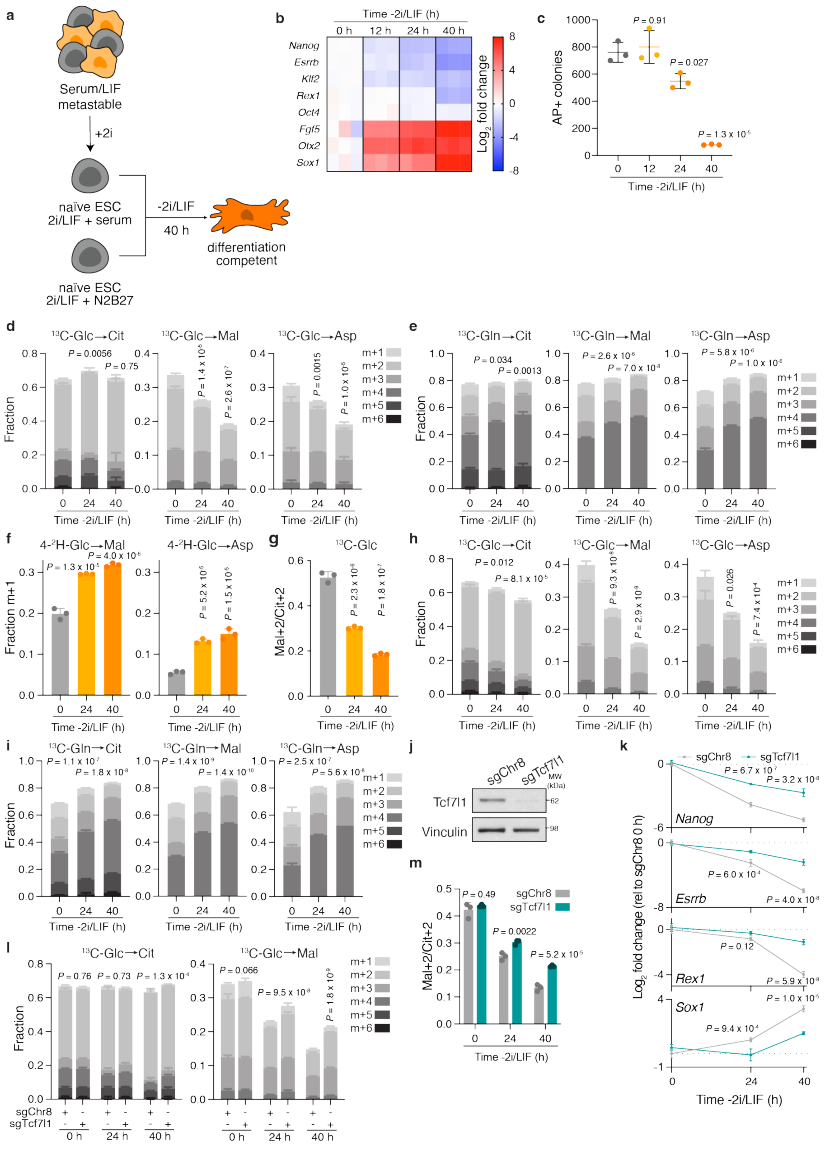

Figure 2.10 ACL loss blunts exit from naive pluripotency. a, Experimental setup for cell fate transitions. Mouse ES cells cultured in serum and leukemia inhibitory factor (LIF) are a heterogenous population that can be converted to the naive, ground state of pluripotency by addition of MEK and GSK3β inhibitors (2i) in either serum replete (serum/LIF+2i, **d-f**) or serum-free (2i/LIF, **g-i**) media formulations. Transition to serum-free medium lacking 2i/ LIF (−2i/LIF) induces exit from the naive pluripotent state, enabling ES cells to gain differentiation competence. **b**, RT–qPCR of pluripotency-associated (*Nanog*, *Esrrb*, *Klf2*, *Rex1* and *Oct4*) and early differentiation-associated (*Fgf5*, *Otx2* and *Sox1*) genes in 2i/LIF-cultured ES cells subjected to 2i/LIF withdrawal for 12, 24 or 40 h. Levels are represented as the fold change (expressed in log2) relative to naive, 2i/LIF-cultured ES cells (0 h). **c**, Quantification of alkaline phosphatase (AP)-positive colonies representing ES cells that failed to exit from the pluripotent state. 2i/LIF-cultured ES cells were subjected to 2i/LIF withdrawal for 0, 12, 24 or 40 h and then reseeded at clonal density into medium containing 2i and LIF. **d-f**, Fractional labeling of citrate (Cit), malate (Mal) and aspartate (Asp) in serum/LIF+2i-cultured ES cells incubated with [U-^{13}C]glucose (**d**),

[U-^{13}C]glutamine (**e**) or [4-^{2}H]glucose (**f**) subjected to exit from pluripotency for the indicated times. **g**, Fractional enrichment of glucose- derived malate M+2 relative to citrate M+2 (mal+2/cit+2) in 2i/LIF-cultured ES cells subjected to 2i/LIF withdrawal for the indicated times. **h**, **i**, Fractional labeling of citrate, malate and aspartate in 2i/LIF-cultured ES cells cultured in medium containing [U-^{13}C]glucose (**h**) or [U-^{13}C]glutamine (**i**) subjected to 2i/ LIF withdrawal for the indicated times. **j**, Immunoblot of polyclonal ES cells in which CRISPR/Cas9-mediated editing was used to target either a non-genic region of chromosome 8 (sgChr8) or *Tcf7l1* (sgTcf7l1). **k**, RT–qPCR of pluripotency-associated (*Nanog*,*Esrrb*, and *Rex1*) and early differentiation- associated (*Sox1*) genes in control and *Tcf7l1*-edited ES cells adapted to the naive, ground state and subjected to 2i/LIF withdrawal for the indicated times. Levels are represented as the fold change (expressed in log2) relative to chromosome 8-targeted control cells in the naive, ground state (0 h). **l**, **m**, Fractional labeling of citrate (left) and malate (right) (**l**) and glucose-derived mal+2/cit+2 ratio (**m**) in chromosome 8-targeted control or *Tcf7l1*- edited ES cells cultured in medium containing [U-^{13}C]glucose subjected to 2i/ LIF withdrawal for the indicated times. Data are mean ± SD, $n = 3$ independent replicates. In **d-e**, **h-i**, and **l**, significance was assessed using one-way ANOVA (**d-e**, **h-i**) or two-way ANOVA (**l**) with Sidak's multiple comparisons post-test to compare total metabolite fraction labelled relative to the 0 h timepoint (**d-e**, **h-i**) or control cells (**l**). In remaining panels, significance was assessed relative to the 0 h timepoint using one-way ANOVA (**c**, **f-g**) or chromosome 8-targeted control cells at each time point using two-way ANOVA (**k**, **m**) with Sidak's multiple comparisons post-test. Panels **a-k** were generated by the author of this thesis (from Arnold*, Jackson* et al., *Nature* 2022).

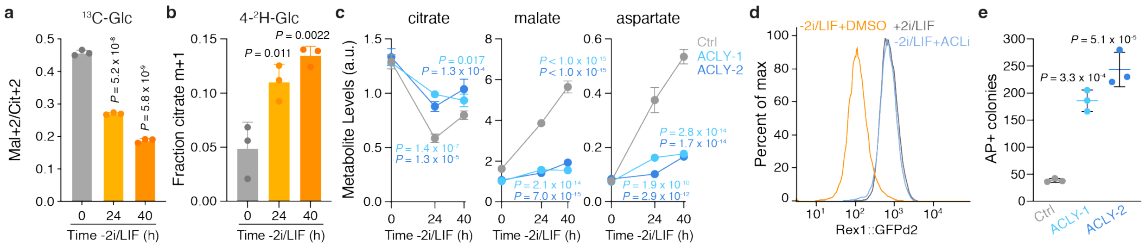

Figure 2.11 Exit from naive pluripotency requires engagement of the non-canonical TCA cycle. a, **b**, Fractional enrichment of malate M+2 relative to citrate M+2 (mal+2/cit+2) derived from [U-^{13}C]glucose (Glc) (**a**) or citrate M+1 derived from [4-^{2}H]glucose (**b**) in ES cells subjected to 2i/LIF withdrawal for the indicated times. **c**, Steady-state levels of metabolites in control and *Acly*-edited ES cells grown under −2i/LIF conditions for the indicated times. **d**, GFP intensity encoded by the *Rex1::GFPd2* reporter in ES cells subjected to 2i/LIF withdrawal for 40 h in the presence of vehicle or 50 μM BMS-303141 (ACLi). Naive ES cells (+2i/LIF) were included as a control. **e**, Quantification of alkaline phosphatase positive (AP^{+}) colonies representing control and *Acly*-edited ES cells that did not exit the naive pluripotent state. 2i-adapted ES cells subjected to 2i/LIF withdrawal for 40 h were reseeded at clonal density into medium containing 2i/ LIF. One histogram representative of four replicates with similar results shown in **d**. For all other panels, data are mean ± s.d. $n = 3$ independent replicates. Significance was assessed using two-way ANOVA with Sidak's multiple-comparisons post-test relative to control cells at each timepoint with *P* values coloured according to comparison (**c**), or by one-way ANOVA in comparison to 0 h (**a** and **b**) or control cells (**e**) with Sidak's multiple-comparisons post-test. Panels **a-e** were generated by the author of this thesis (from Arnold*, Jackson* et al., *Nature* 2022).

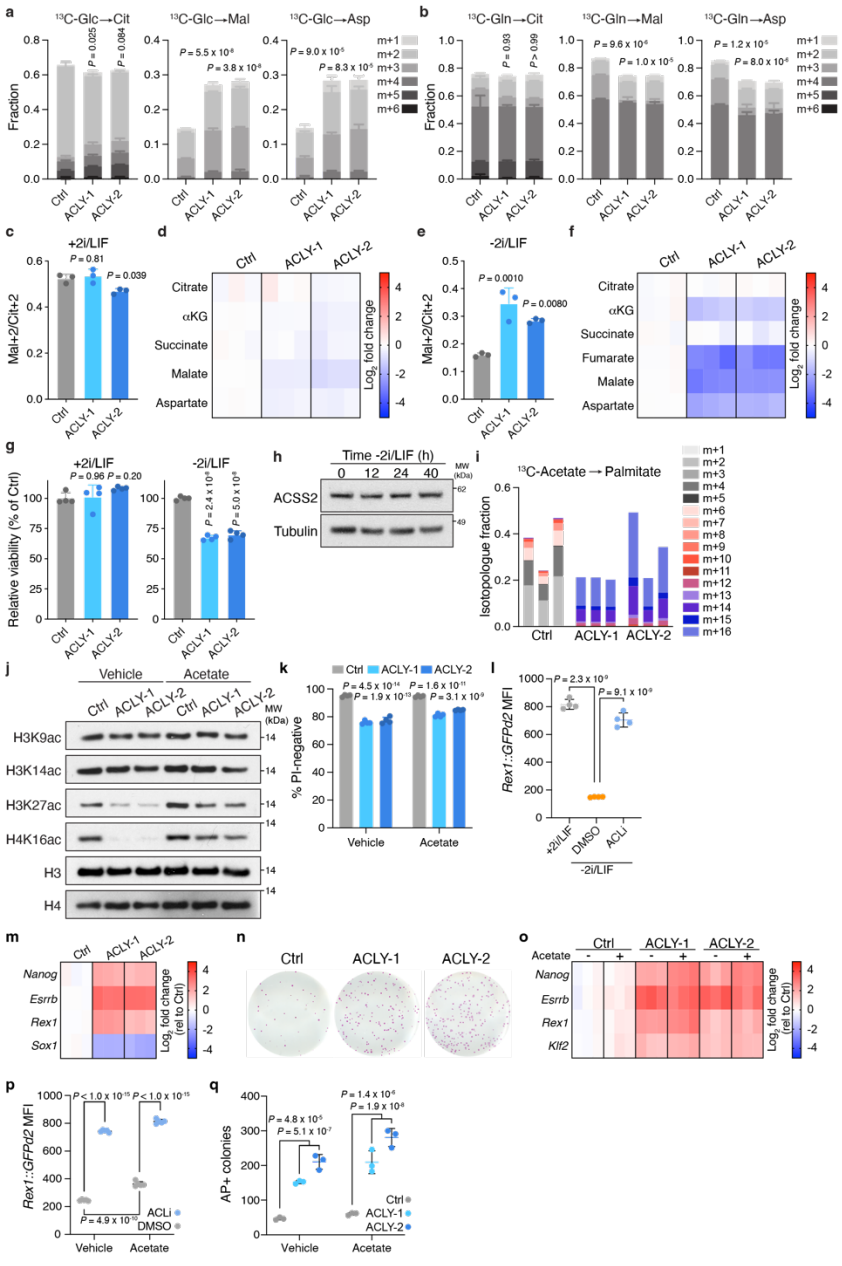

Figure 2.12 Acetate does not reverse the effects of ACL loss on exit from pluripotency. a, **b**, Fractional labelling of citrate (Cit), malate (Mal) and aspartate (Asp) in control and *Acly*-edited ES cells cultured in medium containing [U-^{13}C]glucose (**a**) or [U-^{13}C]glutamine (**b**) following 40 h of 2i/LIF withdrawal. **c**, **d**, Fractional enrichment of malate M+2 relative to citrate M+2 (mal+2/cit+2) derived from [U-^{13}C]glucose (**c**) or steady-state levels of TCA cycle metabolites (**d**) in naive, 2i-adapted control (Ctrl) and *Acly*-edited (ACLY-1 and ACLY-2) ES cells. Steady-state levels are represented as the fold change (expressed in log2) relative to control cells. **e**, **f**, Assessment of the [U-^{13}C] glucose-derived mal+2/cit+2 ratio (**e**) and steady-state levels of TCA cycle metabolites (**f**) in control and *Acly*-edited ES cells subjected to 2i/LIF withdrawal for 40 h. **g**, Relative viability (measured by PI exclusion) of control and *Acly*-edited ES cells maintained in the naive pluripotent state (+2i/LIF, left) or subjected to 2i/LIF withdrawal for 40 h (−2i/LIF,

right). **h**, Immunoblot showing expression of ACSS2, the enzyme that converts acetate to acetyl-CoA in the cytosol, in naive, ground state ES cells subjected to 2i/LIF withdrawal for the indicated times. **i**, Fractional labelling of palmitate in control and *Acly*- edited ES cells cultured in medium containing [U-^{13}C]acetate following 40 h of 2i/LIF withdrawal. Each bar represents one independent sample. **j**, Immunoblot comparing levels of acetylation (ac) at indicated histone lysine residues in control and *Acly*-edited ES cells subjected to 2i/LIF withdrawal for 40 h in the presence of vehicle or 5 mM sodium acetate. **k**, Relative viability of control and *Acly*-edited ES cells subjected to 2i/LIF withdrawal for 40 h in the presence of vehicle or 5 mM sodium acetate. **l**, Quantification of GFP mean fluorescence intensity (MFI) encoded by the *Rex1::GFPd2* reporter in ES cells subjected to 2i/ LIF withdrawal for 40 h in the presence of vehicle or 50 μM BMS-303141 (ACLi). Naïve ES cells (+2i/LIF) are included as a control. Representative histograms are shown in Fig. 4d. **m**, RT–qPCR of pluripotency-associated (*Nanog*, *Esrrb* and *Rex1*) and early differentiation-associated (*Sox1*) genes in control and *Acly*- edited ES cells subjected to 2i/LIF withdrawal for 40 h. Levels are represented as the fold change (expressed in log2) relative to chromosome 8-targeted control cells. **n**, Alkaline phosphatase (AP) staining of colony formation assay representing control and *Acly*-edited ES cells that failed to exit the naive pluripotent state. 2i-adapted ES cells were subjected to 2i/LIF withdrawal for 40 h and then reseeded at clonal density into medium containing 2i/LIF. Quantification is shown in Fig. 4e. **o**, RT–qPCR of pluripotency-associated genes in control and *Acly*-edited ES cells subjected to 2i/LIF withdrawal for 40 h in the presence of vehicle or 5 mM sodium acetate. **p**, Quantification of GFP MFI encoded by the *Rex1::GFPd2* reporter in ES cells subjected to 2i/LIF withdrawal for 40 h in the presence of DMSO or 50 μM BMS-303141(ACLi) and vehicle or 5 mM sodium acetate. **q**, Quantification of AP-positive colonies representing control and *Acly*-edited ES cells that failed to exit from the pluripotent state. ES cells were subjected to 2i/LIF withdrawal for 40 h in the presence of vehicle or 5 mM sodium acetate prior to reseeding at clonal density into medium containing 2i and LIF. Data are mean ± SD, $n = 5$ (**p**), $n = 4$ (**g**, **k**, **l**) or $n = 3$ (all other experiments) independent replicates. In **a-b**, significance was assessed using one-way ANOVA with Sidak's multiple comparisons post-test to compare total metabolite fraction labelled relative to control cells. In remaining panels, significance was assessed by two-way ANOVA relative to control cells (**k**, **q**) or DMSO treatment (**p**) with Sidak's multiple comparisons post-test, or by one- way ANOVA in comparison to control cells (**c**, **e**, **g**) with Sidak's multiple comparisons post-test or in the indicated comparisons (**l**) with Tukey's multiple comparisons post-test. Panel **i** was generated by Oliver J. Newsom. All other panels were generated by the author of this thesis with assistance from Paige K. Arnold for panel **h** (from Arnold*, Jackson* et al., *Nature* 2022).

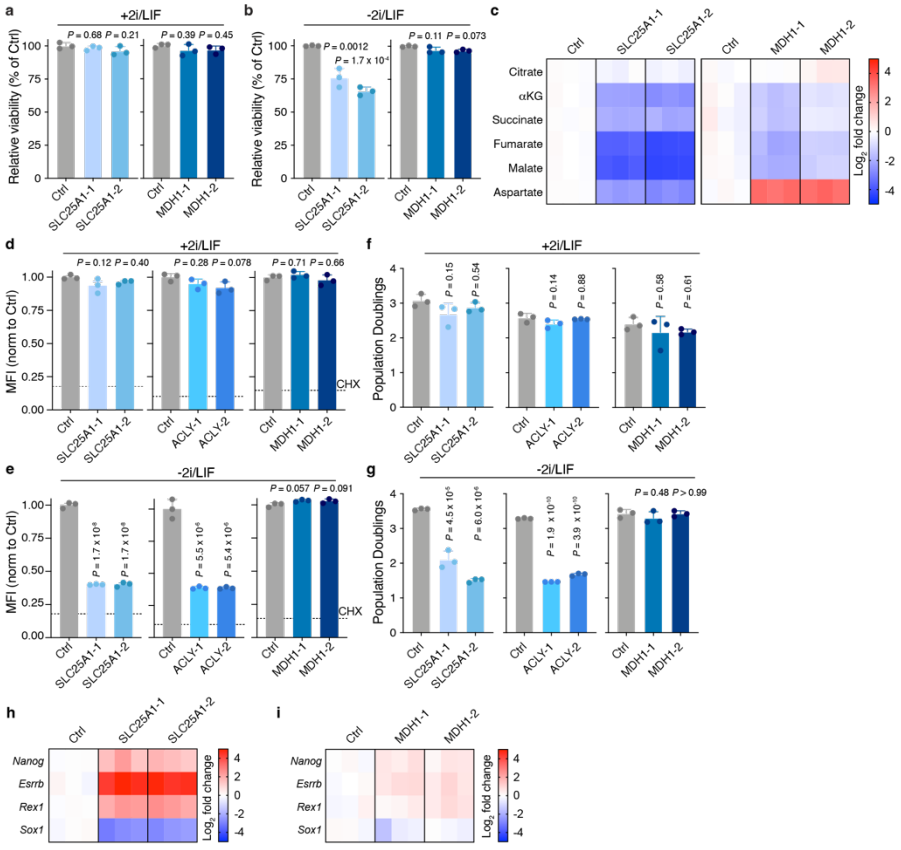

Figure 2.13 Effect of SLC25A1 and MDH1 loss in exit from naive pluripotency. a, **b**, Relative viability (measured by PI exclusion) of control and *Slc25a1*-edited (left) and *Mdh1*-edited (right) ES cells maintained in the naive pluripotent state (+2i/LIF, **a**) or subjected to 2i/LIF withdrawal for 40 h (−2i/LIF, **b**). **c**, Steady-state levels of TCA cycle metabolites in control and *Slc25a1*-edited (left) and *Mdh1*-edited (right) ES cells subjected to 2i/LIF withdrawal for 40 h. Steady-state levels are represented as the fold change (expressed in log2) relative to control cells. **d**, **e**, Relative O-propargyl-puromycin (OP-puro) mean fluorescence intensity (MFI) in control, *Slc25a1*-edited, *Acly*-edited and *Mdh1*-edited ES cells that have been maintained in the naive pluripotent state (**d**) or subjected to 2i/LIF withdrawal for 40 h (**e**). Dotted line represents OP-puro MFI following cycloheximide (CHX) treatment as a control. **f**, **g**, Population doublings of control, *Slc25a1*-edited, *Acly*-edited and *Mdh1*-edited ES cells that have been maintained in the naive pluripotent state (**f**) or subjected to 2i/LIF withdrawal for 40 h (**g**). **h**, **i**, RT–qPCR of pluripotency-associated (*Nanog*, *Esrrb* and *Rex1*) and early differentiation-associated (*Sox1*) genes in control and *Slc25a1*-edited (**h**) and *Mdh1*-edited (**i**) ES cells subjected to 2i/LIF withdrawal for 40 h. Data are mean ± SD, $n = 3$ independent samples. Significance was assessed in comparison to control cells by one-way ANOVA with Sidak's multiple comparisons post-test. Panels **a-i** were generated by the author of this thesis (from Arnold*, Jackson* et al., *Nature* 2022).

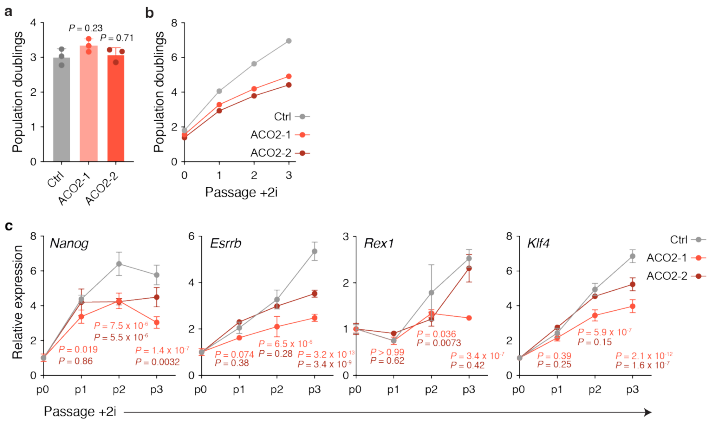

Figure 2.14 Mode of TCA cycle engagement regulates cell fate. a, Population doublings of control and *Aco2*-edited ES cells cultured in metastable (serum/LIF) conditions. **b**, Cumulative population doublings over the indicated passages of control and *Aco2*-edited ES cells upon conversion to the naive, ground state of pluripotency via addition of MEK and GSK3β inhibitors (+2i). **c**, RT–qPCR of pluripotency-associated genes at the indicated passages in control and *Aco2*-edited ES cells following addition of 2i. Gene expression at every passage was normalized to passage 0 (p0). Data are mean ± SD, $n = 1$ (**b**) or $n = 3$ (**a**, **c**) independent replicates. Significance was assessed in comparison to control cells by one-way ANOVA with Sidak's multiple comparisons post-test (**a**) or relative to control cells at each timepoint with *P* values coloured according to comparison by two-way ANOVA with Sidak's multiple comparisons post-test (**c**). Panels **a-c** were generated by Paige K. Arnold with assistance from the author of this thesis (from Arnold*, Jackson* et al., *Nature* 2022).

CHAPTER 3: SELECTIVE PYRUVATE UPTAKE SAFEGUARDS NAIVE PLURIPOTENCY

3.1 Abstract

NAD^+ is a critical cofactor that is reduced to NADH to fuel cellular oxidation reactions that sustain cell proliferation[110]. While many pathways exist for NAD^+ regeneration, how different cell types balance these diverse strategies to maintain redox homeostasis remains poorly understood. Here, we demonstrate that increased pyruvate uptake is a hallmark of naive embryonic stem cells (ESCs) that facilitates NAD^+ regeneration to sustain pluripotent cell growth. We show that the monocarboxylate transporter MCT1 is required, but not limiting, for pyruvate uptake. Rather, mitochondrial pyruvate consumption sets the rate of pyruvate uptake in ESCs. Naive ESCs preferentially utilize pyruvate as a direct TCA cycle substrate, creating a metabolic gradient that drives pyruvate entry into naive cells even at low pyruvate concentrations. Accordingly, naive ESCs cultured in the absence of pyruvate or MCT1-deficient ESCs lose the ability to form naive colonies and sustain levels of TCA cycle intermediates. Alternative electron acceptors or TCA cycle substrates can substitute for pyruvate to support pluripotent cell growth. These findings establish selective pyruvate uptake as a key feature of naive ESCs that supports TCA cycle oxidation and provide insight into the unique metabolic strategies of early development.

3.2 Results

3.2.1 Redox state varies with TCA cycle choice

While all mammalian cells require similar macromolecules to survive and proliferate, different cell types utilize diverse strategies to meet these metabolic demands. Work outlined in **Chapter 2** of this thesis established a non-canonical TCA cycle that is engaged by both cancer

cells and stem cells upon changes in cell state[111]. Otherwise known as the citrate-malate-shuttle (CMS), this pathway encompasses the transport of citrate to the cytoplasm, where it is oxidized prior to reimport into the mitochondria as malate to complete a cross-compartment metabolic cycle (**Figure 3.1a**). One advantage of the CMS is the regeneration of cytosolic NAD^+, in contrast to the mitochondrial TCA cycle that requires the reduction of multiple NAD^+ molecules to NADH to fuel citrate oxidation and regenerate oxaloacetate (**Figure 3.1b**). Loss of the CMS enzyme ACL decreased the cytosolic NAD^+/NADH ratio[111] as assessed by the ratio of pyruvate to lactate[78], confirming that CMS activity contributes to cytosolic redox levels as an electron shuttle (**Figure 2.4l**). However, the precise importance of this aspect of the CMS or alternative methods of cytosolic NAD^+ regeneration to cellular fitness remain unexplored.

NAD^+ is a cofactor used in multiple biosynthetic reactions[110], including the production of aspartate[76,79,86,112], and supports cellular serine and lipid synthesis[113-115]. Recent evidence further suggests that a low NAD^+/NADH ratio may constrain cell proliferation[116]. In most rapidly proliferating mammalian cells, a major route of cytosolic NAD^+ regeneration is the conversion of pyruvate to lactate by lactate dehydrogenase (LDH) and the concomitant oxidation of NADH to NAD^+, commonly termed aerobic glycolysis. However, aerobic glycolysis is redox neutral, as the initial oxidation of glucose requires NAD^+ (**Figure 3.1a,b**). Therefore, electron shuttles such as the CMS provide cytoplasmic NAD^+ that can support cellular proliferation.

We have previously demonstrated that the CMS is engaged by ESCs during the exit from naive pluripotency upon 2i/LIF withdrawal[111]. Conversely, ESCs cultured in the naive, ground state of pluripotency[117] with inhibitors against MEK and GSK3β (2i) predominantly utilize the mitochondrial TCA cycle and therefore lack this pathway of cytosolic NAD^+ regeneration. An additional metabolic hallmark of naive pluripotency is the preferential oxidation of glucose-derived pyruvate in the TCA cycle[47,83]. However, pyruvate oxidation comes at the expense of maintaining redox balance in the cell, as every molecule of pyruvate that is captured in mitochondria is unable to support NAD^+ regeneration in the cytosol (**Figure 3.1a**). Therefore,

enforced pyruvate oxidation creates reductive stress that limits cell proliferation[116]. Indeed, naive ESCs display signatures of reductive stress. ESCs cultured in S/L+2i have a significantly lower pyruvate/lactate ratio than those cultured in S/L (**Figure 3.1d**), consistent with reports that metabolic oxidation increases with cell differentiation[118]. Naive ESCs additionally have decreased levels of serine synthesis from glucose and lower cellular levels of aspartate, both of which are dependent on cellular NAD^+ levels[79,86,113,114] (**Figure 3.1e,f**). Together, these data suggest that naive ESCs are more reduced and are NAD^+ constrained. Here, we leverage metabolic profiling and genetic tools to identify the strategies employed by naive ESCs to meet the demands of NAD^+ regeneration.

3.2.2 Increased pyruvate uptake is a feature of naive pluripotency

In addition to its generation by glycolysis, pyruvate can be directly taken up from the extracellular environment. Proliferation of mammalian cells lacking a functional ETC is boosted by the addition of exogenous pyruvate due to its role as an electron acceptor to regenerate NAD^+ from NADH through LDH[76,119]. However, the importance of pyruvate to maintain NAD^+ levels under physiologic conditions remains unclear. Pyruvate is a ubiquitous addition to ESC culture media, leading us to hypothesize that pyruvate uptake might provide an additional route of NAD^+ regeneration for these cells. We therefore tested whether pyruvate uptake differed significantly in naive or metastable ESCs by measuring media from S/L- or S/L+2i-cultured ESCs. Naive ESCs cultured in S/L+2i consumed more than twofold more pyruvate than their more differentiated counterparts over 24 hours (**Figure 3.2.a**). Pyruvate consumption tracked with acquisition of naive pluripotency, as upon addition of 2i pyruvate uptake was unchanged after 48 hours but increased with successive passages in 2i (**Figure 3.2.b**). Likewise, pyruvate consumption rapidly decreased with loss of the naive pluripotent state[5]. During 40 hours of 2i/LIF withdrawal, ESCs consumed twofold less pyruvate over the final 24 hours relative to 2i/LIF cultured counterparts (**Figure 3.2.c**). ESCs induced to adopt an epiblast-like (EpiLC) cell identity by culture with FGF2

and Activin A[6] likewise decreased pyruvate uptake (**Figure 3.2d**). These results demonstrate that pyruvate uptake is linked to both the establishment and dismantling of the naive pluripotent state by culture with 2i.

To determine whether increased pyruvate uptake is a specific consequence of MEK/GSK3β inhibition or a general figure of cells with higher potential for self-renewal, we took advantage of the population heterogeneity of ESCs cultured in S/L. We utilized previously-generated ESCs harboring a green fluorescent protein (GFP) at the endogenous *Nanog* locus[120]. These Nanog-GFP ESCs have a bimodal GFP distribution under S/L culture conditions, reflecting the functional heterogeneity of these cells where Nanog^{low} cells are more prone to differentiate than their Nanog^{high} counterparts[3,120]. We have previously identified that Nanog^{high} cells similarly demonstrate metabolic characteristics of naive ESCs such as glutamine and leucine independence[62,83]. We sorted cells with both the highest and lowest expression of Nanog to assess if pyruvate uptake differed between these populations (**Figure 3.2e**). Within 3 days of sorting, both Nanog^{high} and Nanog^{low} cells began to reestablish their characteristic bimodal distribution (**Figure 3.2e**). Nevertheless, both sorted populations demonstrated altered pyruvate uptake relative to total population controls, with Nanog^{high} ESCs having higher pyruvate consumption while Nanog^{low} ESCs consumed relatively less extracellular pyruvate (**Figure 3.2f**). Together, these data suggest that enhanced pyruvate uptake is an intrinsic feature of naive pluripotency.

3.2.3 MCT1 is required but is not limiting for pyruvate uptake by naive ESCs

We next probed the molecular mechanisms that enable avid pyruvate consumption by naive ESCs. Pyruvate transport is largely performed by the Slc16 gene family, four of which have been characterized as monocarboxylate transporters[121]. These proteins carry out the co-transport of a monocarboxylate and a proton across the plasma membrane and have been characterized in multiple tissue and cell types (**Figure 3.3a**), but their specific relevance in ESCs has yet to be determined. To identify which transporter carries out pyruvate uptake in naive ESCs we utilized

inhibitors targeting MCT1 and MCT4, which are the most expressed monocarboxylate transporters in ESCs (**Figure 3.3b)**. MCT1 inhibition (MCT1i) had no effect on pyruvate uptake in S/L-cultured ESCs but significantly decreased pyruvate consumption in S/L+2i-cultured ESCs (**Figure 3.3c**). In contrast, MCT4 inhibition did not decrease pyruvate uptake in either culture condition (**Figure 3.4a**). To further support this pharmacological data, we generated clonal ESC lines with genetic disruption of *Slc16a1*, which encodes MCT1 (**Figure 3.4b**). Loss of MCT1 had no consistent effect on pyruvate uptake in S/L-cultured ESCs but reduced pyruvate consumption of naive S/L+2i-cultured ESCs (**Figure 3.3d**). Expression of MCT1 cDNA in MCT1-deficient ESCs restored pyruvate uptake in naive ESCs (**Figure 3.4c,d**), reinforcing its requirement for enhanced pyruvate transport by this cell type.

We next asked whether increased levels of MCT1 enables pyruvate uptake by naive ESCs by generating ESCs expressing MCT1 cDNA (**Figure 3.4e**) Despite localization to the plasma membrane, exogenous MCT1 did not increase pyruvate uptake in either S/L or S/L+2i cultured ESCs (**Figure 3.3e,f**). This data suggests that the amount of MCT1 does not determine pyruvate consumption from the extracellular environment. Consistently, expression of *Slc16a1* was not increased during conversion to the naive state upon the addition of 2i (**Figure 3.3g**). Similarly, *Slc16a1* did not decrease with exit from naive pluripotency (**Figure 3.4f**). We further examined existing proteomic datasets to determine if protein levels of MCT1 tracked with pluripotent state. MCT1 protein levels displayed no consistent change between the naive ground state and metastable culture (**Figure 3.4g,h**). In contrast, RNA and protein levels of MCT4 were significantly increased in more committed ESCs (**Figure 3.3e and Figure 3.4f-h**). MCT4 has a much lower affinity for pyruvate and is thought to function primarily as a lactate exporter for cells[121], and its increased expression is consistent with increased aerobic glycolysis and lactate excretion during ESC differentiation[11] (**Figure 3.4i**). Together, these results indicate that MCT1 is necessary but is not limiting for enhanced pyruvate uptake in the naive pluripotent state.

3.2.4 Pyruvate uptake is set by pyruvate demand

The above results illustrate that MCT1 levels does not set pyruvate uptake in naive ESCs. To identify determinants of pyruvate uptake, we performed genetic co-essentiality mapping utilizing genome-wide CRISPR screens conducted by the DepMap project[70]. In these screens, genes that operate in the same biological pathways demonstrate similar pattens of essentiality which allows for the annotation of genes into functional modules[71]. Co-essentiality analysis has been previously utilized to uncover novel metabolic gene activity and pathway functions[111,122-124]. We reasoned that genes co-essential with the monocarboxylate transporter *Slc16a1* might play similar roles in pyruvate uptake. Unbiased identification of these genes and two-dimensional mapping of their correlation distance revealed multiple gene clusters (**Figure 3.5a**). One gene that was co-essential with *Slc16a1* but clustered independently of other top correlates was its chaperone *Bsg,* confirming the utility of this approach to identify known factors in pyruvate transport. Additionally, a large cluster emerged corresponding to genes involved in mitochondrial metabolism. Similar analysis looking at *Slc16a1* correlation with all genes revealed an enrichment for genes involved in the TCA cycle and oxidative phosphorylation, metabolic pathways in which pyruvate is converted to citrate and consumed (**Figure 3.5b and Figure 3.6a**). These results suggest that pyruvate oxidation may be linked to its extracellular uptake.

We therefore asked whether altering pyruvate mitochondrial utilization affected its uptake from the extracellular environment (**Figure 3.6b**). Pharmacologic inhibition of the mitochondrial pyruvate carrier (MPCi) completely eliminated pyruvate consumption in both S/L and S/L+2i cultured ESCs (**Figure 3.5c**). Reciprocally, treatment with dichloroacetate to potentiate PDHC activity[82] significantly increased pyruvate uptake in S/L cultured ESCs (**Figure 3.5d**). Thus, pyruvate uptake can be determined by changing the amount of pyruvate captured for oxidation in the mitochondria.

The fact that increasing mitochondrial pyruvate capture in S/L-cultured ESCs increased extracellular pyruvate uptake suggested that naive ESCs might preferentially utilize pyruvate as a

TCA cycle substrate relative to their more differentiated counterparts. Indeed, tracing of [U-^{13}C]pyruvate revealed that S/L+2i-cultured ESCs incorporated twofold more pyruvate-derived carbon into citrate than S/L-cultured ESCs (**Figure 3.5e)**. We further evaluated whether ESCs utilize pyruvate as a fuel source by monitoring oxygen consumption rates upon the addition of FCCP (**Figure 3.6c**). While naive and metastable ESCs had no difference in maximal respiration in media containing glucose alone, addition of 0.2 mM or 1 mM of pyruvate significantly increased respiration in S/L+2i-cultured ESCs relative to S/L (**Figure 3.5f and Figure 3.6d**). Conversely, S/L+2i-cultured ESCs preferentially utilized glutamine as a fuel for respiration, consistent with their increased incorporation of glutamine into TCA cycle intermediates[47,83]. The ability of naive ESCs to utilize pyruvate for respiration was abolished in cells deficient for MCT1 (**Figure 3.5g and Figure 3.6e**), confirming that differential pyruvate uptake enables its usage as a substrate for respiration.

3.2.5 Naive ESCs are dependent on pyruvate uptake

In naive ESCs, pyruvate oxidation in the mitochondria drives its uptake from the extracellular environment. This raises the possibility that metabolite consumption can create gradients that dictate nutrient flow into or out of the cell. Under this model, nutrients are taken up until an equilibrium is formed between the intracellular and extracellular environment at a metabolite concentration dictated by the specific metabolic demands of the cell. Because naive ESCs have higher pyruvate demand, we hypothesized that they would retain the ability to take ability to take up pyruvate even in low pyruvate conditions. We measured pyruvate uptake in S/L- and S/L+2i-cultured ESCs at a range of pyruvate concentrations. Strikingly, S/L+2i-cultured ESCs consumed pyruvate from media at pyruvate concentrations as low as one tenth normal media amounts (**Figure 3.7a**). Conversely, S/L-cultured ESCs net excreted pyruvate in media with pyruvate concentrations below 0.5 mM. When no pyruvate was present in the media, all ESCs released pyruvate to the extracellular environment. These results are consistent with a

model where pyruvate is taken up or excreted until intracellular and extracellular pyruvate are at an equilibrium concentration that is lower in naive ESCs.

While pyruvate is often supplemented into ESC culture media at 1 mM concentrations, the level of pyruvate in most biological fluids including serum or in the maternal reproductive tract where embryonic development occurs is thought to be 0.2 mM[60]. This concentration corresponds to the set point at which naive ESCs consume pyruvate while pyruvate is excreted by their more committed counterparts (**Figure 3.7a**). Inhibition or loss of MCT1 abrogated both excretion of pyruvate in S/L-cultured ESCs and its uptake in S/L+2i-cultured ESCs in media containing 0.2 mM pyruvate (**Figure 3.8a,b**), consistent with the bidirectional monocarboxylate transport of the Slc16 gene family. Restoration of MCT1 expression in MCT1-deficient ESCs likewise restored pyruvate uptake in naive ESCs at this physiologic pyruvate concentration (**Figure 3.8c**).

We hypothesized that withdrawal of exogenous pyruvate below its set intracellular concentration should enforce its excretion from the cell and impair naive ESC function. Pioneering studies by Eagle demonstrated that cells exhibit population-dependent dependencies for specific metabolites—including pyruvate—that are due to loss of these critical metabolites from the cell to the environment at low cell density[125]. Therefore, we performed colony-formation assays with S/L+2i-cultured ESCs where cells are seeded at clonal density in media containing a range of pyruvate concentrations. Naive ESCs formed equal numbers of colonies in media containing 1 mM or 0.2 mM pyruvate, consistent with our data that pyruvate is net consumed in these conditions (**Figure 3.7a-c**). However, colony formation was significantly impaired in media without pyruvate supplementation (**Figure 3.7b-c**). These data reveal that excessive loss of pyruvate to the extracellular environment limits naive ESC colony formation.

While culture in media without pyruvate potentiates pyruvate efflux from the cell, loss of MCT1 in cells cultured in media with pyruvate restricts pyruvate import. We hypothesized that cells deficient for MCT1 would have impaired colony forming ability. Consistent with impaired

pyruvate import in media containing 1 mM pyruvate, MCT1-deficient ESCs formed fewer colonies and were rescued by expression of MCT1 cDNA (**Figure 3.7d,e**). Further supporting a model where restricting pyruvate availability limits naive ESC function, loss of MCT1 was potentiated at 0.2 mM and 0 mM pyruvate concentrations (**Figure 3.7f**). Additionally, MCT1-deficient ESCs cultured in S/L+2i had impaired growth at standard culturing densities in media containing 0.2 mM pyruvate (**Figure 3.7g**).

To evaluate whether the detrimental effects of pyruvate withdrawal or MCT1 deficiency were specific to the naive state, we tested the role of pyruvate in more differentiated ESCs. In contrast to impeding cell growth in naive ESCs, loss of MCT1 in S/L-cultured ESCs resulted in a minor increase in proliferation (**Figure 3.9a**). MCT1-deficient ESCs remained competent for multilineage differentiation, as embryoid bodies formed from these cells effectively decreased markers of the pre-implantation epiblast and increased expression of markers of all three germ layers (**Figure 3.9b**).

The above results suggest that pyruvate dependency is a specific metabolic vulnerability of naive ESCs. To test this hypothesis, we exploited the phenotypic heterogeneity of ESCs cultured in S/L. Using our Nanog-GFP reporter line, we cultured ESCs in media with or without pyruvate and evaluated the proportion of cells expressing high levels of Nanog. Pyruvate withdrawal significantly decreased the proportion of $Nanog^{high}$ cells (**Figure 3.7h,i**), consistent with our data that these cells consume relatively more pyruvate (**Figure 3.2f**). Similarly, S/L-cultured ESCs subjected to colony-forming assays in media without pyruvate formed fewer overall colonies that were less likely to be undifferentiated (**Figure 3.9c,d**). Together, these results demonstrate that reliance on pyruvate uptake is a selective vulnerability of cells in the naive pluripotent state.

3.2.6 Pyruvate uptake sustains redox balance and TCA cycle metabolism in ESCs

We next asked what metabolic output downstream of pyruvate was required for naive ESC function. To assess the relevance of pyruvate utilization as a TCA cycle substrate, we inhibited the mitochondrial pyruvate carrier (MPCi). In contrast to loss of MCT1, MPCi had no effect on naive colony formation (**Figure 3.10a**). Similarly, the addition of lactate—which can be converted to pyruvate by LDH—did not rescue naive colony formation in media containing 0 mM pyruvate despite lactate supplementation at ten times normal pyruvate concentrations (**Figure 3.10b**). Because lactate is the reduced form of pyruvate and plays an opposing role in maintaining cellular redox balance through the LDH reaction, we hypothesized that pyruvate is required in naive ESCs for NAD^+ regeneration. Indeed, measurement of the pyruvate/lactate ratio that varies specifically with cytosolic $NAD^+/NADH$[78] demonstrated that naive ESCs cultured in decreasing amounts of pyruvate or ESCs lacking MCT1 are more reduced (**Figure 3.11a,b**). These data suggest that pyruvate uptake contributes to maintenance of redox state in naive ESCs.

Therefore, we tested the alternative methods of NAD^+ regeneration in naive ESCs. Alpha keto-butyrate (αKB) has been previously shown to substitute for pyruvate as a substrate for LDH or other intracellular dehydrogenases as an alternative electron acceptor[76] (**Figure 3.10c**). In line with these reports, addition of αKB partially rescued the pyruvate/lactate ratio in SL+2i-cultured ESCs in the absence of pyruvate (**Figure 3.10d**). αKB supplementation likewise restored naive colony formation in media containing 0 mM pyruvate (**Figure 3.11c**). To further test the relevance of $NAD^+/NADH$ alterations in naive ESCs, we generated ESCs expressing *Lactobacillus brevis* NADH oxidase (*Lb*NOX), an enzyme capable of oxidizing NADH to NAD^+ using molecular oxygen (**Figure 3.10c,e**). Expression of *Lb*NOX was sufficient to increase the pyruvate/lactate ratio in S/L+2i-cultured ESCs (**Figure 3.10f**) and partially rescue naive colony formation in media without pyruvate (**Figure 3.11d**). Similarly, *Lb*NOX-expressing ESCs were resistant to the effects of MCT1 inhibition on naive colony formation (**Figure 3.11e**). Together, these results indicate that restoring $NAD^+/NADH$ balance can mitigate the effects of pyruvate withdrawal on naive ESCs.

While interventions restoring the NAD^+/NADH ratio were able to substitute for pyruvate supplementation or MCT1 function, the possibility remains that these approaches work by sparing glucose-derived pyruvate to act as a direct fuel for TCA cycle metabolism. We therefore examined the effect of decreased pyruvate uptake on levels of TCA cycle metabolites. Loss of MCT1 substantially lowered levels of TCA-cycle metabolites downstream of citrate (**Figure 3.11f**). Consistent with the hypothesis that alternative electron acceptors can increase mitochondrial capture of pyruvate for oxidation, αKB supplementation increased levels of TCA cycle intermediates in media without pyruvate (**Figure 3.10g**). These data suggest that pyruvate supports naive ESC function both through redox balance and as a TCA cycle substrate.

We further dissected the role of pyruvate as a TCA cycle fuel by providing naive ESCs with an alternative TCA cycle source to compensate for the absence of pyruvate. Dimethyl alpha-ketoglutarate (DM-αKG) is a cell-permeable form of alpha-ketoglutarate that can support ESC proliferation in the absence of glutamine[47,83]. Addition of DM-αKG completely restored TCA cycle intermediates in naive ESCs cultured without pyruvate (**Figure 3.10h**). Importantly, DM-αKG did not increase the pyruvate/lactate ratio in naive ESCs, indicating that this effect on metabolite pools was independent of changes in overall redox state (**Figure 3.10i**). Strikingly, DM-αKG partially rescued naive colony formation in media containing 0 mM pyruvate and in MCT1-deficient ESCs (**Figure 3.11g,h**). Thus, our results indicate that enhanced pyruvate uptake supports both NAD^+ regeneration and TCA cycle metabolism and that these functions are critical to support the naive pluripotent state.

3.3 Discussion

Here, we identify enhanced pyruvate uptake as a hallmark of naive pluripotency that is selectively engaged by naive ESCs to cope with reductive stress and sustain cellular anabolism. While pyruvate is a common cell culture additive, this study enforces that its uptake may be cell-type specific. Monocarboxylate transporters such as MCT1 or MCT4 are differentially expressed

in many cell types[126], but this study suggests their levels alone might be permissive rather than rate-limiting for pyruvate uptake. Instead, pyruvate uptake is a function of both its extracellular concentration and pyruvate usage for intracellular metabolism. A recent report indicated similar bidirectional transport drives amino acid homeostasis[127], enforcing the paramount role of metabolic demand as the driver of nutrient uptake.

The precise downstream metabolic outputs of pyruvate that support the naive state remain to be fully elucidated. While previous studies have shown pyruvate addition can alter redox ratios within cancer cells[128], our data indicate that pyruvate uptake is required to maintain NAD^+/NADH levels specifically in naive ESCs. This combination of redox balance with mitochondrial pyruvate oxidation allows pyruvate to serve as a dual fuel for cell proliferation. These findings lay the groundwork for future studies investigating the role of pyruvate uptake in embryonic development and disease.

3.4 Experimental Methods

Cell culture

Mouse ESCs were generated previously from C57BL/6 × 129S4/SvJae F_1 male embryos[47]. Nanog-GFP ESCs were a gift from R. Jaenisch[120]. For all experiments, ESCs were maintained on gelatin-coated plates in the following media formulations: serum/LIF, serum/LIF+2i, and 2i/LIF. Serum/LIF media was composed of knockout DMEM (10829018; Thermo Fisher Scientific) supplemented with 10% fetal bovine serum (FBS; Gemini), 0.1 mM 2-mercaptoethanol, 2 mM L-glutamine and 1000 U/mL LIF (Gemini). Serum/LIF+2i ESCs were converted to the naive state by the addition of 3μM CHIR99021 (Stemgent) and 1μM PD0325901 (Stemgent) to serum/LIF media. 2i/LIF media contained a 1:1 mix of DMEM/F-12 (11320033; Gibco) and Neurobasal medium (21103049; Gibco), N2-supplement (17502048; Gibco) B27-supplement (17504044; Gibco), 0.1 mM 2-mercaptoethanol, 2 mM L-glutamine, LIF and 2i. Both

2i/LIF and serum/LIF+2i ESCs were generated by adapting serum/LIF-cultured ESCs for at least three passages, and adapted cells were used for a maximum of nine passages.

To induce exit from naive pluripotency, 2i/LIF-cultured ESCs were seeded in their maintenance media for 24h prior to washing with PBS and changing into maintenance medium without 2i and LIF for 40h prior to harvest. For EpiLC differentiation, 2i/LIF-cultured ESCs were seeded directly into Fibronectin-coated plates in media containing a 1:1 mix of DMEM-F12 and Neurobasal medium supplemented with N2 (1:200), B-27 (1:100), 2 mM L-glutamine, 0.1 mM 2-mercaptoethanol, 12 ng/mL FGF2, 20 ng/mL Activin A and 1% Knockout serum replacement. EpiLCs were harvested 48 hours after seeding.

Nutrient consumption

For serum/LIF and serum/LIF+2i experiments, ESCs were seeded in 6-well plates in maintenance media. 24h prior to harvest, cells were washed with PBS and 1 mL of media was added consisting of a 1:1 mix of DMEM/Neurobasal media without pyruvate, 10% dialyzed FBS (Gemini), 0.1 mM 2-mercapto-ethanol, 2 mM L-glutamine, 1000 U/mL LIF and indicated concentrations of sodium pyruvate (Gibco) with or without 2i. For 2i/LIF experiments, dialyzed FBS was replaced with N2 and B27 supplement. For EpiLC experiments, dialyzed FBS was replaced with N2, B27, and KSR supplements along with FGF2 and Activin A. For each experiment, a plate of media without cells was seeded as a control for normalization. At the time of harvest, media samples were collected and spun down at 1,700 x *g* for 5 minutes in a pre-chilled centrifuge. 10-50 µL of supernatant per sample was mixed with 1 mL of ice-cold 80% methanol supplemented with 2µM deuterated 2-hydroxyglutarate (*D*-2-hydroxyglutaric-2,3,3,4,4-d_5 acid (d5-2HG)) as an internal standard. Samples were incubated overnight at -80°C and spun down at 20,000 x *g* for 20 minutes at 4°C. Supernatants were dried in an evaporator (Genevac E-2 Elite) and processed for GC-MS analysis as detailed below.

Metabolic analyses

To assess intracellular metabolite pools, ESCs were seeded in standard culture media in six-well plates. 24h later, cells were washed with PBS and changed into media containing of a 1:1 mix of DMEM/Neurobasal media without pyruvate, 10% dialyzed FBS, 0.1 mM 2-mercapto-ethanol, 2 mM L-glutamine, 1000 U/mL LIF and indicated concentrations of pyruvate with or without 2i. 4h prior to harvest, cells were washed with PBS and identical media was refreshed. For [U-^{13}C]pyruvate tracing, this same pyruvate free media was supplemented with 1mM either [^{12}C] pyruvate or its labeled version [U-^{13}C]pyruvate (Cambridge Isotope Laboratories). Cells were harvested after 1h. For [U-^{13}C]glucose tracing, media was changed to a 1:1 combination of glucose- and glutamine-free DMEM and glucose- and glutamine-free Neurobasal-A media with 10% dialyzed FBS, 0.1 mM 2-mercaptoethanol, 2mM L-glutamine, and LIF with or without 2i. This media was supplemented with either [^{12}C]glucose (Sigma-Aldrich) or its labeled version [U-^{13}C]glucose (Cambridge Isotope Laboratories) to a final concentration of 20 mM. Cells were harvested after 4h.

For all samples, metabolites were extracted at collection with 1 mL ice-cold 80% methanol containing d5-2HG. After overnight incubation at 80°C lysates were centrifuged at 20,000 x g for 20 minutes to remove protein. Supernatants were dried in an evaporator (Genevac E-2 Elite) and processed for GC-MS analysis as detailed below.

GC-MS analysis

Dried extracts were resuspended in 50 µL of 40 mg/mL methoxyamine hydrochloride in pyridine and incubated at 30°C for 2h with shaking. Metabolites were further derivatized by adding 80 µL of *N*-methyl-*N*-(trimethylsilyl) trifluoroacetamide (Thermo Fisher Scientific) and 70 µL ethyl acetate (Sigma-Aldrich) prior to 30 minutes of incubation at 37°C. Samples were analyzed using an Agilent 7890A gas chromatograph coupled to an Agilent 5977C mass selective detector. The gas chromatograph was operated in splitless injection mode and helium gas flow was constant at 1 mL/min. 1 µL of each sample was injected onto an HP-5ms column and the gas chromatograph oven temperature increased over 25 min from 60-290°C. MassHunter v.B.08 was used to extract

and integrate peaks representing compounds of interest. For nutrient consumption analysis, peak values were normalized to the internal standard (d5-2HG) peak and the delta was calculated with media-only controls to determine the amount of each metabolite that was consumed. This difference was normalized to protein content of samples as determined using the bicinchoninic acid assay (Thermo Fisher Scientific). For intracellular metabolite pools, peaks were normalized to d5-2HG and protein content. The following ions were used for quantification: d5-2HG, 354 *m/z*; αKG, 304 *m/z*; aspartate, 334 *m/z*; citrate, 363 *m/z*; lactate, 219 *m/z*; malate, 335 *m/z*; pyruvate, 115 *m/z*; and succinate, 247 *m/z.* Known spectra for each metabolite was used to verify peak identity. Enrichment of [^{13}C] was assessed by quantifying the abundance of the following ions: citrate, 465-471 *m/z*; serine, 306-309 *m/z*. Natural isotope abundance correction was performed using IsoCor v2.0[105].

Generation of clonal ES cell lines

Single guide RNA (sgRNA) sequences targeting *Slc16a1* or a control, non-genic region on mouse chromosome 8[100] were cloned into the pSpCas9(BB)-2A-GFP plasmid (PX458, Addgene #48138) as previously described[103]. sgRNA sequences are provided in **Table 4**. A 4D-Nucleofector (Amaxa, Lonza) was used to electroporate ESCs (4 x 10^5 per condition) with 5 µg of PX458 plasmid. Electroporated cells were plated on mitotically inactivated feeder mouse embryonic fibroblasts (MEFs). After 48h, cells were dissociated with Accutase (Invitrogen) and sorted on a BD FACSAria III sorter (BD Biosciences) to enrich for GFP-positive cells. Less than 10,000 GFP-positive cells were reseeded on 10 cm plates with MEFs to enable clonal growth. After 7 days, individual clones were picked and expanded to MEFs and eventually gelatin-coated plates prior to confirmation of genetic editing by immunoblot.

Table 4: Chapter 3 sgRNA primer sequences

Chr.8 Control	CACCGACATTTCTTTCCCCACTGG
	AAACCCAGTGGGGAAAGAAA TGTC
Slc16a1 sg	CACCGTGGCGTGATCCTCATCATCG

	AAACCGATGATGAGGATCACGCCAC

Generation of MCT1 or LbNOX expressing ESCs

Either *Slc16a1* (Horizon Discovery, 3499773) or *Lb*NOX (Addgene #75285) was cloned into Piggybac (pCAGGS-IRES-Neo, a gift from H. Niwa). ESCs were electroporated with either vector control or Piggybac plasmids containing genes of interest plus transposase (pBase) at a ratio of 3:1 using a 4D-Nucleofector. After electroporation, cells were seeded on MEFs and 48h later selection was initiated with G418 (300 μg/mL). Expression was confirmed by immunoblot.

Colony-formation assay

ESCs maintained in either serum/LIF or serum/LIF+2i were counted and seeded in media containing a 1:1 mix of DMEM/Neurobasal media without pyruvate, 10% dialyzed FBS, 0.1 mM 2-mercaptoethanol, 2 mM L-glutamine, indicated sodium pyruvate concentration and LIF with or without 2i. Other metabolite or drug interventions were added as indicated. For MPCi or MCT1i, cells were pre-treated for 48h prior to harvest with either drug or vehicle control. Cells were seeded in groups of 6 replicates at a density of 500 cells per well of a 6-well plate. Media was refreshed 3 days after seeding. At 6 days post seeding, cells were fixed with citrate/acetone/3% formaldehyde and stained with Leukocyte Alkaline Phosphatase Kit (Sigma-Aldrich) according to manufacturer's instructions. For serum/LIF assays, colonies were classified as differentiated, mixed and undifferentiated by an unblinded investigator.

Growth curves

ESCs were seeded at a density of 40,000 cells/well in 12-well plates into media containing a 1:1 mix of DMEM/Neurobasal media without pyruvate, 10% dialyzed FBS, 0.1 mM 2-mercaptoethanol, 2 mM L-glutamine, 0.2 mM sodium pyruvate and LIF with or without 2i. Replicate plates were seeded for each day of the assay. Cells were harvested and counted each day using a Beckman Coulter Multisizer 4e gated at 400-10,000 fL.

Embryoid bodies

ESCs maintained in serum/LIF+2i were seeded in 96-well low attachment plates (MS-9096UZ, Sbio) at 5000 cells/well in maintenance media without LIF or 2i. Media was refreshed every 2-3 days. After 4 or 8 days, 8 wells were pooled to form one biological replicate. For day 0 controls, serum/LIF+2i cells seeded in 12-well plates in maintenance media were used. Embryoid bodies or cells were harvested in TRIzol (Invitrogen) for quantification of gene expression as below.

Oxygen consumption

Oxygen consumption rate (OCR) was measured using a Seahorse XFe96 Extracellular Flux Analyzer (Agilent Technologies). ESCs were plated on gelatin-coated tissue-culture-treated XF96 96-well plates (Agilent Technologies) in standard maintenance medium. The next day, cells were washed with assay medium composed of Seahorse XF DMEM medium supplemented with 10 mM glucose. Baseline measurements of OCR were obtained three times prior to injection with indicated substrates, FCCP, and rotenone/antimycin A. OCR was measured three times after each injection. After the assay, protein content was determined and averaged for each condition for OCR normalization. For maximum respiration measurements, the first measurement after FCCP injection is shown.

Immunofluorescence

Serum/LIF cultured ESCs were seeded in gelatin-coated glass chamber slides. For immunofluorescence, cells were fixed in 4% PFA for 10 minutes and then blocked at room temperature for 1 h in 1% BSA and 0.3% TritonX-100 in PBS. Samples were incubated in primary antibody overnight at 4°C, washed in PBS and exposed to secondary antibody for 1 h at room temperature. 4', 6 Diamidino 2 Phenylindole, Dihydrochloride (DAPI; Thermo Fisher Scientific) was added prior to imaging. HA-tagged proteins were detected using a primary anti-HA antibody (C29F4, Cell Signaling Technology) and secondary anti-Rabbit antibodies conjugated to Alexa Fluor-647. Images were acquired on a Leica SP5 inverted confocal microscope using a x20 water-immersion objective and were processed using ImageJ.

Nanog-GFP analysis

Nanog-GFP ESCs were cultured in serum/LIF media. To assess the effects of pyruvate withdrawal on Nanog-GFP distribution, cells were seeded in media containing a 1:1 mix of DMEM/Neurobasal without pyruvate, 10% dFBS, 0.1 mM 2-mercaptoethanol, 2 mM L-glutamine and LIF with or without 1 mM pyruvate supplementation. 48 h later, cells were harvested and resuspended in flow cytometry buffer (PBS with 2% FBS, 0.5 mM EDTA and 0.05% sodium aide) with DAPI. GFP signal was measured on an LSRFortessa flow cytometer using FACSDiva software v.8.0 (BD Biosciences) and analyzed using FlowJo v10.9.0.

Western blotting

Protein lysates were extracted in 1X RIPA buffer (Cell Signaling Technology). Equal amounts of protein were separated by SDS-polyacrylamide gel electrophoresis and transferred to nitrocellulose membranes (Bio-Rad). Membranes were blocked in 3% milk in Tris-buffered saline with 0.1% Tween (TBST) and incubated with primary antibodies overnight. The next day, membranes were washed with TBST and incubated with horseradish-peroxidase-conjugated secondary antibodies (mouse, NA931; rabbit, NA934; Cytiva) for at least 2 h. Signal was visualized using enhanced chemiluminescence (Thermo Fisher Scientific) and imaged using an SRX-101A X-ray Film Processor (Konica Minolta). The antibodies used were as follows: anti-MCT1 (1:1000, ab85021, Abcam); anti-HA (1:1000, C29F4, Cell Signaling Technology); anti-Flag (1:500, F1804, Sigma); anti-vinculin (1:10,000; V9131; Sigma).

Proteomics analysis

Proteomics data were obtained from Atlasi et al[129]. Values were calculated as log2-fold change relative to either 2i/LIF or serum/LIF conditions.

Quantification of gene expression

RNA was isolated from cells or embryoid bodies using TRIol (Invitrogen) according to manufacturer's instructions. The iScript cDNA synthesis Kit (Bio-Rad) was used with 200 ng of RNA as input for complementary DNA (cDNA) synthesis. Quantitative PCR with reverse

transcription (RT-qPCR) analysis using Power SYBR Green Master Mix (Thermo Fisher Scientific) was performed in technical triplicate using a QuantStudio 5 or 6 Flex (Applied Biosystems). Each cDNA reaction was generated from an individual biological replicate. A list of RT-qPCR primer sequences is provided in **Table 5**.

Table 5: Chapter 3 qRT-PCR primer sequences

Actin, forward	GCTCTTTTCCAGCCTTCCTT
Actin, reverse	CTTCTGCATCCTGTCAGCAA
Nanog, forward	AAGATGCGGACTGTGTTCTC
Nanog, reverse	CGCTTGCACTTCATCCTTTG
Esrrb, forward	AACAGCCCCTACCTGAACCT
Esrrb, reverse	TGCCAA TTCACAGAGAGTGG
Pax6, forward	AGTGAATGGGCGGAGTTATG
Pax6, reverse	ACTTGGACGGGAACTGACAC
Brachyury (T), forward	GAGACGGCTGTGGTCCAGTT
Brachyury (T), reverse	GGGTGGACGAATTCCAGGAT
Sox17, forward	GAATCCAACCAGCCCACTGA
Sox17, reverse	GAGGTTCACTCCGCAGTCGT
Slc16a1, forward	CGTCCAGTAATGATCGCTGGTG
Slc16a1, reverse	GAAAGCAAGCCCAAGACCTCC
Slc16a3, forward	CGGACAGAGGCAGATACAGCG
Slc16a3, reverse	CAGGAGGGCTGCTTTCACCAAG

Co-essentiality analysis

To obtain metabolic gene essentiality scores, we analyzed gene dependency values from the DepMap Portal Project[93,94] 22Q2 release. *Slc16a1* was chosen as bait to identify genes involved in pyruvate uptake. Pearson correlation coefficients were calculated between *Slc16a1* and all genes surveyed, and the top 20 were chosen as input for network analysis and are shown in **Table 6**. Network diagrams were drawn using the Python package NetworkX

(http://networkx.org). Genes with low correlation scores ($r < 0.2$) were filtered out. The Python package PyGraphviz (http://pygraphviz.github.io) with method 'neato' was used to generate spring model layouts. Graphs were created using the NetworkX draw function such that graph edges are weighted according to the strength of pairwise gene correlations.

Table 6: Top *Slc16a1* co-essentiality scores

Gene	Correlation (*r*)
SDHB	0.2650
MRPS33	0.2648
COX14	0.2514
DARS2	0.2454
SDHA	0.2451
MRPL47	0.2445
CYB561A3	0.2415
TCF3	0.2406
COX16	0.2297
DAP3	0.2256
TFB1M	0.2248
BSG	0.2199
COX6B1	0.2186
AGPAT1	0.2168
EZH2	0.2156
COA6	0.2139
MRPL3	0.2125
CDIN1	0.2098
PDCD10	0.2092
CCM2	0.2054

Gene set enrichment analysis

Slc16a1 co-essentiality data was obtained as described above from the DepMap 22Q2 release. Genes were ranked by correlation with *Slc16a1* and this list was used as input for gene

set enrichment analysis[99]of KEGG gene sets. Analysis was performed and graphed using clusterProfiler v4.0[130].

RNA-seq analysis

RNA was isolated as previously described and quantified using a Qubit 3.0 fluorometer. RNA-seq libraries were generated using the TruSeq Stranded mRNA Library Prep Kit (20020594, Illumina) according to the manufacturer's instructions prior to pooling and sequencing by the Memorial Sloan Kettering Cancer Center Integrated Genomics Operation. For analysis, RNA-seq libraries were filtered and trimmed using fastp[106] and mapped with STAR aligner[107] against the mm10 mouse genome assembly using default parameters. Gene counts were assessed using featureCounts[108] and input into DeSeq2 (ref[109]) for quality control analysis, size normalization and variance dispersion corrections.

Statistics and reproducibility

All statistical analysis with the exception of co-essentiality analysis and gene set enrichment analysis was performed using Prism 10 (GraphPad). Error bars, *P* values and statistical tests are reported in the figures and figure legends. No statistical methods were used to predetermine sample sizes. Co-essentiality analysis was performed using Python v3.8 and is available on GitHub (http://github.com/finley-lab/coessentiality-network). Gene set enrichment analysis was performed using R v4.2.1.

3.5 Acknowledgements

Nanog-GFP cells were a gift from R. Jaensich. Work contained in this chapter was performed with assistance from multiple members of the Finley laboratory. Nutrient uptake protocols were developed and optimized by Pavlina K. Todorova. MCT1-OE lines were generated by Angela M. Montero with supervision by the author of this thesis. Sangita Chakraborty assisted with many experiments with supervision by the author of this thesis. Katrina I. Paras performed RNA-seq. Julia S. Brunner assisted with figure preparation. Lydia W.S. Finley supervised the project.

3.6 Figures

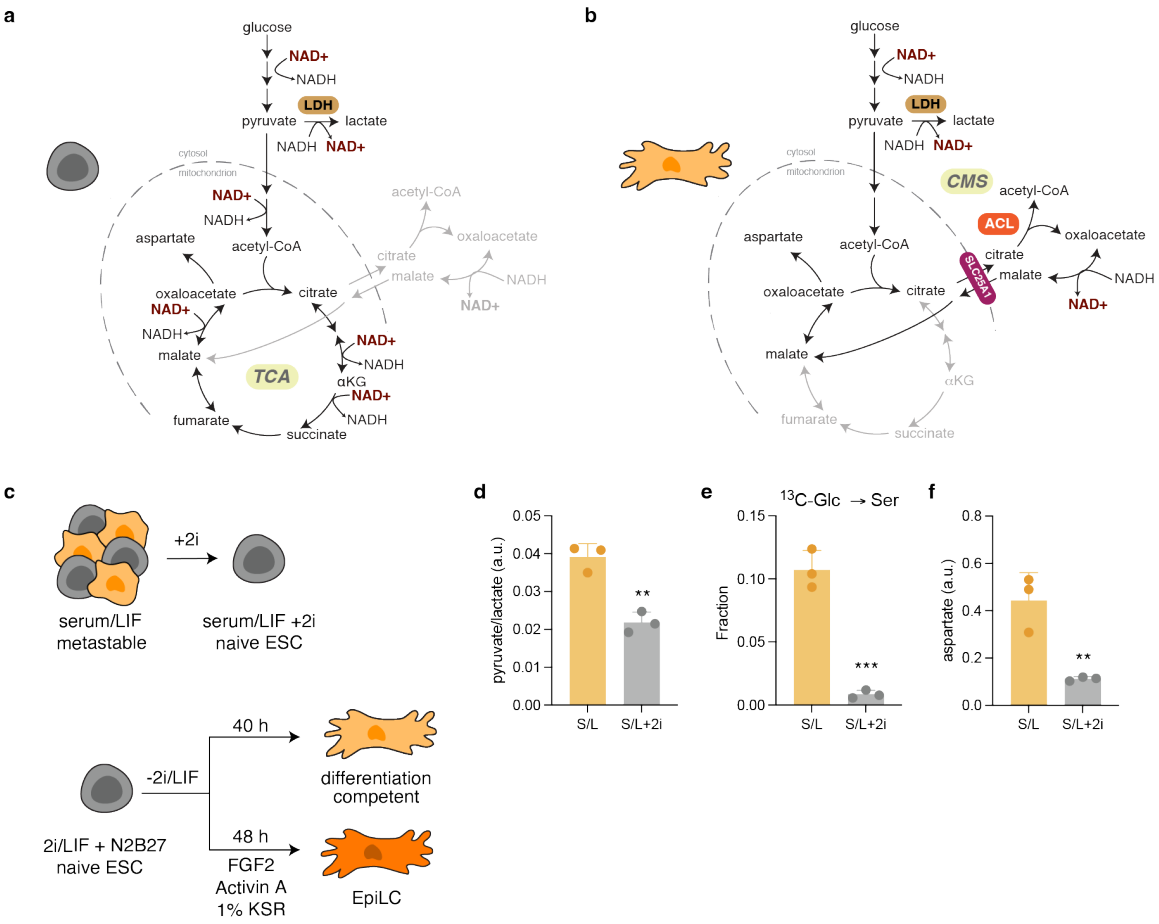

Figure 3.1 Differential TCA cycle configurations underlie ESC pluripotency. a,b, Schematic of the mitochondrial TCA cycle (**a**) and citrate-malate shuttle (**b**). **c,** Experimental setup for ESC fate transitions. **d-f,** Pyruvate/lactate ratio (**d**), fractional enrichment of serine from [U-^{13}C]glucose (**e**), and aspartate levels (**f**) in S/L or S/L+2i-cultured ESCs. Data are mean +/- s.d. *n* = 3 independent replicates. Significance was assessed in comparison to S/L using unpaired two-tailed Student's *t*-test. (**p<0.01, ***p<0.001)

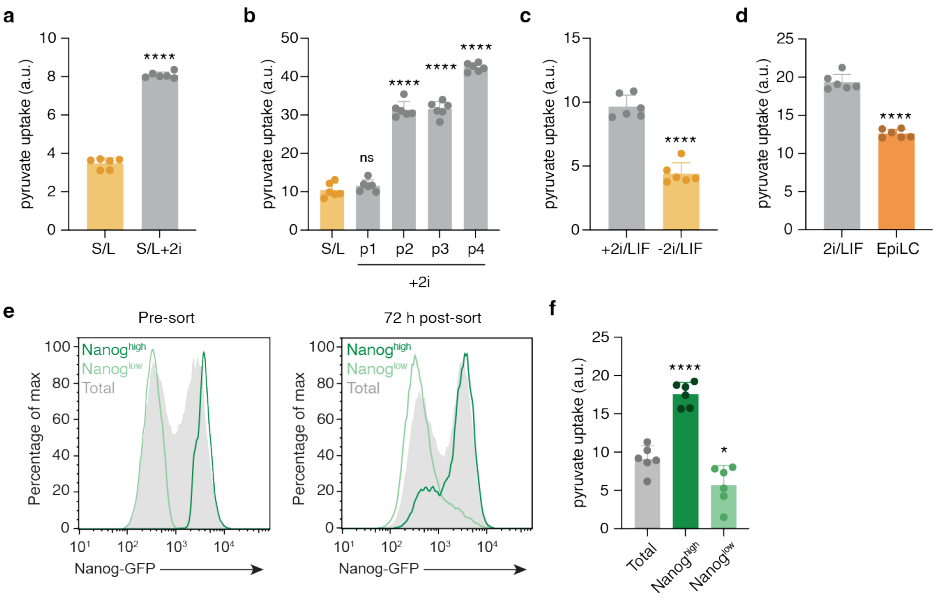

Figure 3.2 Pyruvate uptake is a feature of naive ESCs. a, Pyruvate uptake measured over 24 hours in S/L or S/L+2i-cultured ESCs. **b,** Uptake of pyruvate during conversion to the naive, ground state of pluripotency upon addition of inhibitors against MEK and GSK3β. **c,d,** Uptake of pyruvate by 2i/LIF-cultured ESCs versus ESCs exiting naive pluripotency (**c**) or upon EpiLC induction (**d**). Pyruvate uptake was measured over the final 24 hours of indicated cell state transitions. **e,** Separation of Nanog^{high} and Nanog^{low} populations by FACS. Total populations of Nanog-GFP ESCs cultured in S/L are shown in gray. The top 10% bottom 10% populations were sorted and plated for nutrient uptake measurement (left). Nanog-GFP distribution at the time of media harvest 72 h after initial sorting is shown on the right. **f,** Quantification of pyruvate uptake in Nanog^{high}, Nanog^{low}, and total Nanog-GFP populations shown in **e** (right). Data are mean +/- s.d., $n = 6$ independent replicates. In **a,** and **c-d,** significance was assessed in comparison to S/L (**a**) or 2i/LIF (**c-d**) using unpaired two-tailed Student's *t*-test. For **b** and **f**, significance was assessed relative to S/L (**b**) or total Nanog-GFP population (**f**) using one-way ANOVA with Sidak's multiple comparisons post-test. (*p<0.05, ****p<0.0001)

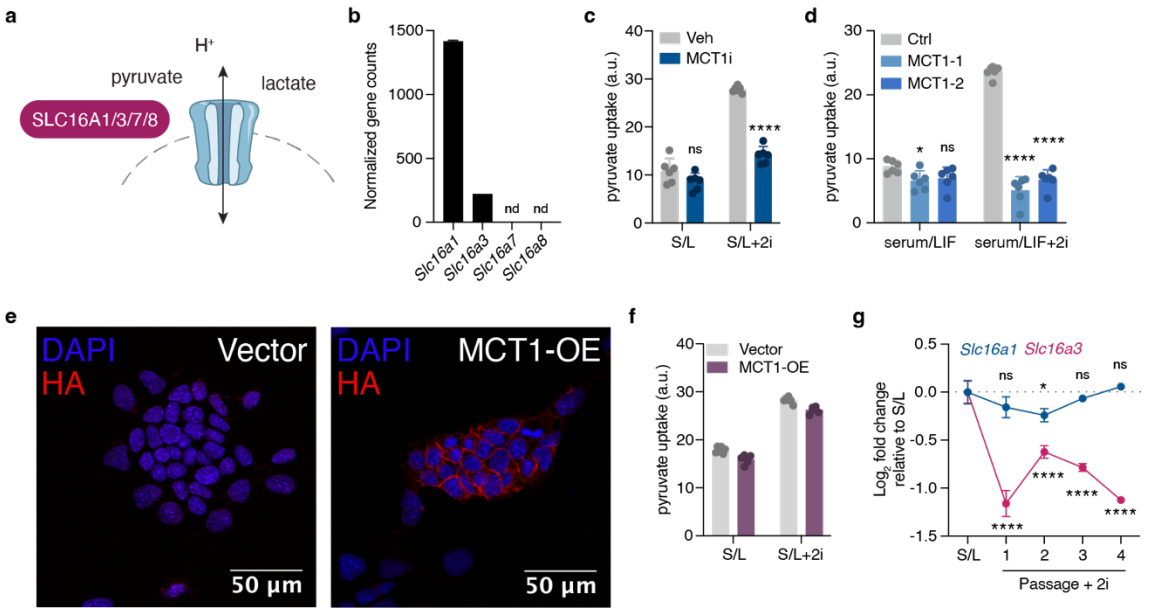

Figure 3.3 MCT1 is required for pyruvate uptake by naive ESCs. a, Schematic depicting monocarboxylate transport by the Slc16 family of transporters. **b,** Expression of monocarboxylate transporters in S/L+2i-cultured ESCs. *Slc16a7* and *Slc16a8* were not detected. **c,d,** Pyruvate uptake in S/L or S/L+2i-cultured ESCs with either MCT1 inhibition (**c**) or in MCT1-deficient ESCs (**d**). For **c**, MCT1i (AZD3965, Selleck Chemicals, 100 nM) or vehicle control was added only during 24 hr of nutrient uptake measurement. **e,** Representative images of immunofluorescence of S/L-cultured ESCs expressing HA-tagged MCT1 (red) or vector control. DAPI staining is shown in blue. **f,** Pyruvate uptake of cells shown in panel **e** cultured in either S/L or S/L+2i. **g,** RT-qPCR of *Slc16a1* or *Slc16a3* at indicated passages upon conversion to the naive, ground state of pluripotency via addition of MEK and GSK3β. Data are mean +/- s.d., $n = 2$, (**b**) 6 (**c,d,f**) or 3 (**g**) independent replicates. Significance was assessed for **c-d** by two-way ANOVA with Sidak's multiple comparisons post-test relative to S/L control or vehicle-treated cells. For **g,** significance was assessed by one-way ANOVA with Sidak's multiple comparisons post-test relative to S/L. (*p<0.05, ****p<0.0001)

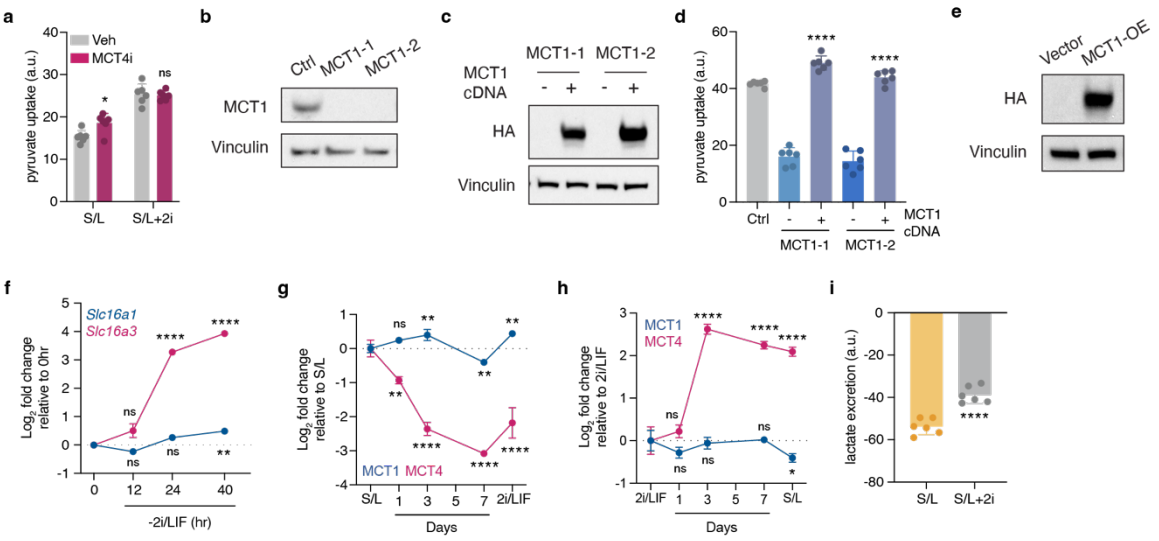

Figure 3.4 MCT1 levels are not limiting for pyruvate uptake. a, Pyruvate uptake in S/L or S/L+2i-cultured ESCs with MCT4 inhibition (VB124, MedChem Express, 10 μM) added during 24h of nutrient uptake measurement. **b,** Immunoblot of clonal mouse ESCs in which CRISPR/Cas9-mediated editing was used to target either a non-genic region of chromosome 8 (Ctrl) or *Slc16a1* (MCT1-1 and MCT1-2). **c,** Immunoblot of mouse ESCs deficient for MCT1 with addition of either HA-tagged MCT1 cDNA or vector control. **d,** Pyruvate uptake in S/L+2i-cultured ESCs shown in panel **c. e,** Immunoblot of ESCs expressing either HA-tagged MCT1 cDNA or vector control. **f**, RNA-seq analysis of *Slc16a1* and *Slc16a3* expression upon 2i/LIF withdrawal for indicated time period. **g,h,** Proteomic analysis of MCT1 and MCT4 levels during acquisition of naive pluripotency (**g**) or exit from the naive ground state (**h**). Data were taken from Atlasi et al. [129] **i,** Lactate excretion over 24 hours by either S/L or S/L+2i-cultured ESCs. Data are mean +/- s.d., $n = 6$, (**a,d,i**) 2, (**f**) or 3 (**g,h**) independent replicates. For **a**, significance was assessed by two-way ANOVA with Sidak's multiple comparisons post-test relative to vehicle-treated cells. Significance was assessed for **d** and **i** using unpaired two-tailed Student's *t*-test relative to each respective MCT1-deficient cell line (**d**) or S/L (**i**). For **f-h,** significance was assessed by one-way ANOVA with Sidak's multiple comparisons post-test relative to 0 h (**f**), S/L (**g**) or 2i/LIF (**h**). (*p<0.05, **p<0.01, ****p<0.0001)

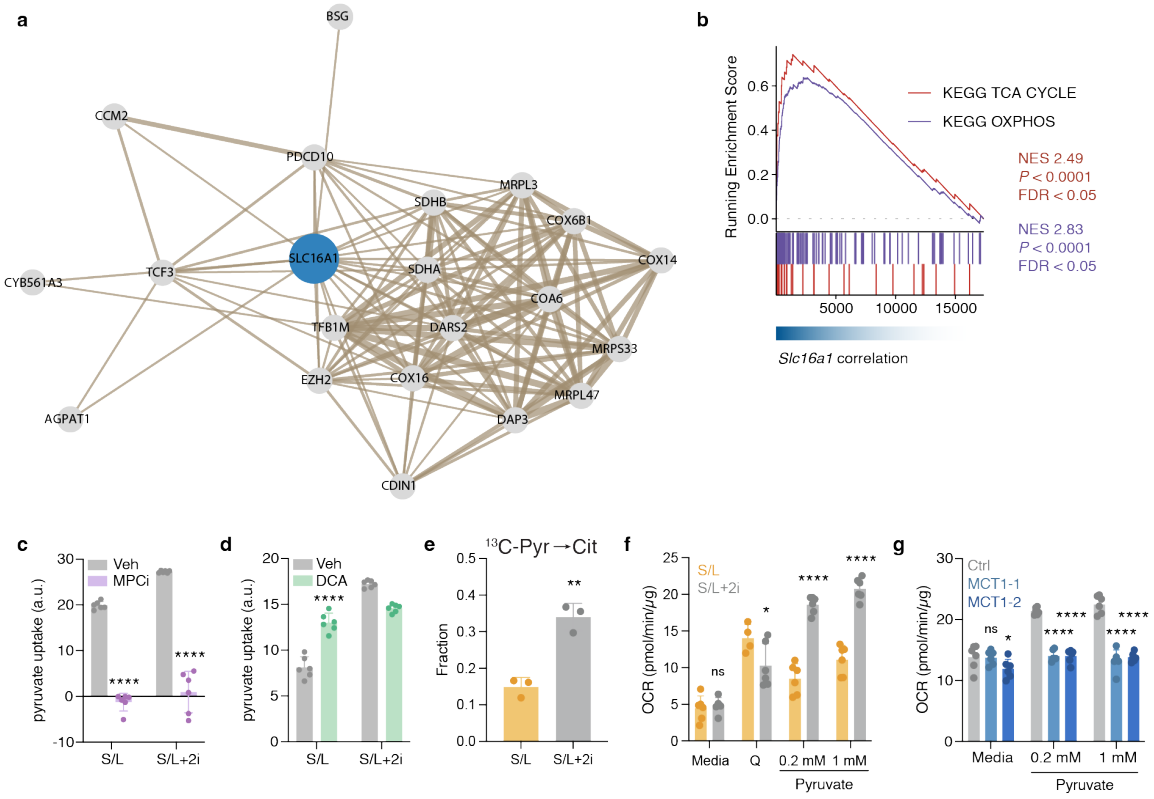

Figure 3.5 Mitochondrial capture of pyruvate dictates its uptake. a, Two-dimensional network diagram representing gene essentiality score correlations between genes. Top 20 genes co-essential with *Slc16a1* are shown. Correlation strength is represented by the length and thickness of the connecting edge. **b,** Gene set enrichment analysis showing that genes correlated with *Slc16a1* essentiality are enriched for KEGG TCA-cycle and oxidative phosphorylation-associated genes. **c,d** Pyruvate uptake in S/L and S/L+2i with either mitochondrial pyruvate carrier inhibition (**c,** UK5099, Tocris, 10μM) or dichloroacetate (**d,** 5 mM) during the 24h of nutrient uptake measurement. **e,** Fractional enrichment of citrate from [U-^{13}C]pyruvate. **f,g,** Oxygen consumption rate of S/L versus S/L+2i (**f**) or SL+2i control versus MCT1-deficient ESCs (**g**) with the addition of indicated substrates. Values shown are the first measurement following FCCP injection. Data are mean +/- s.d., $n = 6$ independent replicates except for **e** ($n = 3$). Significance was assessed by two-way ANOVA with Sidak's multiple comparisons post-test relative to vehicle-treated cells (**c,d**), S/L (**f**), or control ESCs (**g**). For **e,** significance was assessed by unpaired two-tailed Student's *t*-test relative to S/L. (*p<0.05, **p<0.01, ****p<0.0001)

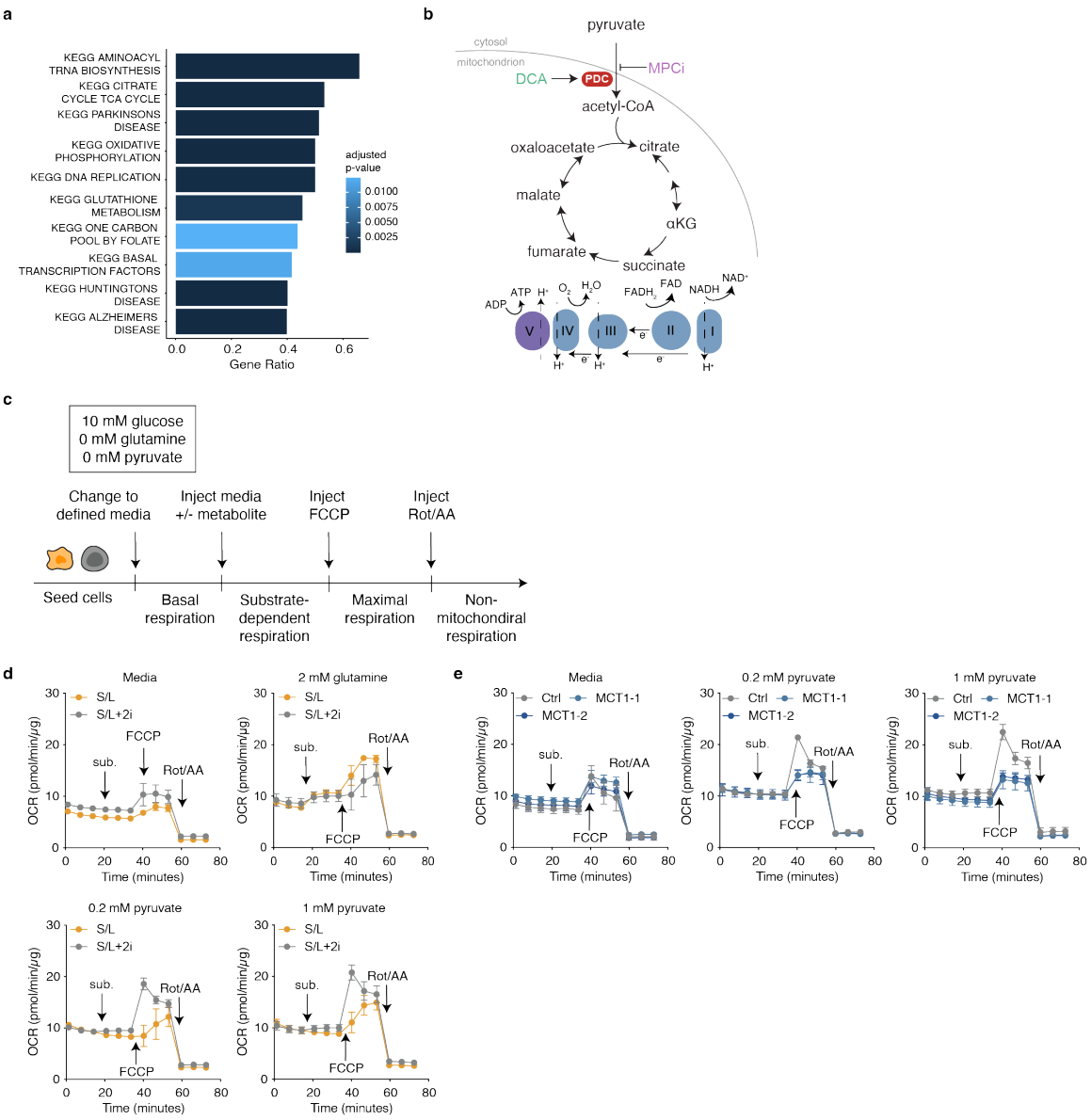

Figure 3.6 Pyruvate is preferentially oxidized by naive ESCs. a, Unbiased gene set enrichment analysis of genes correlated with *Slc16a1* essentiality with KEGG gene sets. Top 10 most enriched gene sets are shown. **b,** Schematic of mitochondrial pyruvate capture for TCA cycle oxidation. **c,** Schematic of oxygen consumption rate measurements with different mitochondrial substrates. **d, e,** Representative oxygen consumption rate profiles for experiments like those shown in **Figure 3.5f, g**.

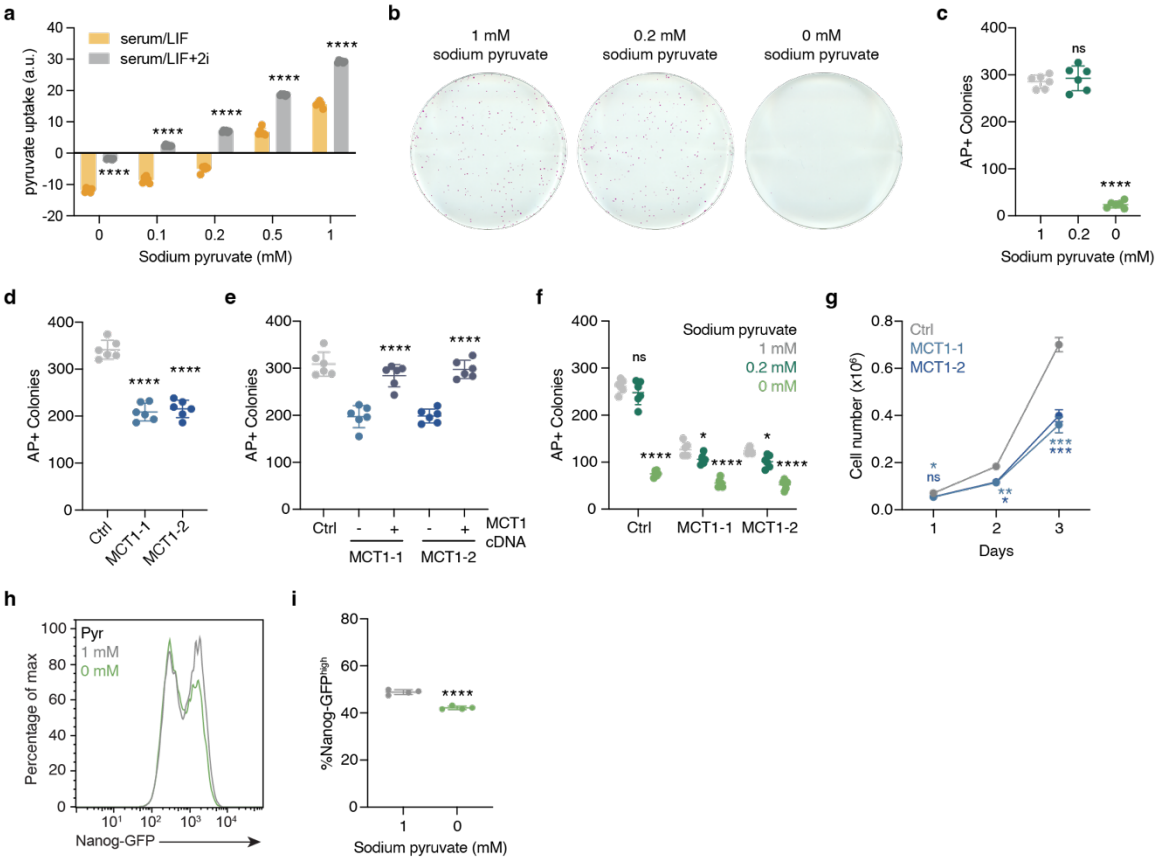

Figure 3.7 Loss of pyruvate uptake impairs naive ESC fitness. a, Pyruvate uptake in S/L and S/L+2i at indicated concentrations of pyruvate over 24 hours. **b,c,** Alkaline phosphatase staining of colony formation assay. S/L+2i-cultured ESCs were seeded at clonal density into medium containing indicated pyruvate concentrations. Representative wells are shown in **b** and quantified in **c. d-f,** Quantification of colony formation assay with S/L+2i control versus MCT1-deficient ESCs (**d,f**) or MCT1-deficient versus MCT1-cDNA expressing ESCs (**e**). Pyruvate was supplemented at 1 mM (**d,e**) or indicagted concentration (**f**). **g,** Growth of control or MCT1-deficient ESCs cultured in S/L+2i media containing 0.2 mM pyruvate. **h,i,** Nanog-GFP distribution of ESCs cultured in S/L media containing 1 or 0 mM pyruvate. Percentage of Nanog^{high} cells is quantified in **i.** Data are mean +/- s.d., n = 6, (**a,c-f**) 3, (**g**) or 4 (**i**) independent replicates. For **a,f-g**, significance was assessed by two-way ANOVA with Sidak's multiple comparisons post-test relative to S/L (**a**), 1mM pyruvate (**f**), or control (**g**). Significance was assessed in **c-d** using one-way ANOVA with Sidak's multiple comparisons post-test relative to 1 mM pyruvate (**c**) or control (**d**). For **e** and **i,** significance was assessed using unpaired two-tailed Student's *t*-test relative to each respective MCT1-deficient cell line (**e**) or 1 mM pyruvate (**i**). (*p<0.05, **p<0.01, ***p<0.001, ****p<0.0001)

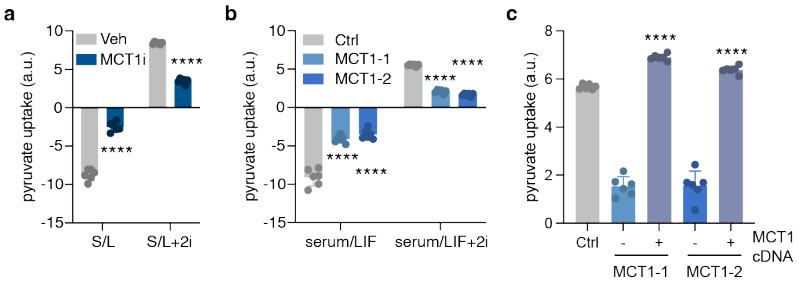

Figure 3.8 MCT1 is required for pyruvate uptake at physiologic pyruvate levels. a-b, Pyruvate uptake in S/L and S/L+2i media containing 0.2 mM pyruvate with inhibition of MCT1 (**a,** AZD3965, 100 nM) or in ESCs lacking MCT1 (**b**). Pyruvate uptake was restored by expression of MCT1 cDNA (**c**). Data are mean +/- s.d., $n = 6$. Significance was assessed for **a,b** by two-way ANOVA with Sidak's multiple comparisons post-test relative to vehicle (**a**) or control cells (**b**). For **c**, significance was assessed using unpaired two-tailed Student's *t*-test relative to each respective MCT1-deficient cell line. (****$p<0.0001$)

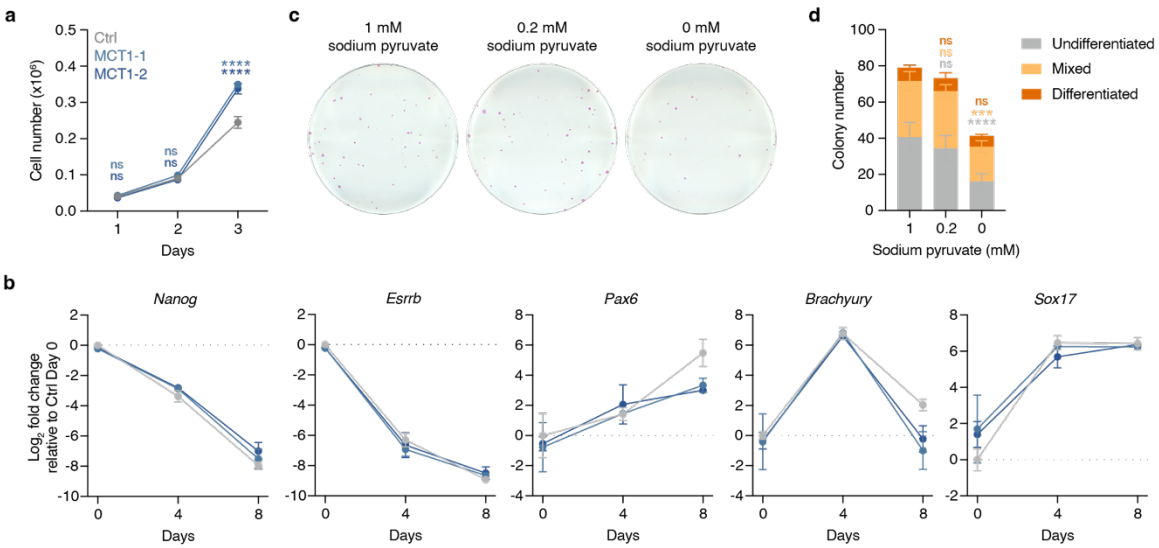

Figure 3.9 MCT1 is dispensable for ESC differentiation. a, Growth of control or MCT1-deficient ESCs cultured in S/L media containing 0.2 mM pyruvate. **b,** RT-qPCR of pluripotency genes and lineage markers during embryoid body formation using control or MCT-deficient ESCs. **c,d**, Alkaline phosphatase staining of colony formation assay performed in S/L media with indicated concentrations of pyruvate. Representative wells are shown in **c** and were scored for quantification in **d.** Data are mean +/- s.d., $n = 3$ (**a,b**) or 6 (**d**). Significance was assessed by two-way ANOVA with Sidak's multiple comparisons post-test relative to control cells (c) or 1 mM pyruvate (**d**). (***p<0.001, ****p<0.0001)

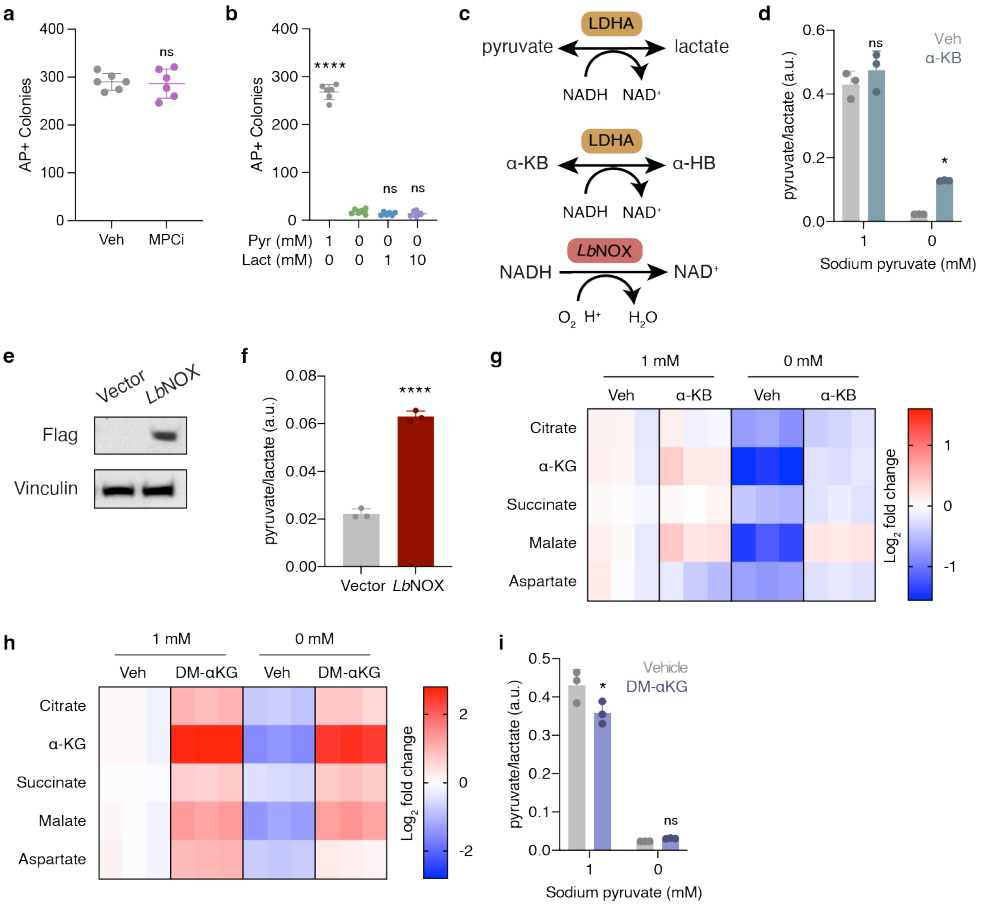

Figure 3.10 Alternative electron acceptors support TCA cycle metabolism in naive ESCs. **a**, Quantification of colony formation assay of ESCs cultured in media containing 2i and 1 mM sodium pyruvate with MPCi (UK5099, 10μM) or vehicle control. MPCi was added 48 h prior to seeding and was maintained for the duration of the assay. **b,** Quantification of colony formation of S/L+2i cultured ESCs in media containing indicated amounts of pyruvate or lactate. **c,** Schematic showing methods of NAD^+ regeneration by electron acceptors or *Lb*NOX. **d,** Pyruvate/lactate ratio in S/L+2i media containing either 1 or 0 mM pyruvate and with α-KB (1 mM) or vehicle supplementation. **e,f,** Immunoblot (**e**) showing Flag-tagged *Lb*NOX expression in S/L+2i-cultured ESCs and the pyruvate/lactate ratio (**f**) in these cells. **g,h,** Steady-state levels of TCA-cycle metabolites in S/L+2i-cultured ESCs with or without pyruvate and α-KB (1mM, **g**) or DM-αKG (1mM, **h**) supplementation. **i,** Pyruvate/lactate ratio S/L+2i-cultured ESCs with 1 or 0 mM pyruvate and vehicle or DM-αKG (1 mM) supplementation. Data are mean +/- s.d., $n = 6$ (**a,b**) or 3 (**d,f-i**). For **a,f,** significance was assessed by unpaired two-tailed Student's *t*-test relative to each vehicle (**a**) or vector (**f**) control. Significance was assessed for **b** using one-way ANOVA with Sidak's multiple comparisons post-test relative to 0 mM pyruvate and lactate and for **c,i,** by two-way ANOVA with Sidak's multiple comparisons post-test relative to vehicle controls. (*p<0.05, ****p<0.0001)

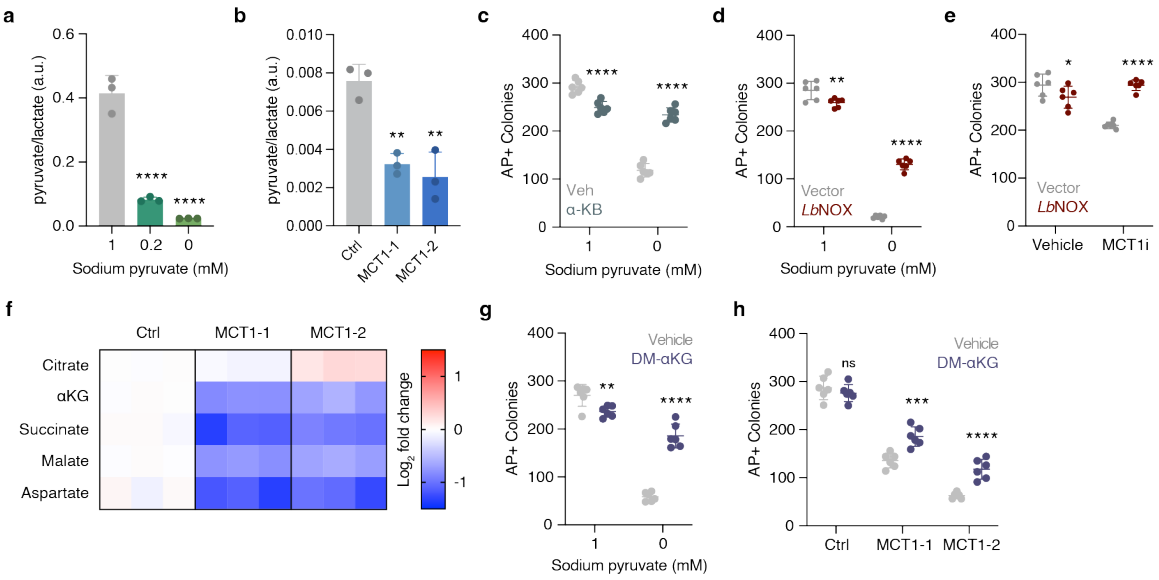

Figure 3.11 Alternative electron acceptors rescue loss of pyruvate uptake in naive ESCs. **a,b,** Pyruvate/lactate ratio in S/L+2i-cultured ESCs in media containing indicated pyruvate concentration (**a**) or in ESCs lacking MCT1 (**b**). **c-e,** Quantification of colony formation assay of ESCs in S/L+2i media containing 1 or 0 mM pyruvate with α-KB of vehicle supplementation (**c**), in ESCs expressing *Lb*NOX or vector control (**d**), or in *Lb*NOX-expressing ESCs cultured in media containing 1 mM pyruvate with or without MCT1i (**e,** AZD3965, 100nM). For **e,** MCT1i was added 48 h prior to seeding and was maintained for the duration of the assay. f, Steady-state levels of TCA-cycle metabolites in control or MCT1-deficient ESCs in S/L+2i media with 0.2 mM pyruvate. **g,h,** Quantification of colony formation assay of S/L+2i-cultured ESCs with 1 or 0 mM pyruvate (**g**) or control versus MCT1-deficient ESCs in 1 mM pyruvate (**h**) with vehicle or DM-αKG supplementation (1mM). Data are mean +/- s.d., $n = 3$ (**a-b,f**) or 6 (**c-e,g-h**). Significance was assessed for **a,b** using one-way ANOVA with Sidak's multiple comparisons post-test relative to 1 mM pyruvate (**a**) or control cells (**b**). For all other panels, significance was assessed by two-way ANOVA with Sidak's multiple comparisons post-test relative to vehicle (**c, g,h**) or vector controls (**d,e**). (*p<0.05, **p<0.01, ***p<0.001, ****p<0.0001)

CHAPTER 4: CONCLUSIONS AND FUTURE DIRECTIONS

Development is a period of specialized metabolism where metabolic pathways are rewired to meet specific proliferative demands and maintain cell identity. In this thesis, we sought to interrogate this metabolic rewiring to determine how metabolism supports the acquisition or loss of naive pluripotency. These studies uncovered common themes, where ESCs differentially engage electron shuttles such as the citrate-malate shuttle (**Chapter 2**) or alter pyruvate uptake (**Chapter 3**), and perturbation of these pathways created cell-state dependent metabolic vulnerabilities. Interestingly, a common utility of both the CMS and pyruvate uptake is the regeneration of cytosolic NAD^+. Therefore, this collective work illustrates the diverse ways cells meet common metabolic demands during development and opens exciting new avenues of inquiry.

4.1 TCA cycle rewiring in development

Upon the exit from naive pluripotency, ESCs decrease usage of the mitochondrial TCA cycle and engage the CMS (**Chapter 2**). Correspondingly, deletion of the genes encoding components of the CMS block exit from naive pluripotency as ESCs are unable to meet the bioenergetic demands of differentiation and die. Supporting the importance of this pathway in development, homozygous loss of the CMS enzyme ACL is embryonic lethal before E8.5[131]. Similarly, mutations in the citrate-malate antiporter SLC25A1 in humans results in a combined D-2- and L-2-hydroxyglutaric aciduria that causes developmental delay and early death[132].

Many questions remain regarding the role of the CMS in development, and studies addressing them are already underway. Which metabolic outputs of the CMS are specifically required for exit from naive pluripotency? What metabolic or signaling cues regulate engagement of the CMS? Is the CMS required in specific lineages of the developing embryo or in adult stem

cells? The development of new tools such as degron-based approaches to temporally degrade CMS components will help yield insights into these and other questions.

Another key future direction will be the engagement of the CMS in intact embryos and in vivo. Recent studies have generated ^{13}C-glucose labeling datasets in the 2C, morula, and blastocyst stages of preimplantation embryos cultured ex vivo[133]. To profile the metabolism in vivo, several groups have developed approaches to perform isotope tracing in the placenta and embryo during midgestation[58] and mid-to-late gestation[59] in mice. These datasets will be instructive for examining engagement of the CMS in different tissue types throughout the spectrum of embryogenesis.

4.2 Pyruvate uptake in the developing blastocyst

Work in **Chapter 3** of this thesis demonstrates that pyruvate is avidly consumed by ESCs cultured in the naive ground state of pluripotency that resembles the ICM of the pre-implantation embryo. Strikingly, pyruvate has been among the most studied metabolites in embryonic development[66]. Pyruvate is robustly consumed in developmental stages up to the blastocyst, at which time glucose becomes the dominant substrate[134]. Furthermore, pyruvate supplementation in media is required—and is sufficient in the absence of other substrates—for development from the 1-cell to blastocyst stage[135]. The requirement for pyruvate can be partially rescued by NAD^+, suggesting that at least part of the role of pyruvate is regulation of cellular redox[136]. Interestingly, lactate can support development from the 2-cell to blastocyst stage through mechanism dependent on the malate-aspartate shuttle[137] and can directly regulate pyruvate uptake metabolism[138]. The roles of pyruvate and lactate have been confirmed using modern metabolomic and tracing approaches[133] that additionally suggest pyruvate might act by promoting the nuclear localization of TCA cycle enzymes[139]. In these models, DM-αKG rescues the effects of pyruvate withdrawal, although these findings have been disputed[140]. Nevertheless, these studies collectively suggest

that the work discussed in **Chapter 3** of this thesis may have real relevance to embryonic development.

The mechanisms by which pyruvate is taken up in development are unknown. Notably, homozygous loss of MCT1 in mouse models is embryonic lethal[141,142], although the exact stage of death of MCT1-deficient embryos is unexplored. Mice with heterozygous loss of MCT1 develop an axonopathy in the brain and spinal cord by 8 months of age due to loss of MCT1 expression in oligodendroglia. Intriguingly, several human patients with mutations in MCT1 have been identified. These patients can present with defects in lactic acid transport[143]or disorders of ketone utilization leading to ketoacidosis often accompanied by mild-to-moderate developmental delay[144]. MCT1 inhibition has also been investigated for as a target for immunosuppression[145] and for several types of cancer[146]. Critically, the consequences of MCT1 loss-of-function or inhibition have been largely attributed to transport of monocarboxylates other than pyruvate, particularly lactate efflux. This study (**Chapter 3**) perhaps cautions against targeting of MCT1 for disease treatment as pyruvate uptake may play important roles in stem cell populations or in cell types dependent on pyruvate uptake for NAD+ regeneration. Of note, deficiency of almost all enzymes involved in pyruvate metabolism have been implicated in human disease[147], emphasizing the critical importance of this pathway to normal organismal homeostasis.

4.3 Metabolism and human disease

The above examples suggest that perhaps the strongest argument for the utility of studying metabolism comes from the presentation of patients with inborn errors of metabolism. These diseases are characterized by mutations in metabolic enzymes that often result in almost complete loss of protein function. However, despite the loss of what many would consider essential cellular pathways, many inborn errors of metabolism are compatible with embryonic development and postnatal life[148]. Patients with these disorders can have clinical manifestations

of their disease at all ages, and inborn errors of metabolism have been shown to affect virtually every organ system. For example, Leigh syndrome—a disorder caused largely by alterations in the mitochondrial respiratory chain—is characterized clinically by a wide range of abnormalities ranging from CNS disease to non-neurological manifestations to complete absence of symptoms that can present in both pediatric and adult populations[149].

The diversity of presentation of inborn errors of metabolism demonstrates the flexibility of variable cell types to circumvent loss of metabolic pathway function throughout different periods of human development. Loss of metabolic gene function disproportionately affects tissues that rely on that pathway the most but can be tolerated in other organ systems. Furthermore, therapies designed to treat these metabolic diseases are often metabolic in nature themselves, such as dietary modification to reduce exposure to nutrients whose buildup is pathological[150]. That these interventions improve patient health and lifespan reinforces the modularity of metabolic disease, where metabolic activity can be titrated to both beneficial and harmful levels.

Inborn errors of metabolism and their treatment are a valuable tool to understand the way that metabolism functions in normal human physiology. Similarly, learning more about the way that metabolic pathways are assembled across diverse tissue types and how these pathways change with development and aging will inform the understanding and development of therapies for these unique diseases.

REFERENCES

1. Mathieu, J. & Ruohola-Baker, H. Metabolic remodeling during the loss and acquisition of pluripotency. *Development* **144,** 541–551 (2017).
2. Martello, G. & Smith, A. The nature of embryonic stem cells. *Annu. Rev. Cell Dev. Biol.* **30,** 647–675 (2014).
3. Boroviak, T., Loos, R., Bertone, P., Smith, A. & Nichols, J. The ability of inner-cell-mass cells to self-renew as embryonic stem cells is acquired following epiblast specification. *Nat. Cell Biol.* **16,** 516–528 (2014).
4. Ying, Q.-L. *et al.* The ground state of embryonic stem cell self-renewal. **453,** 519–523 (2008).
5. Kalkan, T. *et al.* Tracking the embryonic stem cell transition from ground state pluripotency. *Development* **144,** 1221–1234 (2017).
6. Hayashi, K., Ohta, H., Kurimoto, K., Aramaki, S. & Saitou, M. Reconstitution of the mouse germ cell specification pathway in culture by pluripotent stem cells. *Cell* **146,** 519–532 (2011).
7. Brons, I. G. M. *et al.* Derivation of pluripotent epiblast stem cells from mammalian embryos. *Nature* **448,** 191–195 (2007).
8. Tesar, P. J. *et al.* New cell lines from mouse epiblast share defining features with human embryonic stem cells. *Nature* **448,** 196–199 (2007).
9. Weinberger, L., Ayyash, M., Novershtern, N. & Hanna, J. H. Dynamic stem cell states: naive to primed pluripotency in rodents and humans. *Nat Rev Mol Cell Biol* **17,** 155–169 (2016).
10. Intlekofer, A. M. & Finley, L. W. S. Metabolic signatures of cancer cells and stem cells. *Nat Metab* **1,** 177–188 (2019).
11. Zhou, W. *et al.* HIF1α induced switch from bivalent to exclusively glycolytic metabolism during ESC-to-EpiSC/hESC transition. *EMBO J.* **31,** 2103–2116 (2012).
12. Gu, W. *et al.* Glycolytic Metabolism Plays a Functional Role in Regulating Human Pluripotent Stem Cell State. *Cell Stem Cell* **19,** 476–490 (2016).
13. Cliff, T. S. *et al.* MYC Controls Human Pluripotent Stem Cell Fate Decisions through Regulation of Metabolic Flux. *Cell Stem Cell* **21,** 502–516.e9 (2017).
14. DeBerardinis, R. J. & Chandel, N. S. We need to talk about the Warburg effect. *Nat Metab* **2,** 127–129 (2020).
15. Zhang, J. *et al.* UCP2 regulates energy metabolism and differentiation potential of human pluripotent stem cells. *EMBO J.* **35,** 899–899 (2016).
16. Kim, H. *et al.* Core Pluripotency Factors Directly Regulate Metabolism in Embryonic Stem Cell to Maintain Pluripotency. *Stem Cells* **33,** 2699–2711 (2015).
17. Pernaute, B. *et al.* DRP1 levels determine the apoptotic threshold during embryonic differentiation through a mitophagy-dependent mechanism. *Developmental Cell* **57,** 1316–1330.e7 (2022).
18. Carey, B. W., Finley, L. W. S., Cross, J. R., Allis, C. D. & Thompson, C. B. Intracellular α-ketoglutarate maintains the pluripotency of embryonic stem cells. **518,** 413–416 (2015).
19. Vardhana, S. A. *et al.* Glutamine independence is a selectable feature of pluripotent stem cells. *Nat Metab* **1,** 676–687 (2019).
20. Bayerl, J. *et al.* Principles of signaling pathway modulation for enhancing human naive pluripotency induction. *Cell Stem Cell* **28,** 1549–1565.e12 (2021).
21. Lu, V. *et al.* Glutamine-dependent signaling controls pluripotent stem cell fate. *Developmental Cell* **57,** 610–623.e8 (2022).

22. Snow, M. H. Autonomous development of parts isolated from primitive-streak-stage mouse embryos. Is development clonal? *J Embryol Exp Morphol* **65 Suppl,** 269–287 (1981).
23. Manova, K. *et al.* Apoptosis in mouse embryos: elevated levels in pregastrulae and in the distal anterior region of gastrulae of normal and mutant mice. *Dev Dyn* **213,** 293–308 (1998).
24. Heyer, B. S., MacAuley, A., Behrendtsen, O. & Werb, Z. Hypersensitivity to DNA damage leads to increased apoptosis during early mouse development. *Genes & Development* **14,** 2072–2084 (2000).
25. Pernaute, B. *et al.* MicroRNAs control the apoptotic threshold in primed pluripotent stem cells through regulation of BIM. *Genes & Development* **28,** 1873–1878 (2014).
26. Tait, S. W. G. & Green, D. R. Mitochondrial regulation of cell death. *Cold Spring Harb Perspect Biol* **5,** a008706 (2013).
27. Pernaute, B. *et al.* DRP1 levels determine the apoptotic threshold during embryonic differentiation through a mitophagy-dependent mechanism. *Developmental Cell* **57,** 1316–1330.e7 (2022).
28. Chakrabarty, R. P. & Chandel, N. S. Mitochondria as Signaling Organelles Control Mammalian Stem Cell Fate. *Cell Stem Cell* **28,** 394–408 (2021).
29. Tan, D. Q. & Suda, T. Reactive Oxygen Species and Mitochondrial Homeostasis as Regulators of Stem Cell Fate and Function. *Antioxid Redox Signal* **29,** 149–168 (2018).
30. Hämäläinen, R. H. *et al.* mtDNA Mutagenesis Disrupts Pluripotent Stem Cell Function by Altering Redox Signaling. *Cell Reports* **11,** 1614–1624 (2015).
31. Rodríguez-Nuevo, A. *et al.* Oocytes maintain ROS-free mitochondrial metabolism by suppressing complex I. *Nature* **607,** 756–761 (2022).
32. van der Weijden, V. A. & Bulut-Karslioglu, A. Molecular Regulation of Paused Pluripotency in Early Mammalian Embryos and Stem Cells. *Front Cell Dev Biol* **9,** 708318 (2021).
33. Hussein, A. M. *et al.* Metabolic Control over mTOR-Dependent Diapause-like State. *Developmental Cell* **52,** 236–250.e7 (2020).
34. Sousa, M. I., Correia, B., Rodrigues, A. S. & Ramalho-Santos, J. Metabolic characterization of a paused-like pluripotent state. *Biochim Biophys Acta Gen Subj* **1864,** 129612 (2020).
35. Khoa, L. T. P. *et al.* Histone Acetyltransferase MOF Blocks Acquisition of Quiescence in Ground-State ESCs through Activating Fatty Acid Oxidation. *Cell Stem Cell* **27,** 441–458.e10 (2020).
36. Arena, R. *et al.* Lipid droplets in mammalian eggs are utilized during embryonic diapause. *Proc. Natl. Acad. Sci. U.S.A.* **118,** e2018362118 (2021).
37. Lee, J.-E. *et al.* Autophagy regulates embryonic survival during delayed implantation. *Endocrinology* **152,** 2067–2075 (2011).
38. Fenelon, J. C. & Murphy, B. D. Inhibition of polyamine synthesis causes entry of the mouse blastocyst into embryonic diapause. *Biol Reprod* **97,** 119–132 (2017).
39. Naeslund, G. The effect of glucose-, arginine- and leucine-deprivation on mouse blastocyst outgrowth in vitro. *Ups J Med Sci* **84,** 9–20 (1979).
40. Scognamiglio, R. *et al.* Myc Depletion Induces a Pluripotent Dormant State Mimicking Diapause. *Cell* **164,** 668–680 (2016).
41. Bulut-Karslioglu, A. *et al.* Inhibition of mTOR induces a paused pluripotent state. *Nature* **540,** 119–123 (2016).
42. Liu, W. M. *et al.* Let-7 derived from endometrial extracellular vesicles is an important inducer of embryonic diapause in mice. *Sci Adv* **6,** (2020).
43. Schvartzman, J. M., Thompson, C. B. & Finley, L. W. S. Metabolic regulation of chromatin modifications and gene expression. *J Cell Biol* **217,** 2247–2259 (2018).

44. Shyh-Chang, N. *et al.* Influence of threonine metabolism on S-adenosylmethionine and histone methylation. *Science* **339,** 222–226 (2013).
45. Shiraki, N. *et al.* Methionine metabolism regulates maintenance and differentiation of human pluripotent stem cells. *Cell Metab.* **19,** 780–794 (2014).
46. Sperber, H. *et al.* The metabolome regulates the epigenetic landscape during naive-to-primed human embryonic stem cell transition. *Nat. Cell Biol.* **17,** 1523–1535 (2015).
47. Carey, B. W., Finley, L. W. S., Cross, J. R., Allis, C. D. & Thompson, C. B. Intracellular α-ketoglutarate maintains the pluripotency of embryonic stem cells. **518,** 413–416 (2015).
48. Hwang, I.-Y. *et al.* Psat1-Dependent Fluctuations in α-Ketoglutarate Affect the Timing of ESC Differentiation. *Cell Metab.* **24,** 494–501 (2016).
49. Baksh, S. C. & Finley, L. W. S. Metabolic Coordination of Cell Fate by α-Ketoglutarate-Dependent Dioxygenases. *Trends in Cell Biology* (2020). doi:10.1016/j.tcb.2020.09.010
50. Blaschke, K. *et al.* Vitamin C induces Tet-dependent DNA demethylation and a blastocyst-like state in ES cells. **500,** 222–226 (2013).
51. TeSlaa, T. *et al.* α-Ketoglutarate Accelerates the Initial Differentiation of Primed Human Pluripotent Stem Cells. *Cell Metab.* **24,** 485–493 (2016).
52. Li, X. *et al.* Regulation of chromatin and gene expression by metabolic enzymes and metabolites. *Nat Rev Mol Cell Biol* **19,** 563–578 (2018).
53. Wellen, K. E. *et al.* ATP-citrate lyase links cellular metabolism to histone acetylation. *Science* **324,** 1076–1080 (2009).
54. Sabari, B. R., Zhang, D., Allis, C. D. & Zhao, Y. Metabolic regulation of gene expression through histone acylations. *Nat Rev Mol Cell Biol* **18,** 90–101 (2017).
55. Moussaieff, A. *et al.* Glycolysis-mediated changes in acetyl-CoA and histone acetylation control the early differentiation of embryonic stem cells. *Cell Metab.* **21,** 392–402 (2015).
56. Finley, L. W. S. What is cancer metabolism? *Cell* **186,** 1670–1688 (2023).
57. Brunet, A., Goodell, M. A. & Rando, T. A. Ageing and rejuvenation of tissue stem cells and their niches. *Nat Rev Mol Cell Biol* **24,** 45–62 (2023).
58. Solmonson, A. *et al.* Compartmentalized metabolism supports midgestation mammalian development. *Nature* **604,** 349–353 (2022).
59. Perez Ramirez, C. A. *et al.* Atlas of Fetal Metabolism During Mid-To-Late Gestation and Diabetic Pregnancy. *bioRxiv* 1–38 (2023). doi:10.1101/2023.03.16.532852
60. Harris, S. E., Gopichandran, N., Picton, H. M., Leese, H. J. & Orsi, N. M. Nutrient concentrations in murine follicular fluid and the female reproductive tract. *Theriogenology* **64,** 992–1006 (2005).
61. Palm, W. & Thompson, C. B. Nutrient acquisition strategies of mammalian cells. *Nature* **546,** 234–242 (2017).
62. Todorova, P. K. *et al.* Amino acid intake strategies define pluripotent cell states. *bioRxiv* 1–32 (2022). doi:10.1101/2022.11.16.516803
63. Wang, J. *et al.* Dependence of mouse embryonic stem cells on threonine catabolism. *Science* **325,** 435–439 (2009).
64. Whitten, W. K. & Biggers, J. D. Complete development in vitro of the pre-implantation stages of the mouse in a simple chemically defined medium. *J Reprod Fertil* **17,** 399–401 (1968).
65. Cholewa, J. A. & Whitten, W. K. Development of two-cell mouse embryos in the absence of a fixed-nitrogen source. *J Reprod Fertil* **22,** 553–555 (1970).
66. Leese, H. J. Metabolism of the preimplantation embryo: 40 years on. *Reproduction* **143,** 417–427 (2012).
67. DeBerardinis, R. J. & Chandel, N. S. Fundamentals of cancer metabolism. *Sci Adv* **2,** e1600200 (2016).

68. Kim, J. & DeBerardinis, R. J. Mechanisms and Implications of Metabolic Heterogeneity in Cancer. *Cell Metab.* **30,** 434–446 (2019).
69. Muir, A., Danai, L. V. & Vander Heiden, M. G. Microenvironmental regulation of cancer cell metabolism: implications for experimental design and translational studies. *Dis Model Mech* **11,** (2018).
70. Tsherniak, A. *et al.* Defining a Cancer Dependency Map. *Cell* **170,** 564–576.e16 (2017).
71. Wainberg, M. *et al.* A genome-wide atlas of co-essential modules assigns function to uncharacterized genes. *Nat. Genet.* **53,** 638–649 (2021).
72. Hatzivassiliou, G. *et al.* ATP citrate lyase inhibition can suppress tumor cell growth. *Cancer Cell* **8,** 311–321 (2005).
73. Zhao, S. *et al.* ATP-Citrate Lyase Controls a Glucose-to-Acetate Metabolic Switch. *Cell Reports* **17,** 1037–1052 (2016).
74. Chen, P.-H. *et al.* Metabolic Diversity in Human Non-Small Cell Lung Cancer Cells. *Mol. Cell* **76,** 838–851.e5 (2019).
75. Alves, T. C. *et al.* Integrated, Step-Wise, Mass-Isotopomeric Flux Analysis of the TCA Cycle. *Cell Metab.* **22,** 936–947 (2015).
76. Sullivan, L. B. *et al.* Aspartate is an endogenous metabolic limitation for tumour growth. *Nat. Cell Biol.* **20,** 782–788 (2018).
77. Lewis, C. A. *et al.* Tracing compartmentalized NADPH metabolism in the cytosol and mitochondria of mammalian cells. *Mol. Cell* **55,** 253–263 (2014).
78. Williamson, D. H., Lund, P. & Krebs, H. A. The redox state of free nicotinamide-adenine dinucleotide in the cytoplasm and mitochondria of rat liver. *Biochem. J.* **103,** 514–527 (1967).
79. Birsoy, K. *et al.* An Essential Role of the Mitochondrial Electron Transport Chain in Cell Proliferation Is to Enable Aspartate Synthesis. *Cell* **162,** 540–551 (2015).
80. Krebs, H. A. & Eggleston, L. V. The oxidation of pyruvate in pigeon breast muscle. *Biochem. J.* **34,** 442–459 (1940).
81. Shintaku, J. *et al.* MyoD Regulates Skeletal Muscle Oxidative Metabolism Cooperatively with Alternative NF-κB. *Cell Reports* **17,** 514–526 (2016).
82. Stacpoole, P. W. The pharmacology of dichloroacetate. *Metabolism* **38,** 1124–1144 (1989).
83. Vardhana, S. A. *et al.* Glutamine independence is a selectable feature of pluripotent stem cells. *Nat Metab* **1,** 676–687 (2019).
84. Pereira, L., Yi, F. & Merrill, B. J. Repression of Nanog gene transcription by Tcf3 limits embryonic stem cell self-renewal. *Molecular and Cellular Biology* **26,** 7479–7491 (2006).
85. Wray, J. *et al.* Inhibition of glycogen synthase kinase-3 alleviates Tcf3 repression of the pluripotency network and increases embryonic stem cell resistance to differentiation. *Nat. Cell Biol.* **13,** 838–845 (2011).
86. Sullivan, L. B. *et al.* Supporting Aspartate Biosynthesis Is an Essential Function of Respiration in Proliferating Cells. *Cell* **162,** 552–563 (2015).
87. Borst, P. The malate-aspartate shuttle (Borst cycle): How it started and developed into a major metabolic pathway. *IUBMB Life* **72,** 2241–2259 (2020).
88. Assmann, N. *et al.* Srebp-controlled glucose metabolism is essential for NK cell functional responses. *Nat Immunol* **18,** 1197–1206 (2017).
89. Luengo, A. *et al.* Increased demand for NAD+ relative to ATP drives aerobic glycolysis. *Mol. Cell* **81,** 691–707.e6 (2021).
90. Davidson, S. M. *et al.* Environment Impacts the Metabolic Dependencies of Ras-Driven Non-Small Cell Lung Cancer. *Cell Metab.* **23,** 517–528 (2016).

91. Marin-Valencia, I. *et al.* Analysis of tumor metabolism reveals mitochondrial glucose oxidation in genetically diverse human glioblastomas in the mouse brain in vivo. *Cell Metab.* **15,** 827–837 (2012).
92. Zhu, X. G. *et al.* Functional Genomics In Vivo Reveal Metabolic Dependencies of Pancreatic Cancer Cells. *Cell Metab.* **33,** 211–221.e6 (2021).
93. Dempster, J. M. *et al.* Extracting Biological Insights from the Project Achilles Genome-Scale CRISPR Screens in Cancer Cell Lines. *bioRxiv* 720243 (2019). doi:10.1101/720243
94. Meyers, R. M. *et al.* Computational correction of copy number effect improves specificity of CRISPR-Cas9 essentiality screens in cancer cells. *Nat. Genet.* **49,** 1779–1784 (2017).
95. Ashburner, M. *et al.* Gene ontology: tool for the unification of biology. The Gene Ontology Consortium. *Nat. Genet.* **25,** 25–29 (2000).
96. The Gene Ontology Consortium. The Gene Ontology Resource: 20 years and still GOing strong. *Nucleic Acids Res* **47,** D330–D338 (2019).
97. Virtanen, P. *et al.* SciPy 1.0: fundamental algorithms for scientific computing in Python. *Nat. Methods* **17,** 261–272 (2020).
98. Ghandi, M. *et al.* Next-generation characterization of the Cancer Cell Line Encyclopedia. *Nature* **569,** 503–508 (2019).
99. Subramanian, A. *et al.* Gene set enrichment analysis: a knowledge-based approach for interpreting genome-wide expression profiles. *PNAS* **102,** 15545–15550 (2005).
100. Dow, L. E. *et al.* Inducible in vivo genome editing with CRISPR-Cas9. *Nat Biotechnol* **33,** 390–394 (2015).
101. MacDougall, M. S., Clarke, R. & Merrill, B. J. Intracellular Ca2+ Homeostasis and Nuclear Export Mediate Exit from Naive Pluripotency. *Cell Stem Cell* **25,** 210–224.e6 (2019).
102. Morris, J. P. *et al.* α-Ketoglutarate links p53 to cell fate during tumour suppression. **573,** 595–599 (2019).
103. Ran, F. A. *et al.* Genome engineering using the CRISPR-Cas9 system. *Nat Protoc* **8,** 2281–2308 (2013).
104. Fellmann, C. *et al.* An optimized microRNA backbone for effective single-copy RNAi. *Cell Reports* **5,** 1704–1713 (2013).
105. Millard, P. *et al.* IsoCor: isotope correction for high-resolution MS labeling experiments. *Bioinformatics* **35,** 4484–4487 (2019).
106. Chen, S., Zhou, Y., Chen, Y. & Gu, J. fastp: an ultra-fast all-in-one FASTQ preprocessor. *Bioinformatics* **34,** i884–i890 (2018).
107. Dobin, A. *et al.* STAR: ultrafast universal RNA-seq aligner. *Bioinformatics* **29,** 15–21 (2013).
108. Liao, Y., Smyth, G. K. & Shi, W. featureCounts: an efficient general purpose program for assigning sequence reads to genomic features. *Bioinformatics* **30,** 923–930 (2014).
109. Love, M. I., Huber, W. & Anders, S. Moderated estimation of fold change and dispersion for RNA-seq data with DESeq2. *Genome Biol.* **15,** 550–21 (2014).
110. Hosios, A. M. & Vander Heiden, M. G. The redox requirements of proliferating mammalian cells. *J. Biol. Chem.* **293,** 7490–7498 (2018).
111. Arnold, P. K. *et al.* A non-canonical tricarboxylic acid cycle underlies cellular identity. *Nature* **603,** 477–481 (2022).
112. Garcia-Bermudez, J. *et al.* Aspartate is a limiting metabolite for cancer cell proliferation under hypoxia and in tumours. *Nat. Cell Biol.* **20,** 775–781 (2018).
113. Diehl, F. F., Lewis, C. A., Fiske, B. P. & Vander Heiden, M. G. Cellular redox state constrains serine synthesis and nucleotide production to impact cell proliferation. *Nat Metab* **1,** 861–867 (2019).

114. Baksh, S. C. *et al.* Extracellular serine controls epidermal stem cell fate and tumour initiation. *Nat. Cell Biol.* **22,** 779–790 (2020).
115. Li, Z. *et al.* Cancer cells depend on environmental lipids for proliferation when electron acceptors are limited. *Nat Metab* **4,** 711–723 (2022).
116. Luengo, A. *et al.* Increased demand for NAD+ relative to ATP drives aerobic glycolysis. *Mol. Cell* **81,** 691–707.e6 (2021).
117. Ying, Q.-L. *et al.* The ground state of embryonic stem cell self-renewal. **453,** 519–523 (2008).
118. Panopoulos, A. D. *et al.* The metabolome of induced pluripotent stem cells reveals metabolic changes occurring in somatic cell reprogramming. *Cell Res* **22,** 168–177 (2012).
119. King, M. P. & Attardi, G. Human cells lacking mtDNA: repopulation with exogenous mitochondria by complementation. *Science* **246,** 500–503 (1989).
120. Faddah, D. A. *et al.* Single-cell analysis reveals that expression of nanog is biallelic and equally variable as that of other pluripotency factors in mouse ESCs. *Cell Stem Cell* **13,** 23–29 (2013).
121. Halestrap, A. P. The SLC16 gene family - structure, role and regulation in health and disease. *Mol Aspects Med* **34,** 337–349 (2013).
122. Bayraktar, E. C. *et al.* Metabolic coessentiality mapping identifies C12orf49 as a regulator of SREBP processing and cholesterol metabolism. *Nat Metab* **2,** 487–498 (2020).
123. Amici, D. R. *et al.* C16orf72/HAPSTR1 is a molecular rheostat in an integrated network of stress response pathways. *Proc. Natl. Acad. Sci. U.S.A.* **119,** e2111262119 (2022).
124. Kenny, T. C. *et al.* Integrative genetic analysis identifies FLVCR1 as a plasma-membrane choline transporter in mammals. *Cell Metab.* **35,** 1057–1071.e12 (2023).
125. EAGLE, H. & PIEZ, K. The population-dependent requirement by cultured mammalian cells for metabolites which they can synthesize. *Journal of Experimental Medicine* **116,** 29–43 (1962).
126. Merezhinskaya, N. & Fishbein, W. N. Monocarboxylate transporters: past, present, and future. *Histol Histopathol* **24,** 243–264 (2009).
127. Chidley, C. *et al.* A CRISPRi/a screening platform to study cellular nutrient transport in diverse microenvironments. *bioRxiv* 2023.01.26.525375 (2023). doi:10.1101/2023.01.26.525375
128. Datta, R. *et al.* Interactions with stromal cells promote a more oxidized cancer cell redox state in pancreatic tumors. *Sci Adv* **8,** eabg6383 (2022).
129. Atlasi, Y. *et al.* The translational landscape of ground state pluripotency. *Nat Commun* **11,** 1617–13 (2020).
130. Wu, T. *et al.* clusterProfiler 4.0: A universal enrichment tool for interpreting omics data. *Innovation (Camb)* **2,** 100141 (2021).
131. Beigneux, A. P. *et al.* ATP-citrate lyase deficiency in the mouse. *J. Biol. Chem.* **279,** 9557–9564 (2004).
132. Prasun, P. *et al.* Expanding the Clinical Spectrum of Mitochondrial Citrate Carrier (SLC25A1) Deficiency: Facial Dysmorphism in Siblings with Epileptic Encephalopathy and Combined D,L-2-Hydroxyglutaric Aciduria. *JIMD Rep* **19,** 111–115 (2015).
133. Sharpley, M. S., Chi, F. & Banerjee, U. Metabolic Plasticity drives Development during Mammalian Embryogenesis. *bioRxiv* **18,** 2020.10.07.330571 (2020).
134. Leese, H. J. & Barton, A. M. Pyruvate and glucose uptake by mouse ova and preimplantation embryos. *J Reprod Fertil* **72,** 9–13 (1984).
135. Brown, J. J. & Whittingham, D. G. The roles of pyruvate, lactate and glucose during preimplantation development of embryos from F1 hybrid mice in vitro. *Development* **112,** 99–105 (1991).

136. Streffer, C., Elias, S. & van Beuningen, D. Influence of NAD+ on development of mouse blastocysts in vitro. *Nature* **250,** 434–435 (1974).
137. Lane, M. & Gardner, D. K. Mitochondrial malate-aspartate shuttle regulates mouse embryo nutrient consumption. *J. Biol. Chem.* **280,** 18361–18367 (2005).
138. Lane, M. & Gardner, D. K. Lactate regulates pyruvate uptake and metabolism in the preimplantation mouse embryo. *Biol Reprod* **62,** 16–22 (2000).
139. Nagaraj, R. *et al.* Nuclear Localization of Mitochondrial TCA Cycle Enzymes as a Critical Step in Mammalian Zygotic Genome Activation. *Cell* **168,** 210–223.e11 (2017).
140. Choi, E. S., Kawano, K., Hiraya, M., Matsukawa, E. & Yamada, M. Effects of pyruvate and dimethyl-α-ketoglutarate, either alone or in combination, on pre- and post-implantation development of mouse zygotes cultured in vitro. *Reprod Med Biol* **18,** 405–410 (2019).
141. Lee, Y. *et al.* Oligodendroglia metabolically support axons and contribute to neurodegeneration. *Nature* **487,** 443–448 (2012).
142. Lengacher, S. *et al.* Resistance to diet-induced obesity and associated metabolic perturbations in haploinsufficient monocarboxylate transporter 1 mice. *PLoS One* **8,** e82505 (2013).
143. Merezhinskaya, N., Fishbein, W. N., Davis, J. I. & Foellmer, J. W. Mutations in MCT1 cDNA in patients with symptomatic deficiency in lactate transport. *Muscle Nerve* **23,** 90–97 (2000).
144. van Hasselt, P. M. *et al.* Monocarboxylate transporter 1 deficiency and ketone utilization. *N Engl J Med* **371,** 1900–1907 (2014).
145. Murray, C. M. *et al.* Monocarboxylate transporter MCT1 is a target for immunosuppression. *Nat Chem Biol* **1,** 371–376 (2005).
146. Silva, A. *et al.* In Vivo Anticancer Activity of AZD3965: A Systematic Review. *Molecules* **27,** 181 (2021).
147. Gray, L. R., Tompkins, S. C. & Taylor, E. B. Regulation of pyruvate metabolism and human disease. *Cell. Mol. Life Sci.* **71,** 2577–2604 (2014).
148. Erez, A. & DeBerardinis, R. J. Metabolic dysregulation in monogenic disorders and cancer - finding method in madness. *Nat Rev Cancer* **15,** 440–448 (2015).
149. Finsterer, J. Leigh and Leigh-like syndrome in children and adults. *Pediatr Neurol* **39,** 223–235 (2008).
150. DeBerardinis, R. J. & Thompson, C. B. Cellular metabolism and disease: what do metabolic outliers teach us? *Cell* **148,** 1132–1144 (2012).